THE PENNSYLVANIA STATE UNIVERSITY
SCHREYER HONORS COLLEGE

DEPARTMENT OF METEOROLOGY & ATMOSPHERIC SCIENCE

An Analysis of Environmental Factors and Radar Features Present Prior to Tornadogenesis in Quasi-Linear Convective Systems

SEAN D. MELANSON
SPRING 2022

A thesis
submitted in partial fulfillment
of the requirements
for a baccalaureate degree
in Meteorology & Atmospheric Science
with honors in Meteorology & Atmospheric Science

Reviewed and approved* by the following:

Yvette Richardson
Associate Dean for Undergraduate Education in the College of Earth and Mineral Sciences &
Professor of Meteorology

Paul Markowski
Distinguished Professor of Meteorology

* Electronic approvals are on file.

ABSTRACT

Quasi-Linear Convective Systems (QLCSs) often produce weak, short-lived tornadoes compared to supercells, but can still produce devastating impacts to the most vulnerable communities, living in poorly constructed houses and mobile homes. QLCS tornadoes are also more challenging to forecast than supercell tornadoes, partly as a result of the lack of radar precursors, resulting in many missed events and false alarms. QLCSs have not garnered as much focus in recent literature as supercells, and as such, progress in QLCS tornado forecasting has been slow. In chapter one of this three-part study, we focus on understanding the challenges associated with predicting QLCS tornadoes by evaluating the effectiveness of existing forecasting tools such as the “Three Ingredients Method" (3IM) and radar features referred to as “Confidence Builders and Nudgers” (CB/N). We found 3IM to be an effective distinguisher between QLCSs that are likely and unlikely to produce tornadoes but did not find CB/N to add value in determining when and where a forecaster should issue a tornado warning. In chapter two, we apply the K_{DP}/Z_{DR} separation method, known as a precursor to tornadogenesis in supercells, to a dataset of tornadic QLCSs using a Python algorithm to determine if it also has merit as a precursor to QLCS tornadogenesis. We found the mean K_{DP}/Z_{DR} separation distance to be 20.8 km with a standard deviation of 16.0 km. While a focus on null cases is required in future work to add validity to our findings, our results indicate it may have some value as a forecasting tool. In chapter three, we examined the sensitivity of vertical vorticity and velocity patterns at the leading edge of a QLCS to a heterogeneous shear environment. We performed 4 QLCS simulations, one of which was performed in shear varying sinusoidally in the meridional direction, while the other 3 were run in homogeneous shear of 10, 15, and 20 m/s. We found the QLCS simulated in the homogenous, high-shear domain produced the weakest updrafts and vertical vorticity. In the heterogeneous shear case, our strongest cyclonic vortices were located in weak to moderate shear while the strongest updrafts were located in moderate shear. We hope the results presented in this paper not only provide value to forecasters but stimulate further research on developing new QLCS forecasting tools.

TABLE OF CONTENTS

LIST OF FIGURES

LIST OF TABLES

ACKNOWLEDGEMENTS

I would like to thank Dr. Yvette Richardson for her mentorship not only during this research project but throughout my undergraduate career, Dr. Paul Markowski for his suggestions during the review of this manuscript, Dr. Matt Kumjian for his assistance in the research described in chapter two, and Shawn Murdzek for his help in formulating the Python script used in chapter two. I would also like to thank Mark Fox of NWS Norman, OK, Aaron Ward of NWS Amarillo, TX, the team at NWS Amarillo, and the Pathways Program for their support and guidance in chapter one of this paper. We are grateful for the accessibility of CM1, developed and supported by George Bryan of NCAR and for the availability of the Grid Analysis and Display System (GrADS) developed by the Center for Ocean-Land-Atmospheric Studies at George Mason University which made this research possible.

Chapter 1 Introduction

Section 1: The QLCS Problem

QLCSs (Quasi-Linear Convective Systems), commonly known as squall lines, are nearly continuous lines of thunderstorms. They typically form in environments favorable for thunderstorm development with strong deep layer shear (>40 kts 0-6 km bulk wind difference; Thompson et al. 2012) and are sustained by continual dynamic uplift along the gust front ahead of the line.

QLCSs possess the ability to create mesovortices, or areas of rotation within the line, which can be associated with tornadoes and damaging straight line winds. Despite the fact that QLCS tornadoes are usually weak (EF 0-1), they are of interest because they often produce tornadoes outside of the Great Plains (a traditional tornado hotspot) in areas less frequented and less prepared for severe weather (Trapp et al. 2005). They also are more likely to produce tornadoes during the overnight hours compared to supercells (Trapp et al. 2005).

QLCS tornadoes are notoriously difficult to both accurately nowcast and warn. This is primarily a result of the lack of radar indicated rotation prior to tornadogenesis compared to supercells (Trapp et al. 1999). As a result, one of the greatest threats posed by QLCS tornadoes is the element of surprise imposed by the lack of adequate lead time.

Part of the reason for the lack of accurate warnings is because the method by which QLCS tornadoes form is not well understood. Several hypotheses have been presented to explain mesovortex and subsequent tornado development. Horizontal shearing instability has been thought to play a role in QLCS tornadogenesis (Carbone 1982, 1983; Lee and Wilhelmson

1997a,b). Another theory proposes that mesovortex development is closely related to downward tilting of vortex lines by the downdraft (Weisman and Trapp 2003). Once vorticity is oriented in the vertical, strong updrafts, modulated by the strength of the low-level shear, stretch the vorticity into a strong mesovortex capable of producing a tornado (Schaumann and Przybylinski 2012).

Section 2: The "Three Ingredients Method" and Confidence Builders/Nudgers

Several techniques have been developed to aid forecasters in predicting and issuing warnings for QLCS tornadoes. The most notable of these includes "The Three Ingredients Method" (3IM) set forth by Schaumann and Przybylinski (2012). An analysis of a dataset of QLCSs revealed three criteria which, when all were satisfied, were intended to distinguish between QLCSs that were and were not likely to produce tornadoes as well as identify broad areas within the line that would be most favorable for tornadogenesis. These 3 criteria are presented in Figures 1 and 2 and include:

1. A segment of the QLCS where the system's cold pool and ambient low-level shear are balanced
2. Environmental 0-3 km line-normal bulk shear greater than or equal to 30 kts
3. A rear inflow jet (RIJ) or area of enhanced outflow that creates a bow or surge in the line.

When the ambient shear and system cold pool are balanced, lifting is enhanced, resulting in strong updrafts that maximize vortex stretching (Rotunno et al. 1988; Schaumann and Przybylinski 2012; Figure 3). The threshold for creating this balance is hypothesized to be 0-3 km shear of at least 15 m/s or 30 kts (Schaumann and Przybylinski 2012). The reason bows and surges in the line can be indicators of vortexgenesis is a result of a strong downdraft which leads to an enhancement of the updraft on the leading edge of the surge. This strong updraft then tilts vortex lines previously produced baroclinically in the cold pool, leading to a cyclonic-anticyclonic pair of vortices (Atkins and St. Laurent 2009b).

The criteria set forth by Schaumann and Przybylinski (2012) serves as a starting point for forecasters, but the issue frequently arises that the area where all 3 ingredients are satisfied is on a spatial and temporal scale exceeding that of a tornado warning. Additional tools have been developed through the National Weather Service (NWS) Central Region Tornado Warning Improvement Project to help forecasters decide when and where to issue warnings. A “QLCS Mesovortex Warning System Reference Sheet” was created which includes details of 3IM as well as a list of radar features that are supposed to be indicative of QLCS tornadogenesis referred to as “Confidence Builders” and “Nudgers” (CB/N). This collection of radar features, including the updraft downdraft convergence zone (UDCZ) entry point, paired front/rear inflow notches, and cell mergers, can be seen in Figure 4. Williamson et al. (2021) found 3IM to have merit as a forecasting tool and Gibbs (2021) found that CB/N had some forecasting skill when combined with 3IM. However, the study did not examine trends in CB/N before unwarned vs warned tornadoes or before unverified warnings.

Section 3: K_{DP}/Z_{DR} Separation in QLCS Radar Fields

Another technique proposed to aid forecasters in deciding when and where to warn involves the use of Dual-Polarization (Dual-Pol) radar products, which allow operational meteorologists to identify distinct sub-storm scale features, including tornadic debris signatures, hail, and turbulence, and use them to more accurately forecast storm evolution. Two of these products include differential reflectivity (Z_{DR}) and specific differential phase (K_{DP}). Z_{DR} is the difference between the power scattered back to the radar in the horizontal and vertical polarizations. Positive Z_{DR} indicates the radar detects objects that possess a major axis in the horizontal, while negative Z_{DR} indicates objects have a major axis in the vertical, and a Z_{DR} near zero is indicative of spherical hydrometeors. K_{DP} measures the difference between the phase shifts of horizontally and vertically polarized energy after passing through a medium per unit distance along the direction of propagation. K_{DP} is dependent on particle concentration and is thus proportional to the mass of nonspherical hydrometeors along the polarization direction.

In supercells, recent work has shown that prior to tornadogenesis, enhanced regions of Z_{DR} and K_{DP} that are initially collocated along the inflow side of the storm can become separated, with the K_{DP} enhancement region moving farther into the forward-flank downdraft as a result of size-sorting of hydrometeors. An example can be seen in Figure 5, adapted from Romine et al. (2008). The process of K_{DP} and Z_{DR} enhancement regions becoming separated can be explained by drop residence time in sheared flow (Figure 6). Smaller drops fall slower than larger drops, which allows the flow to advect them farther downstream, while larger drops are not advected as far (Crowe et al. 2012). During the fall of a raindrop, air resistance causes the bottom to take on a flat appearance. As a result, the major axis is in the horizontal, resulting in the observed enhanced Z_{DR} values where mainly large drops are present. K_{DP} is enhanced in the region of smaller drops as a result of the increased number concentration on which K_{DP} is dependent. The primary reason separation between high values of K_{DP} and Z_{DR} is hypothesized to be indicative of tornadic development is due to the storm ingesting locally enhanced regions of storm-relative helicity (SRH) which in turn increases size-sorting (Kumjian and Ryzhkov 2008a, 2009).

A similar theory involving K_{DP}/Z_{DR} separation has been proposed for QLCS tornadoes. Anderson-Frey et al. (2016) found links between QLCS tornado occurrence and large 0-1 km SRH. Given the relationship between SRH and storm-relative winds, this suggests size-sorting may be present prior to QLCS tornadogenesis (Loeffler and Kumjian 2018). Previous studies have explored relationships between K_{DP}/Z_{DR} separation and QLCS tornadoes. Crowe et al. (2012) provided an example of this process using a case from 27 April 2011. Loeffler and Kumjian (2018) explored the topic further by developing an algorithm that identified regions of max K_{DP} and Z_{DR} for which there were 10 radar gates within a subjectively drawn "analysis box" around a region of interest. The separation distance was found as well as the angle between the storm motion vector and separation vector. The study done by Loeffler and Kumjian (2018) was developed based on tornadoes occurring east of the 88° W line of longitude while our study focuses on QLCS tornadoes that occurred west of 88° W.

Section 4: Heterogeneities in QLCS Environments

A QLCS can span for 100s of km along a north-south oriented line, so it should come as no surprise that such storms frequently encounter environments containing varying quantities of moisture, shear, instability, etc. Such a situation is often present in the southeast United States where the presence of the Gulf of Mexico allows a strong low-level jet to transport large quantities of moisture into the southernmost regions while areas farther north remain drier. An example of this can be seen in Figure 7. In other situations, mesoscale features such as differential heating zones or boundary layer mixing can alter shear profiles. Such processes may influence the internal mechanisms responsible for tornadogenesis in QLCSs.

Previous work has shown how convective storms behave in environments with heterogeneous wind shear. Richardson et al. (2007) performed simulations using the Advanced Regional Prediction System (ARPS) to compare the evolution of storms in heterogeneous and homogeneous shear environments. They found that when convection is initiated in a heterogeneous strongly sheared environment, typical of that found in between multicell and supercell modes, the lower shear flank favored increased cell development while the higher sheared flank favored increased cell organization. While this particular study focuses on severe convection as a whole rather than explicitly on QLCSs and the influence of heterogeneous shear on tornadogenesis, it demonstrates the importance of differential shear in a storm's environment.

Limited research has been done to study how heterogeneous environments affect the ability of a QLCS to produce mesovortices capable of tornadogenesis. Wheatley and Trapp (2008) investigated the structure and evolution of two observed QLCSs using the Advanced Research Weather and Forecasting (WRF-ARW) model to perform real-data numerical simulations. One QLCS, which occurred on 24 October 2001, evolved in a homogenous environment while the other, which occurred on 6 July 2003, evolved in a heterogeneous environment of equivalent potential temperature and low-to-mid level, including 0-3 km, shear. The most notable result from their study was that variations in low-to-mid level shear along the line contributed to deeper lifting and stronger mesovortices where shear was stronger and weaker lifting and mesovortices where shear was weaker. However, they also noted the increase in wind shear was accompanied by larger amounts of CAPE. This result agrees with Schaumann and Przybylinski (2012) in their discussion of the importance of strong 0-3 km shear for developing sufficiently strong updrafts that can tilt and stretch vorticity but does not consider how the environmental heterogeneity of shear itself may change the structure of the QLCS and the dynamics at play.

Section 5: Objectives of this Study

The goal of this study is twofold. In chapter one, we conduct an analysis of the effectiveness of existing forecasting tools, including the "Three Ingredients Method" proposed by Schaumann and Przybylinski (2012) and confidence builder/nudger radar features developed through the NWS Central Region Tornado Warning Improvement Project. Our study serves as a confirmation analysis of the results found in Gibbs (2021) but also takes a unique perspective by examining trends in the number of CB/N present prior to unverified and verified tornado warnings as well as unwarned tornadoes. In chapters two and three, we explore two new topics to the QLCS tornado space and investigate the implications for operational meteorologists. Chapter two investigates the applicability of K_{DP}/Z_{DR} separation, a known precursor to tornado formation in supercells, to QLCS tornadogenesis. Our study takes a different approach than Loeffler and Kumjian (2018) on how regions of enhanced K_{DP} and Z_{DR} are identified, using percentiles as opposed to fixed radar gates. We also include detailed computer-generated graphics demonstrating the structure of K_{DP} and Z_{DR} maxima within each QLCS examined. In chapter three, we perform a numerical simulation to compare QLCS evolution in 3 simulations with 10, 15, and 20 m/s homogeneous 0-3 km shear with a heterogeneous run containing shear varying from 10 to 20 m/s. Our approach expands on the study done by Wheatley and Trapp (2008) as we investigate mesovortex development purely as a result of an inhomogeneous environment of low-level shear.

Chapter 2

An Analysis of the Effectiveness of Forecaster Tools Developed through the NWS Central Region Tornado Warning Improvement Project

Section 1: Methods

A total of 20 QLCS cases were selected for this study from 1996 to 2021. The westernmost storm was located near Las Animas, CO and the easternmost storm was located near Portage, WI. They were divided into 10 tornadic (at least one tornado reported) and 10 nontornadic cases. Nontornadic QLCSs were selected if the center of the leading edge of the convection was within 100 km of a radar. Tornadic QLCSs were selected only if their associated tornadoes were not embedded within convection or farther than 100 km from the radar. It should be noted that all tornadic cases took place during the time when Dual-Polarization products were available.

For each of the 20 cases, we examined the QLCS to determine which, if any, of the criteria in 3IM were satisfied. We assessed whether a surge or bow was present in the line as well as the balance between the cold pool and environmental shear using the method outlined in Figures 1 and 2. These criteria were assessed either at the time step prior to a tornado developing (if one was present) or throughout the lifespan of the QLCS to determine if both criteria were satisfied at any one time. 0-3 km shear was calculated using the North American Regional Reanalysis (NARR) sounding archives from Northern Illinois University. We would have preferred to use the Storm Prediction Center's mesoanalysis archive, but unfortunately 0-3 km shear was unavailable in the archive. For tornadic QLCSs, soundings were taken at the closest time prior to and at the location of each reported tornado. For nontornadic cases, soundings were taken at the closest time prior to and at the location where the other two criteria were met and the QLCS appeared to be strongest as evidenced by severe reports and structure, such as size, continuity of strong updrafts along the leading edge, or a rear inflow jet. We calculated the 0-3 km shear magnitude and direction from the hodograph on the sounding and overlaid it with the QLCS's UDCZ on radar to determine whether the line-normal component was greater than 30 kts at any point along the UDCZ where the other two criteria were satisfied (for nontornadic cases) or at the location of the tornado report (for tornadic cases). While our method is subjective to some biases related to timing and errors associated with the calculation process, it should be noted that in most cases, it was abundantly clear that the 0-3 km shear requirement was or was not satisfied.

For each of the 10 tornadic cases, a radar analysis using the Gibson Ridge radar software (GR2Analyst), was performed subjectively one radar time step prior to tornadogenesis to identify the number of CB/N present prior to:

1. Warnings verified with Local Storm Reports (LSRs)
2. Unverified Warnings
3. Unwarned LSRs

In GR2Analyst we were able to overlay tornado warnings and reports with NEXRAD Level II WSR-88D radar data from Amazon Web Services, an example of which can be seen in Figure 8. We only included CB/N present one radar timestep prior to the tornado (unwarned LSRs) or tornado warning (verified or unverified) in order to evaluate the predictive power of these features. Consistent with Gibbs (2021) we did not include a tornadic debris signature as a feature because this would indicate a tornado was already on the ground and has no value as an actual predictor of tornadogenesis. It should also be noted that the 0-3 km CAPE value we used was a computed parameter on the same sounding as was used to find the 0-3 km shear. In the event multiple tornadoes were present within 10 km, only the one closest to the radar was selected in order to avoid multiple reports of the same tornado.

We also looked for trends in tornado warning lead time and computed several verification statistics for each tornadic QLCS including the probability of detection (POD) and False Alarm Ratio (FAR).

Section 2: Results and Discussion

An analysis of the effectiveness of 3IM as a distinguisher between tornadic and nontornadic QLCSs revealed its ability to serve as a starting point for forecasters when looking at QLCS environments. No nontornadic cases with all 3 criteria satisfied were found in our dataset. Only one tornadic case did not have all 3 ingredients satisfied. It is possible in this one case that the 0-6 km shear may have played a role in mesovortex development as a result of enhanced lifting via the updraft in shear effect as proposed in a recent research presentation by Dr. Ariel Cohen and Jason Schaumann as part of the NWS Central Region Tornado Warning Improvement Project (Cohen and Schaumann). The study indicates that this process may be more likely to occur when the 0-6 km bulk shear has a larger line-normal component than the 0-3 km shear. This is consistent with the results found in Williamson et al. (2021). Another possible explanation is that because cold pool strength varies between QLCSs, the 0-3 km shear requirement to balance the cold pool may not be rigid and instead depend on cold pool strength.

In Figure 9, we present the results of our analysis of CB/N radar features present prior to warnings verified with LSRs, unverified warnings, and unwarned LSRs. The scatter plot shows the number of CB/N present in each situation for every tornadic QLCS case. The tornado threshold of 3 was added based on the scale in Figure 10 which shows the number of CB/N that are supposed to be strongly indicative of a tornado forming. Our results show that there is little correlation between the number of CB/N radar features present prior to QLCS tornadogenesis and a tornado actually being reported. Some tornadoes (warned or unwarned) occurred with 1 feature and others with 4 or 5. These results are not consistent with those found in Gibbs (2021). This may be due, in part, to the fact that some of these features are inherently difficult to identify. The highly subjective nature of CB/N identification serves as a limitation of our results. Additionally, forecasters may disagree on what constitutes a particular CB/N.

The lead times for all warned QLCS tornadoes were also found and are presented in Figure 11. We found that lead times varied greatly across all events with 25% having a minute or less, which would provide little to no time for the average person to react, highlighting the challenge associated with issuing warnings in these situations.

We also computed POD and FAR verification statistics for each tornadic QLCS event (Table 1). It should be noted, however, that the 7 March 2016 case was omitted because the warning was issued after the one tornado touched down and before it lifted. We found a trend of high FAR and low POD, but these statistics varied for each event. In several events, there were many more unverified than verified warnings. An example of this is the 9 September 2019 QLCS in which one warning was verified with a tornado but 4 others went unverified, highlighting an over cautious bias. As seen in Table 1, these situations would produce perfect PODs but FARs near 1. However, it should be noted that a limitation to the results of these verification statistics lies in the small sample size of nine. Despite this, these results further serve to highlight the challenges associated with warning QLCS tornadoes and our need for research into more effective forecasting tools.

Chapter 3

An Analysis of K_{DP}/Z_{DR} Separation in QLCS Tornado Events Using a Python Algorithm

Section 1: Methods

10 unique QLCS events as far west as Pueblo, CO and as far east as Portage, WI were selected for the analysis of K_{DP}/Z_{DR} separation (Table 2). These were the same cases as were used for the study in chapter one. Not all QLCS cases satisfied the criteria of a contiguous 100 km line with reflectivity of at least 35 dBZ, but the aspect ratio criterion of 3 to 1 outlined in Smith et al. (2012) was satisfied. However, all QLCS cases had a contiguous area of reflectivity greater than or equal to 35 dBZ that was larger than 2800 km^2.

Several QLCSs produced multiple tornadoes that were analyzed individually for a total of 18 QLCS tornado events. Tornado reports were selected from the Storm Prediction Center's filtered storm reports, each occurring on the leading edge of the most intense convection. Reports embedded within convection or farther than 100 km from the radar were discarded. However, some tornadoes may appear to be slightly embedded in the QLCS (Figures 12-47). This is due to differences in the tornado report time and the nearest available radar scan. The fast storm motions also contribute to this effect especially in storms with a well-developed rear inflow jet. Although the largest time difference was only 3 minutes, this still serves as a limitation to our results.

The most challenging aspect of analyzing K_{DP}/Z_{DR} separation is the subjectivity introduced by attempting to isolate enhanced regions of K_{DP} and Z_{DR}. In order to remove this subjectivity, an algorithm was developed in Python using the Python ARM Radar Toolkit (Py-ART). Py-ART is a library of functions and utilities designed specifically for analyzing radar data in Python (Helmus and Collis 2016). NEXRAD Level II WSR-88D radar data was used for this analysis from Amazon Web Services. It should be noted that only radar images at the volume scan time (VST) were able to be analyzed using Py-ART. Reflectivity, Velocity, K_{DP}, and Z_{DR} fields were extracted from each radar data file and plotted along with the tornado report. K_{DP} was not an included field and instead required computation based on the differential phase field. This was done through the built-in function provided by Maesaka et al. (2012).

Contours of Z_H, K_{DP}, and Z_{DR} were created based on smoothed fields using a gaussian filter with a standard deviation of three. A 90th percentile calculation was performed to create an adaptive threshold for K_{DP} and Z_{DR} rounded to the nearest 0.5 that would identify localized maxima based on each storm's unique structure. This is a different approach than the fixed 10-gate threshold used by Loeffler and Kumjian (2018) but may be more effective along a QLCS where there are multiple pockets of enhanced K_{DP} and Z_{DR}. In order to avoid creating thresholds based on erroneous data outside the storm, the algorithm only considered values of K_{DP} and Z_{DR} collocated with reflectivity of at least 35 dBZ. The program also only plots contours within 35 dBZ reflectivity contours and only if they have an area of at least 30 km^2 . This is similar to the 20 km^2 threshold used for an analysis of supercellular K_{DP}/Z_{DR} separation in Wilson and Van Den Broeke (2021) but is slightly stricter to reduce the increased noise in QLCSs compared to supercells. A centroid was plotted in the center of each of the K_{DP} and Z_{DR} contoured polygons using the Shapely Python package which calculates the center of an object based on the mean of all points along the outline. The K_{DP} and Z_{DR} centroids closest to the tornado report were identified in order to compute the separation distance and plot the vector. Each distance value was stored for further analysis, although if one of the centroids was more than 30 km from the tornado report it was set to 0. This is similar to the approach taken in Van Den Broeke (2021) which matched the K_{DP} and Z_{DR} centroids to the nearest storm object, or centroid of the 45 dBZ polygon associated with the supercell, as long as the distance was smaller than 30 km. However, due to structural differences between supercells and QLCSs, it was more appropriate to match the centroids to a tornado report in our study.

Finally, a statistical analysis was performed on the results. A box plot of the separation distance was created along with a 95% confidence interval and estimate of the variability in the sample mean using a bootstrapping technique.

Section 2: Results and Discussion

For each tornado event, a 4 panel plot was produced showing reflectivity, velocity, K_{DP}, and Z_{DR} (Figures 12-46 even). Contours of 35 dBZ were plotted over reflectivity and 90th percentile values were contoured on top of the K_{DP} and Z_{DR} plots. Additionally, a separate plot of just the contours, centroids, and the K_{DP}/Z_{DR} vector were plotted for analysis of the separation (Figures 13-47 odd). A subjective analysis of the K_{DP} and Z_{DR} fields show that enhanced regions are often clustered near the tornado report relative to other regions of the QLCS. This could be related to the size-sorting as a result of ingestion of localized SRH maximums that play a role in tornado development. As a result of the close proximity of centroids to each tornado report, a K_{DP}/Z_{DR} separation distance was able to be found for all but one tornado event. The mean separation distance was found to be 20.8 km with a standard deviation of 16.0 km. While the standard deviation is indicative of large variation in the orientation of K_{DP} and Z_{DR} polygons relative to the tornado report, it is possible this may be due to the variability between the structure of different tornadic regions of QLCSs and not random patterns of K_{DP} and Z_{DR} maximums in QLCSs as a whole.

A box plot of the separation distance (Figure 48) demonstrates the distribution of values that range from 0 to 54.2 km. The first quartile is located at 6.0 km and the third quartile is at 29.2 km with a median of 20.3 km. It should be noted that the box plot is left-skewed as the median is shifted closer to the third quartile. This indicates that the data is not a normal distribution, and that most K_{DP}/Z_{DR} separation distances are on the higher end. In order to quantify the uncertainty surrounding the mean of the sample, specifically the range in which we could expect the population mean to fall, a 95% confidence interval was constructed which ranged from a separation distance of 12.6 km to 29.0 km (Figure 49). We also plotted a bootstrap sample on top of the confidence interval. This calculation was performed by taking 50 random samples of 4 data points each with replacement, finding the mean, and plotting it on a number line that spanned the values of the 95% confidence interval (Figure 49). We found that all of the averages of the random samples were within 10% of the true mean of the entire sample indicating this mean well represents the sample data.

The results of our statistical analysis also provide some important implications for operational forecasters, specifically that K_{DP} and Z_{DR} separation is large enough to be identified visually most of the time, a crucial aspect during fast-paced warning operations. Some of the smaller K_{DP} and Z_{DR} separations, such as in Figure 43 with a value of 7.2 km, are still relatively distinct.

There are several limitations to our results. Without a complementing analysis of K_{DP}/Z_{DR} separation in non-tornadic QLCS events, any conclusions in tornadic cases may be solely attributable to the normal structure of K_{DP} and Z_{DR} fields in these storms and not to the presence of a tornado. This study also does not factor in the angle between the K_{DP}/Z_{DR} separation vector and the storm motion vector. Thus, some cases show K_{DP} closer to the leading edge of convection rather than Z_{DR}, which contradicts the example of QLCS K_{DP}/Z_{DR} separation provided in Crowe et al. (2012). Additionally, in many of the observed cases, there were multiple K_{DP} and Z_{DR} polygons present and although the separation vector was only drawn between the closest K_{DP} and Z_{DR} centroids to the tornado report, the distance between two centroids of K_{DP}

or Z_{DR} and the tornado report may have been close such as in Figure 25. Thus, deciding which polygon to use in drawing the separation vector during a real event could produce ambiguity in where a forecaster should issue a tornado warning. Finally, the sample size of 18 is small and more cases would have helped provide additional confidence in our results.

Chapter 4

Numerical Simulations of Heterogeneous Environmental Low-Level Shear in QLCSs

Section 1: Methods

Our simulations were performed using version 20.3 of the Bryan Cloud Model 1 [CM1; Bryan and Fritsch (2002)]. The model domain was 150 x 150 x 20 km^3, with a horizontal grid spacing of 250 m and a vertical grid spacing of 100 m. The E-W lateral boundary conditions were open wave radiative, and the N-S lateral boundary conditions (BCs) were periodic. The N-S lateral BCs were periodic to create a continuous QLCS with no defined tails on the northern or southern ends. As a result, we minimized the influence of these features on the development of tornado-like vortices in the line. A complete set of CM1 settings used to run the simulations can be found in Table 3.

The QLCS was initiated using a N-S oriented line of 10 warm bubbles with a 2.0 K maximum potential temperature perturbation spaced 15 km apart, just enough to ensure that they were not intersecting each other at initialization given the radius of each bubble was 7.5 km (Figure 50). All bubbles also had a vertical radius of 1.4 km and were centered above the ground at 1.4 km. The intention of this method of storm initiation is to represent a QLCS that forms from upscale growth of originally discrete cells. We ran the simulation for a total of 7200 seconds or 2 hours.

We used the Weisman-Klemp analytic base-state sounding (Weisman and Klemp 1982) with a mixing ratio of 14 g/kg and a surface potential temperature of 300 K. An RKW-type wind profile was used in each simulation, based on the theory presented in Rotunno et al. (1988). According to RKW theory, the strength and maintenance of squall line updrafts are driven by the interaction of the system's cold pool and ambient low-level shear. To align our study with this fundamental concept, we created a linearly increasing westerly wind from the surface to 3 km. Above 3 km, the wind speed was set to a constant 15 m/s. 0-3 km shear was specifically chosen because climatologically, the strength of this shear layer is related to the ability of a QLCS to produce tornadoes (Schaumann and Przybylinski 2012). We performed 3 QLCS simulations with homogenous 0-3 km shear of 20, 15, and 10 m/s (Figure 51). In our final, heterogeneous simulation, we allowed the shear to vary sinusoidally along the N-S axis of the domain. The 0-3 km wind shear reached a maximum in the center of the southern half of the domain and a minimum in the center of the northern half of the domain (Figure 52).

We examined 5-minute output of the 4 simulations for areas along the gust front where vertical vorticity was enhanced. This is where QLCS tornado formation would be favored because there is a pool of circulation that could be further contracted. Tornadoes cannot be resolved using 250 m resolution, but we are simply looking for areas most favorable for tornadogenesis based on patterns of vertical vorticity.

Section 2: Results and Discussion

In each of our simulations, we compared simulated reflectivity, vertical velocity, potential temperature perturbation, and vertical vorticity fields over the evolution of the QLCS using the Grid Analysis and Display System (GrADS).

We begin with a discussion of our 3 homogeneous shear simulations. Storms initialized with the warm bubbles quickly grew upscale, forming a QLCS after 1 hour as evidenced by the merging of the cold pools from the 10 cells (Figure 53). All 3 QLCSs remained symmetrical and linear, without any surges or bows in the line throughout the simulation.

We found the cold pool was the strongest in the moderate shear case and weakest in the strong shear case, as evidenced by the potential temperature perturbation at the lowest level and final model time of 2 hours (Figure 54b, 55b). The moderate shear case had a slightly stronger cold pool than the weak shear case (Figure 55b, 56b). Substantial differences in the vertical velocity fields were observed at 1 km above the surface between the 3 homogenous simulations. The strongest updrafts were present in the moderate shear case where vertical velocities reached 10 m/s by 2 hours (Figure 55c). The uplift was also continuous and sustained along the gust front. Updrafts in the low shear case were not as strong, only reaching 8 m/s (Figure 56c). Lifting was also not as continuous as in the moderate shear case, with several breaks along the gust front where rising motions were substantially weaker than in the rest of the line. Updrafts in the high shear case were not organized in any way along a gust front and remained the weakest of the 3 cases (Figure 54c).

These results align well with our expectations that balance between the ambient shear and the system's cold pool, expected to occur in 15 m/s of line-normal shear, will promote strong lifting. We also expected the cold pool to be strongest in the moderate shear case as strong vertical updrafts will promote intense precipitation which will substantially cool the surrounding air as it falls. However, we were expecting the high shear simulation to result in at least some weak, continuous lifting along the gust front. Considering the cold pool was the weakest in this simulation, it is possible it was not strong enough to promote deep and strong lifting (Figure 54b, c). Also, while the cold pools did merge, the imprints of the original cells could still be seen in Figure 54b.

A close examination of the near surface (50m) vertical vorticity fields of the 3 homogenous simulations revealed that vertical vorticity values at the final model time of 2 hours reached $0.05\ \mathrm{s}^{-1}$ in the low and moderate shear cases but were weaker in the high shear case, with vortices only reaching $0.04\ \mathrm{s}^{-1}$ (Figure 54d, 55d, 56d). The reason for the weaker vortices in the high shear case can likely be linked to the failure of strong, continuous lifting along the gust front. We did not expect vortices in the moderate and low shear cases to reach similar strengths considering that uplift along the gust front in the low shear simulation was considerably weaker than in the moderate shear simulation. We also found that there were more vortices along the leading edge of the low shear case than in the other two. It is possible that this is a result of enhanced baroclinicity in the cold pool of the low shear simulation, which would enhance vorticity generation in the cold pool that could subsequently be tilted and stretched by the updraft.

In our simulation initialized with heterogeneous 0-3 km wind shear varying from 10-20 m/s, the cells were initiated from the warm bubbles and quickly grew upscale. By 80 minutes, the cold pools of the original cells had completely merged indicating a QLCS had developed. The system had also taken on a slight “S” shape with the northern segment bowing out towards the east and the southern segment bowing out towards the west (Figure 57a). This is a consequence of the shear profile. In creating the weak shear portion of the environment, while still retaining a constant 15 m/s wind above 3 km, we increased the westerly component of the wind in the lowest levels. In our strong-shear environment, the system-relative winds in the lowest levels are more easterly (Figure 52). Indeed, the system motion in different portions of the domain is similar to that in the corresponding homogeneous simulations, and the resulting pattern of convection changes the amount of line-normal shear experienced by different locations.

The vertical velocity field at 1 km indicates updrafts were the weakest along the leading edge of the QLCS in the low, 10 m/s shear (Figure 57c). This is consistent with the weak updrafts observed in the 10 m/s homogenous simulation. The strongest updrafts were located between the regions of maximum and minimum shear, in values closer to 15 m/s (Figure 57c). This is contrary to what we would expect because the line-normal component is actually less than the optimal 15 m/s described in Schaumann and Przybylinski (2012). If we assume the cold pool of the QLCS in the 15 km south to 15 km north region is oriented 45 degrees to the shear vector (directed due east), the system is only experiencing

$$(15 \text{ m/s})\cos(45°)=10.6 \text{ m/s} \qquad (1)$$

of shear. It should be noted that some outflow surges were observed and thus it is possible for the cold pool to be locally balanced with the ambient shear. However, strong updrafts were observed where the cold pool was clearly not oriented normal to the shear vector. It is possible the reason for this result is because the 0-3 km shear threshold needed to balance the cold pool is not actually a fixed value but instead changes based on cold pool strength as measured by the potential temperature perturbation and depth.

Vertical vorticity at 50 m above the surface was examined for the heterogeneous case, revealing some differences compared to the homogenous simulations. Vortices were stronger, reaching 0.07 s^{-1}, than any vortex in the 3 homogenous runs. Several strong cyclonic vortices were observed just north of the apex of the northern bowing segment with several weaker vortices along the leading edge of the northern bowing segment and south of the southern bowing segment. This fits our conceptual model of how mesovortices form along a bowing segment, as cyclonic vortices are more likely to form north of a surge (Atkins and St. Laurent 2009b). Several strong, negative vortices were observed at the midpoint between the two bowing segments but most of the vertical vorticity along the leading edge of the QLCS was positive. We also found that not only did stronger vortices form along the northern bowing segment in weak shear, but more were present along the leading edge when compared to the southern bow. This is contrary to our expectations as we would expect stronger lifting to enhance vertical vorticity and because some of the strongest vortices formed in the weakest updrafts. One possible explanation for this result is the generation of baroclinic vorticity. A close examination of the cold pool behind the gust front prior to the development of the strongest vortices as seen in the plot of potential temperature perturbation in Figure 58a,b, reveals streaks of cold air. This would indicate locally strong baroclinic generation of vorticity within a weaker overall cold pool when compared to the southern bowing segment, potentially giving rise to ample zonally oriented horizontal vorticity that can be tilted into the vertical and stretched. Indeed, we observed more horizontal vorticity in the cold pool of the northern bowing segment than the southern bowing segment in the 13 and 26 minutes prior to the strongest vortices forming (Figure 58c,d). We also found the meridional component of vorticity to be stronger along the gust front of the northern bowing segment than along the gust front of the southern bowing segment (Figure not shown). This is contrary to our expectations as the baroclinic zone across the gust front is weaker along the northern bowing segment.

There exist several limitations to the results presented here. In the creation of our varying shear profile, we ultimately introduced a background vorticity into the simulation. In the central half of the domain, between the two bowing segments, our zonal wind increases towards the north, indicating a region of negative environmental vertical vorticity. Equivalent positive vorticity is found in the region north of the shear max and south of the shear minimum. This environmental vertical vorticity is calculated as

$$-\frac{\partial \bar{u}}{\partial y} = -10\,\frac{\mathrm{m}}{\mathrm{s}}\left(\frac{2\pi}{150000\ \mathrm{m}}\right)\cos\left(\frac{2\pi \mathrm{y}}{150\ \mathrm{km}}\right) \tag{2}$$

where y ranges from -75 km at the southern boundary to 75 km at the northern boundary resulting in a maximum absolute value of vorticity equaling $4 * 10^{-4}\ s^{-1}$. There is also horizontal vorticity associated with the vertical wind shear. This reaches a maximum value of

$$\frac{\partial \bar{u}}{\partial z} = \frac{20\frac{\mathrm{m}}{\mathrm{s}}}{3000\ \mathrm{m}} = 6.7 * 10^{-3}\ \mathrm{s}^{-1} \tag{3}$$

We perform a scale analysis in order to compare the magnitude of the vorticity tilting and stretching terms, using the horizontal and vertical environmental shear to define the environmental vertical and horizontal vorticity. Based on scale analysis, the ratio of stretching to tilting at the first scalar level is

$$\frac{\frac{\partial \bar{u}}{\partial y}D}{\frac{\partial \bar{u}}{\partial z}H} = \frac{(4*10^{-4}\ \mathrm{s}^{-1})(1000\ \mathrm{m})}{(6.7*10^{-3}\ \mathrm{s}^{-1})(50\ \mathrm{m})} = 1.2 \tag{4}$$

where D represents the approximate width of the updrafts produced in the simulation and 50 m is the depth over which the stretching and tilting would occur (this is also the height at which we analyzed vertical vorticity in our simulations). Thus, because the two vorticity source terms are comparable, it is possible for the environmental vorticity to be stretched into vortices by the updrafts to a magnitude similar to the environmental vorticity that was tilted into the updraft.

Indeed, in the center of our domain between the maximum and minimum shear, environmental vertical vorticity is negative, and we observed primarily negative vortices. We observed cyclonic vortices in the region north of the shear maximum and south of the shear minimum which is also where our environmental vertical vorticity would be positive. However, because we did not include baroclinic vorticity in our scale analysis, it is possible the tilting term is stronger.

An additional limitation to our results is that we also cannot definitively determine that vortices observed in our simulations would or would not produce tornadoes as the resolution used in our simulations is not sufficient to resolve the complicated dynamics associated with tornadogenesis. Rather, areas of enhanced vertical vorticity only represent regions favorable for tornado development.

Despite these limitations, we have shown that heterogeneous shear can have unique effects on vertical vorticity patterns as well as lifting along the cold pool and the associated updraft strength in a QLCS. These effects should be examined further in future studies.

Chapter 5

Conclusion

In this three-part study, we investigate the challenges of forecasting and warning QLCS tornadoes by evaluating the effectiveness of forecasting tools already widely in practice by the NWS and providing an analysis of 2 new tools to the QLCS space that may help to improve tornado warning lead time.

In chapter one, we examined 20 QLCS cases in order to evaluate the effectiveness of the “Three Ingredients Method” (3IM) proposed by Schaumann and Przybylinski (2012) in distinguishing between QLCSs that are likely and unlikely to produce tornadoes. We also investigated the utility of Confidence Builder and Nudger radar features (CB/N) proposed by the NWS Central Region Tornado Warning Improvement Project in determining when and where to issue tornado warnings along the leading edge of a QLCS. This was done by first identifying which of the 3 criteria in 3IM were satisfied for a particular QLCS. We then visually examined NEXRAD Level II radar data to identify the number of CB/N radar features present before:

1. Warnings verified with Local Storm Reports (LSRs)
2. Unverified Warnings
3. Unwarned LSRs

Consistent with other studies (Williamson et al. 2021; Gibbs 2021) we found 3IM to be an effective distinguisher between QLCSs that are likely and unlikely to produce tornadoes. However, further research is required to understand the role of 0-6 km shear in mesovortex development as a result of enhanced lifting via the updraft in shear effect in situations when the

0-3 km line normal shear is less than 30 kts. It is also possible that the line-normal shear requirement for balancing a cold pool is not rigid and instead depends on cold pool strength. Our results show the CB/N radar features used to help forecasters issue tornado warnings are ineffective in identifying parts of the QLCS that are most favorable for tornadogenesis to occur (Figure 9). These results are inconsistent with the findings in Gibbs (2021) and warrant further investigation given the subjective nature of identifying such features. However, the lack of clear predictive power and the challenges associated with issuing accurate tornado warnings as demonstrated in Table 1 still demonstrate more research is required to develop new tools for more accurate warnings.

In chapter two, we examined 18 tornadic QLCS events for K_{DP}/Z_{DR} separation occurring at the time of a reported tornado to determine its effectiveness as a warning tool. This was done using an algorithm developed in Python with Py-ART to objectively identify the closest regions of enhanced K_{DP} and Z_{DR} to a tornado report and compute the separation distance between them. We then performed a statistical analysis on the sample including producing a box plot, a 95% confidence interval, and a bootstrap sample to analyze its representation of all tornadic QLCS events. We found the mean K_{DP}/Z_{DR} separation distance to be 20.8 km with a standard deviation of 16.0 km. Despite the variation present in the sample, our statistical analysis indicates that if our sample is representative of the population, most K_{DP}/Z_{DR} separations are large enough such that they can be seen visually on radar, an important aspect for forecasters. However, our lack of focus on the null cases serves as a limitation to our results. Further research should analyze situations where QLCS tornadoes have failed to form, such as when an unverified warning has been issued. Also, future studies should include at least 30 cases to assume normality and include an analysis of the angle between K_{DP}/Z_{DR} separation and storm motion vectors. Despite these limitations, our study still serves as an important step towards improving QLCS tornado warnings and supports the concept of K_{DP}/Z_{DR} separation as a potential tool for forecasters to use when issuing warnings.

In chapter three, we performed a numerical simulation of 4 QLCSs in CM1 comparing vertical vorticity and velocity patterns across the homogeneous shear cases with 20, 15, and 10 m/s with a case of heterogeneous shear varying sinusoidally from 10 to 20 m/s in the N-S direction. We found the production of vortices along the gust front to be somewhat similar between the moderate and low shear homogenous cases while vortices were weaker and fewer in the homogeneous high shear simulation. We also found weak, disorganized updrafts in the high shear QLCS simulation. Future work should investigate situations in which high shear can lead to weaker QLCSs. Our heterogeneous simulation produced a QLCS with the weak shear segment bowing out to the east and the strong shear segment bowing out towards the west. The strongest updrafts occurred in the region of moderate shear, but where the 15 m/s 0-3 km line-normal shear threshold wasn’t satisfied as a result of the 45° orientation of the cold pool to the shear vector. This is a possible indication of the dependence of the shear threshold on the strength of the cold pool. We observed the strongest vortices to form along and just north of the northern bowing segment. This was contrary to our expectations due to the weak shear and updrafts in this location, but it is possible baroclinic generation of vorticity in the cold pool played a role. However, the presence of environmental vertical vorticity introduced by our variation of wind along the meridional direction of the domain may have contributed to the vertical vorticity pattern we observed. We hope future studies investigate this further and are able to distinguish between the different sources of vorticity more accurately. Future work should also further investigate the role of baroclinic vorticity patterns on the development of tornado-like vortices.

Our results highlight where current approaches to QLCS tornado forecasting and warning are effective, such as the use of 3IM, but also underline some of the weaknesses in the current process, including the subjective nature and uncertain skill of CB/N in deciding when and where to issue a tornado warning. The analysis of K_{DP}/Z_{DR} separation shows the potential to add skill to the forecasting process, but more studies are needed that provide a more robust statistical examination with more cases and investigate the internal mechanisms responsible for generating any separation of the two fields. Finally, our simulations of QLCSs in heterogeneous and varying homogeneous shear demonstrate potential caveats to the 0-3 km shear requirement and highlight the importance of understanding baroclinic processes in QLCS cold pools.

BIBLIOGRAPHY

Adlerman, E. J., and K. K. Droegemeier, 2005: The dependence of numerically simulated cyclic mesocyclogenesis upon environmental vertical wind shear. *Mon. Wea. Rev.*, **133**, 3595–3623, https://doi.org/10.1175/MWR3039.1.

Atkins, N. T., and M. St. Laurent, 2009a: Bow echo mesovortices. Part I: Processes that influence their damaging potential. *Mon. Wea. Rev.*, **137**, 1497–1513.

Atkins, N. T. and M. St. Laurent, 2009b: Bow Echo Mesovortices. Part II: Their Genesis. Mon. Wea. Rev., 137, 1514–1532.

Anderson-Frey, A. K., Y. P. Richardson, A. R. Dean, R. L. Thompson, and B. T. Smith, 2016: Investigation of near-storm environment for tornado events and warnings. *Wea. Forecasting*, **31**, 1771–1790, https://doi.org/10.1175/WAF-D-16-0046.1.

Brooks, H. E., J. W. Lee, and J. P. Craven, 2003: The spatial distribution of severe thunderstorm and tornado environments from global reanalysis data. *Atmos. Res.*, **67–68**, 73–94, https://doi.org/10.1016/S0169-8095(03)00045-0.

Bryan, G. H., and J. M. Fritsch, 2002: A benchmark simulation for moist nonhydrostatic numerical models. *Mon. Wea. Rev.*, 130, 2917–2928, doi:10.1175/1520-0493(2002)130<2917:ABSFMN>2.0.CO;2.

Carbone, R. E., 1982: A severe frontal rainband. Part I. Stormwide hydrodynamic structure. *J. Atmos. Sci.*, **39**, 258–279, https://doi.org/10.1175/1520-0469(1982)039<0258:ASFRPI>2.0.CO;2.

Carbone, R. E., 1983: A severe frontal rainband. Part II: Tornado parent vortex circulation. *J. Atmos. Sci.*, **40**, 2639–2654, https://doi.org/10.1175/1520-0469(1983)040<2639:ASFRPI>2.0.CO;2.

Coffer, B. E., and M. D. Parker, 2017: Simulated supercells in nontornadic and tornadic VORTEX2 environments. *Mon. Wea. Rev.*, **145**, 149–180, https://doi.org/10.1175/MWR-D-16-0226.1.

Crowe, C. C., C. J. Schultz, M. Kumjian, L. D. Carey, and W. A. Petersen, 2012: Use of dual-polarization signatures in diagnosing tornadic potential. *Electron. J. Oper. Meteor.*, **13** (5), 57–78, http://www (nwas.org).

Esterheld, J. M., and D. J. Giuliano, 2008: Discriminating between tornadic and non-tornadic supercells: A new hodograph technique. *Electron. J. Severe Storms Meteor.*, **3** (2), http://www.ejssm.org/ojs/index.php/ejssm/article/viewArticle/33.

Gibbs, J. G., 2021: Evaluating precursor signals for QLCS tornado and higher impact straight-line wind events. J. Operational Meteor., 9 (5), 62-75, doi: https://doi.org/10.15191/nwajom.2021.0905.

Helmus, J.J. & Collis, S.M., (2016). The Python ARM Radar Toolkit (Py-ART), a Library for Working with Weather Radar Data in the Python Programming Language. Journal of Open Research Software. 4(1), p.e25. DOI: http://doi.org/10.5334/jors.119.

Kumjian, M.R., and A. Ryzhkov, 2008a: Polarimetric signatures in supercell thunderstorms. J. Appl. Meteor., 47, 1940-1961.

Kumjian, M.R., and A. Ryzhkov, 2009: Storm-relative helicity revealed from polarimetric radar measurements. J. Atmos. Sci., 66, 667-685.

Lee, B. D., and R. B. Wilhelmson, 1997a: The numerical simulation of non-supercell tornadogenesis. Part I: Initiation and evolution of pretornadic misocyclone circulations along a dry outflow boundary. J. Atmos. Sci., 54, 32–60, https://doi.org/10.1175/1520-0469(1997)054<0032:TNSONS>2.0.CO;2.

Lee, B. D., and R. B. Wilhelmson, 1997b: The numerical simulation of non-supercell tornadogenesis. Part II: Evolution of a family of tornadoes along a weak outflow boundary. *J. Atmos. Sci.*, **54**, 2387–2415, https://doi.org/10.1175/1520-0469(1997)054<2387:TNSONT>2.0.CO;2.

Loeffler, S., and M. R. Kumjian, 2018: Quantifying the separation of enhanced *Z*DR and *K*DP regions in nonsupercell tornadic storms. *Wea. Forecasting*, **33**, 1143–1157, https://doi.org/10.1175/WAF-D-18-0011.1.

Maesaka, T., K. Iwanami, and M. Maki, 2012: Non-negative *K*DP estimation by monotone increasing ΦDP assumption below melting layer. *Seventh European Conf. on Radar in Meteorology and Hydrology*, Toulouse, France, ERAD, http://www.meteo.fr/cic/meetings/2012/ERAD/extended_abs/QPE_233_ext_abs.pdf.

Romine, G.S., D.W. Burgess, and R.B. Wilhelmson, 2008: A dual-polarization-radar-based 77 assessment of the 8 May 2003 Oklahoma City area tornadic supercell. Mon. Wea. Rev., 136, 2849-2870, https://doi.org/10.1175/2008MWR2330.1.

Rotunno, R., J. B. Klemp, and M. L. Weisman, 1988: A theory for strong, long-lived squall lines. *J. Atmos. Sci.*, **45**, 463–485, https://doi.org/10.1175/1520-0469(1988)045<0463:ATFSLL>2.0.CO;2.

Schaumann, J. and A. Cohen: Using Deep Shear to Help Anticipate Forthcoming QLCS Mesovortices. *NWS Central Region Tornado Warning Improvement Project.*

Schaumann, J. S., and R. W. Przybylinski, 2012: Operational application of 0–3 km bulk shear vectors in assessing QLCS mesovortex and tornado potential. Preprints, 26th Conf. on Severe Local Storms, Nashville, TN, Amer. Meteor. Soc., 9.10.

Sherburn, K. D., and M. D. Parker, 2019: The development of severe vortices within simulated high-shear, low-CAPE convection. *Mon. Wea. Rev.*, **147**, 2189–2216, https://doi.org/10.1175/MWR-D-18-0246.1.

Smith, B. T., R. L. Thompson, A. R. Dean, and P. T. Marsh, 2015: Diagnosing the conditional probability of tornado damage rating using environmental and radar attributes. *Wea. Forecasting*, **30**, 914–932, https://doi.org/10.1175/WAF-D-14-00122.1.

Thompson, R.L., B. T. Smith, J. S. Grams, A. R. Dean, and C. Broyles, 2012: Convective modes for significant severe thunderstorms in the contiguous United States. Part II: Supercell and QLCS tornado environments. Wea. Forecasting, 27, 1136–1154.

Trapp, R. J., Mitchell E. D. , Tipton G. A. , Effertz D. W. , Watson A. I. , Andra D. L. Jr., and Magsig M. A. , 1999: Descending and non-descending tornadic vortex signatures detected by WSR-88Ds. *Wea. Forecasting*, **14 ,** 625–639.

Trapp, R. J., S. A. Tessendorf, E. S. Godfrey, and H. E. Brooks, 2005: Tornadoes from squall lines and bow echoes. Part I: Climatological distribution. *Wea. Forecasting*, **20**, 23–34, https://doi.org/10.1175/WAF-835.1.

Weisman, M. L., and J. B. Klemp, 1982: The dependence of convective storms on vertical wind shear and buoyancy. *Mon. Wea. Rev.*, **110 ,** 50–66.

Weisman, M. L. and R. W. Przybylinski, 1999: Mesoscale convective systems: Squall lines and bow echoes, COMET CBL module, UCAR.

Weisman, M. L., and R. J. Trapp, 2003: Low-level mesovortices within squall lines and bow echoes. Part I: Overview and dependence on environmental shear. *Mon. Wea. Rev.*, **131**, 2779–2803, https://doi.org/10.1175/1520-0493(2003)131<2779:LMWSLA>2.0.CO;2.

Wicker, L. J., and R. B. Wilhelmson, 1995: Simulation and analysis of tornado development and decay within a three-dimensional supercell thunderstorm. *J. Atmos. Sci.*, **52**, 2675–2703, https://doi.org/10.1175/1520-0469(1995)052<2675:SAAOTD>2.0.CO;2.

Williams, B. M., J. S. Allen, and J. W. Zeitler, 2018: Anticipating QLCS tornadogenesis for decision support: The three-ingredient method during the 19–20 February 2017 south-central Texas tornadic QLCS event. *Major Weather Events and Impacts of 2017*, Austin, TX, Amer. Meteor. Soc., 375, https://ams.confex.com/ams/98Annual/webprogram/Paper331351.html.

Wilson, M.B.; Van Den Broeke, M.S. An automated Python algorithm to quantify ZDR arcs and KDP-ZDR separation signatures in supercells. J. Atmos. Ocean. Technol. 2021, 38, 371–386.

Table 1. List of the date, number of tornadoes, probability of detection (POD), and false alarm ratio (FAR) for each tornadic QLCS event. Note: The 7 March 2016 case was omitted due to warning issuance while the tornado was on the ground.

Date	Number of Tornados	POD (Warned LSRs/Total LSRs)	FAR (Unverified Warnings/Total Warnings)
07/14/2020	4	1	0.75
07/17/2020	1	0	0
09/10/2019	1	1	0.8
06/28/2018	5	1	0.25
08/17/2019	7	0.29	0
06/17/2020	2	0.5	0.5
07/07/2020	1	1	0.75
07/28/2021	6	0.17	0.67
03/28/2017	3	0.00	1
Average		0.15	0.52

Table 2. List of the date, radar site, time of tornado and radar scan, and the tornado latitude and longitude for each of the 18 cases used for the K_{DP}/Z_{DR} separation analysis. Only the radar images at the volume scan time (VST) were able to be analyzed in Py-ART.

Radar	Date	Time of Tornado	Radar Scan Time (VST)	Tornado Latitude	Tornado Longitude
KPUX	7/15/2020	1:00z	00:57:50z	38.03	-103.26
KMVK	7/17/2020	21:54z	21:53:35z	48.35	-96.86
KFSD	9/10/2019	4:25z	04:23:41z	43.48	-96.74
KMVK	6/29/2018	8:52z	08:51:53z	47.76	-97.57
KMVK	6/29/2018	9:48z	09:45:16z	47.27	-96.26
KMVK	6/29/2018	9:54z	09:51:33z	47.55	-96.02
KMVK	6/29/2018	9:56z	09:57:51z	47.64	-96
KFSD	8/18/2019	3:34z	03:33:16z	43.42	-96.15
KFSD	8/18/2019	3:57z	03:57:12z	44	-95.86
KFSD	8/18/2019	3:59z	04:02:53z	43.72	-95.75
KFSD	8/18/2019	3:59z	04:02:53z	43.91	-95.78
KMVK	6/18/2020	1:42z	01:42:25z	48.23	-96.72
KBIS	7/8/2020	4:30z	04:28:29z	47.22	-100.99
KMKX	7/29/2021	5:12z	05:15:36z	43.49	-89.46
KMKX	7/29/2021	5:39z	05:41:16z	43.11	-89.65
KFWS	3/8/2016	0:08z	00:09:26z	32.79	-97.98
KFWS	3/28/2017	7:08z	07:08:29z	32.92	-97.38
KFWS	3/28/2017	7:31z	07:31:33z	33.05	-97.03

Table 3. A list of initial conditions describing the setup of our numerical simulations in CM1

Domain	150 x 150 x 20 km^3
Horizontal Grid Spacing	250 m
Vertical Grid Spacing	100 m
Upper, Lower Boundary Conditions	Free Slip
E-W Lateral Boundary Conditions	Open, Wave Radiative
N-S Lateral Boundary Conditions	Periodic
Microphysical Parametrization	Morrison Double-Moment (Morrison et al. 2005)
Turbulence	TKE (Deardorff 1980)

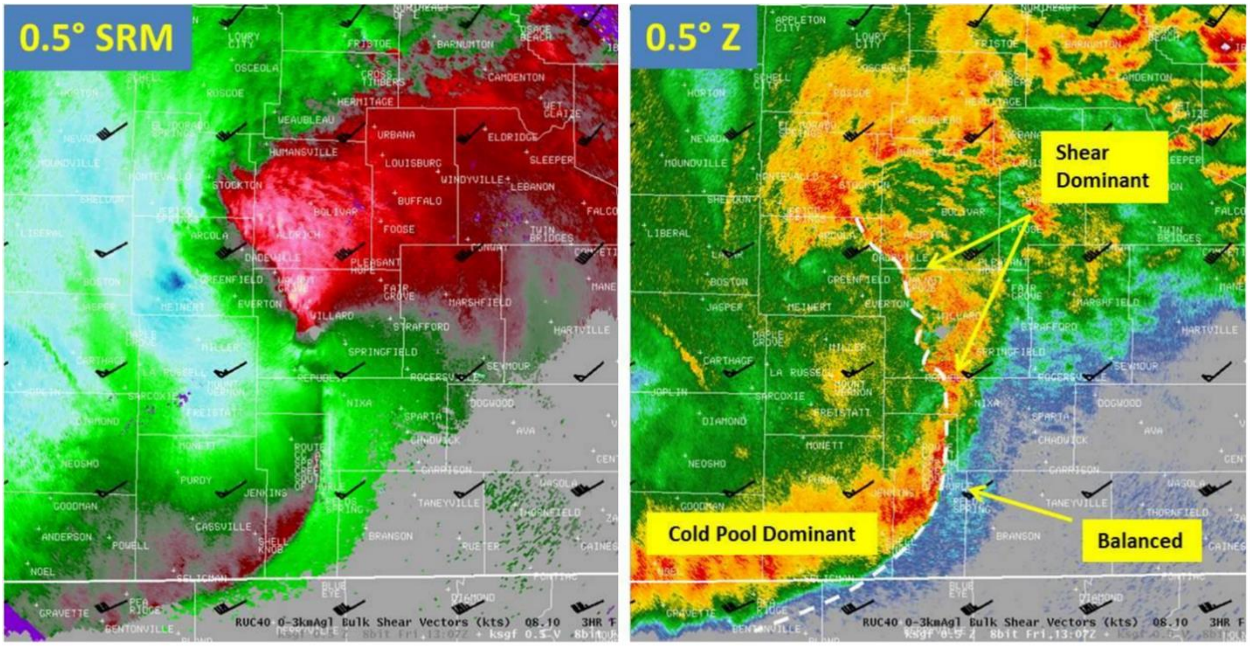

Figure 1. These radar images depict the 8 May 2009 super-derecho as it was moving into Springfield, MO. The updraft downdraft convergence zone (UDCZ) is readily apparent on the 0.5° Storm-Relative Motion (SRM) image (left). Comparison of the UDCZ (dashed white line in right image) to 0.5° reflectivity (Z) effectively highlights differing shear/cold pool balance regimes. 0-3 km bulk shear vectors (knots) are overlaid in black (Figure 8 from Schaumann and Przybylinski 2012).

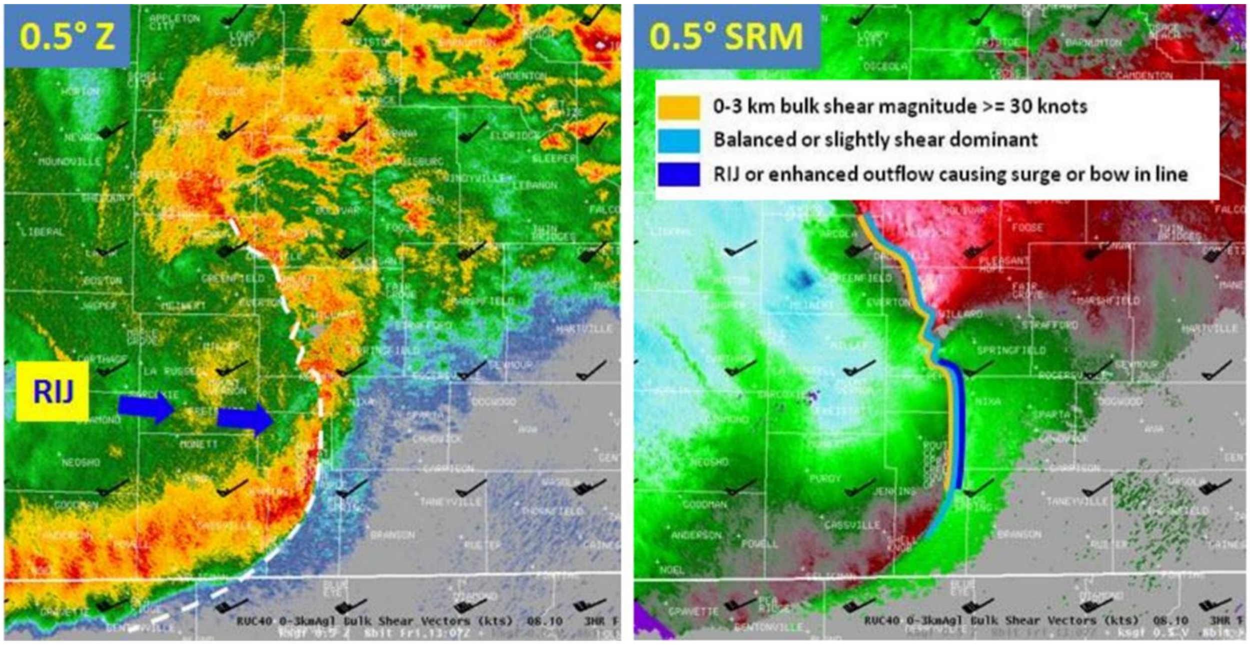

Figure 2. These radar images of the 8 May 2009 super-derecho are valid at the same time as those in Figure 1. 0-3 km bulk shear vectors (knots) are overlaid in black. The left image depicts 0.5° reflectivity (Z) with the location of an impinging rear-inflow jet (RIJ). The UDCZ is denoted by a dashed white line. The right image then depicts 0.5° SRM and color-codes portions of the UDCZ based on the three ingredients favorable for mesovortex genesis and intensification. The light orange shading highlights areas of the QLCS where 0-3 km line-normal bulk shear magnitude was equal to or greater than 15 m/s (30 knots). The pale blue shading depicts areas of the QLCS that were balanced or slightly shear dominant. The dark blue shading highlights areas of the QLCS where a descending RIJ resulted in a bow structure in the line (Figure 9 from Schaumann and Przybylinski 2012).

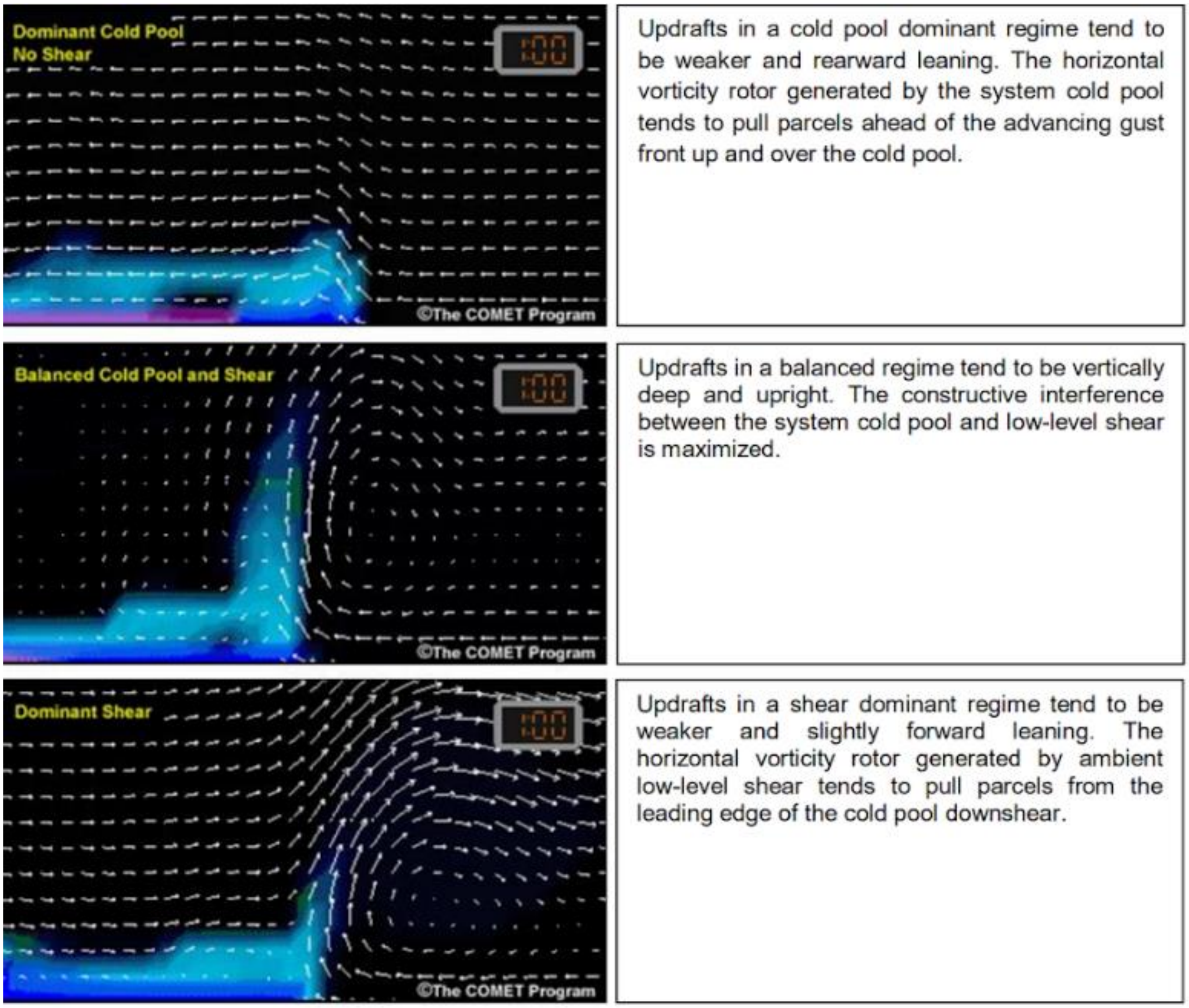

Figure 3. The three different outcomes of ambient shear and system cold pool interaction. White arrows represent the wind vectors while the blue shading indicates the QLCS cold pool. Figure adapted from Weisman and Przybylinski (1999) through COMET.

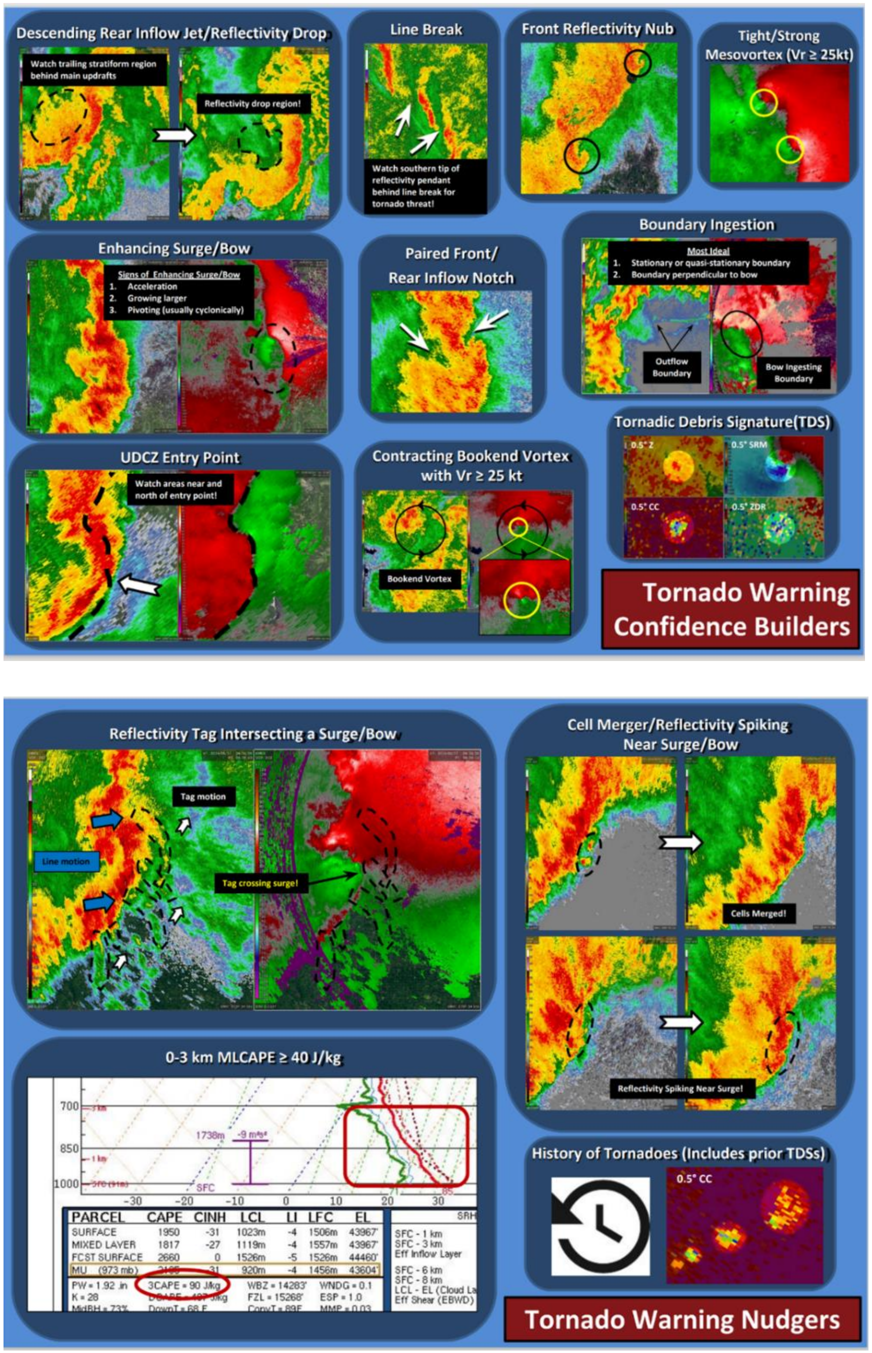

Figure 4. A list of radar features referred to as confidence builders and nudgers (CB/N) which are proposed as indicators of subsequent QLCS tornadogenesis. This is part of the QLCS Mesovortex Warning System Reference Sheet developed by the NWS Central Region Tornado Warning Improvement Project.

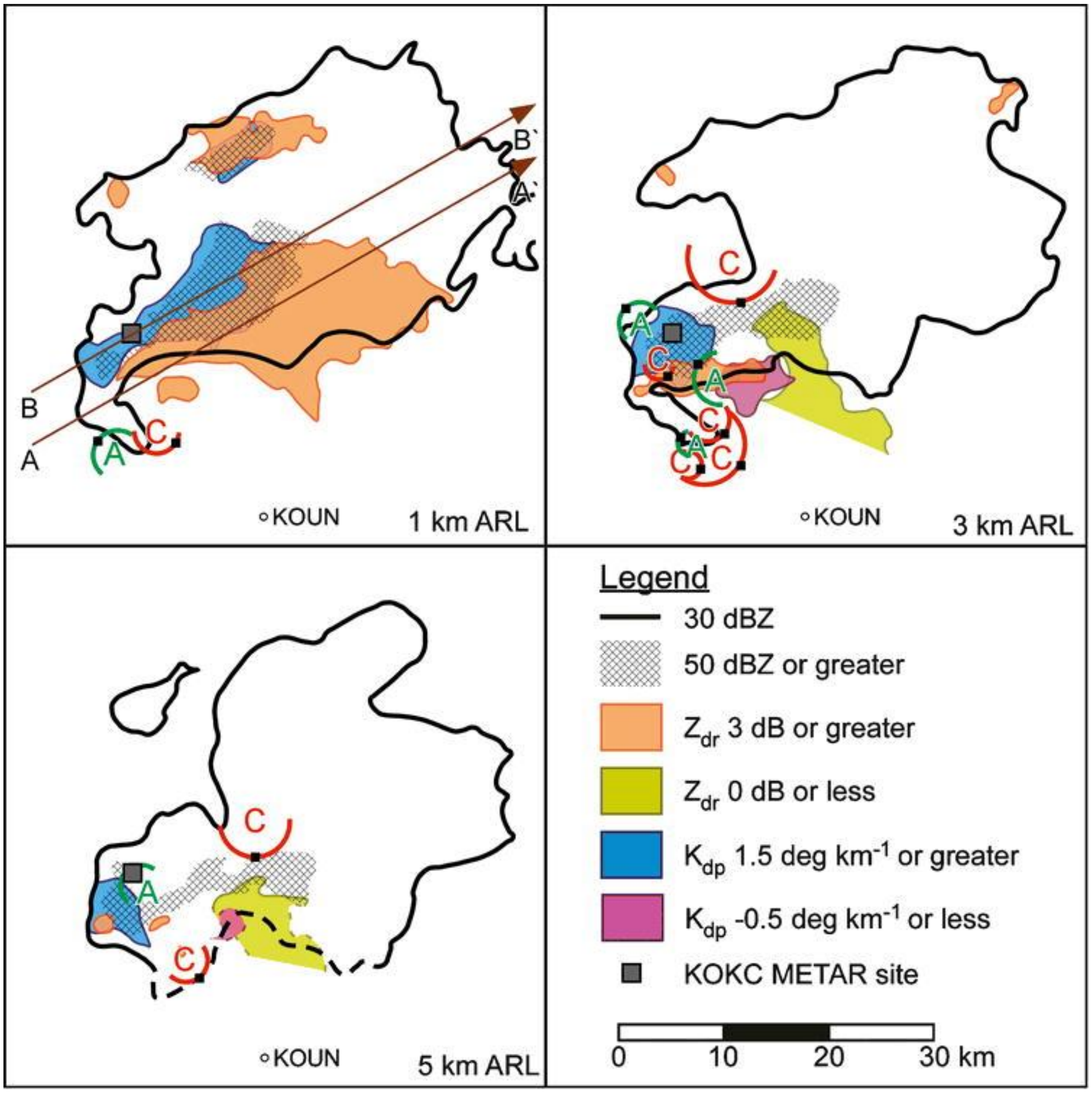

Figure 5. Constant altitude plan position indicator (CAPPI) plots at (top left) 1, (top right) 3, and (bottom left) 5 km above radar level (ARL) at 2204 UTC on 8 May 2003 with 30-dBZ contour of the radar reflectivity (heavy black) (dashed contours are extrapolated estimates within the radar's cone of silence) and regions with 50 dBZ or greater hatched; (bottom right) regions of $Z_{DR} \geq 3$ and ≤ 0 dB and K_{DP} areas ≥ 1.5 and $\leq -0.5°$ km−1 color filled following the legend. Additionally, cyclonic (anticyclonic) azimuthal shear is shown by red (green) half-circles between opposing storm-relative radial wind maxima with shear centroids labeled as C (A), and black boxes indicating couplet alignment relative to the radar position (radial convergence–divergence; Figure 12 from Romine et al. 2008).

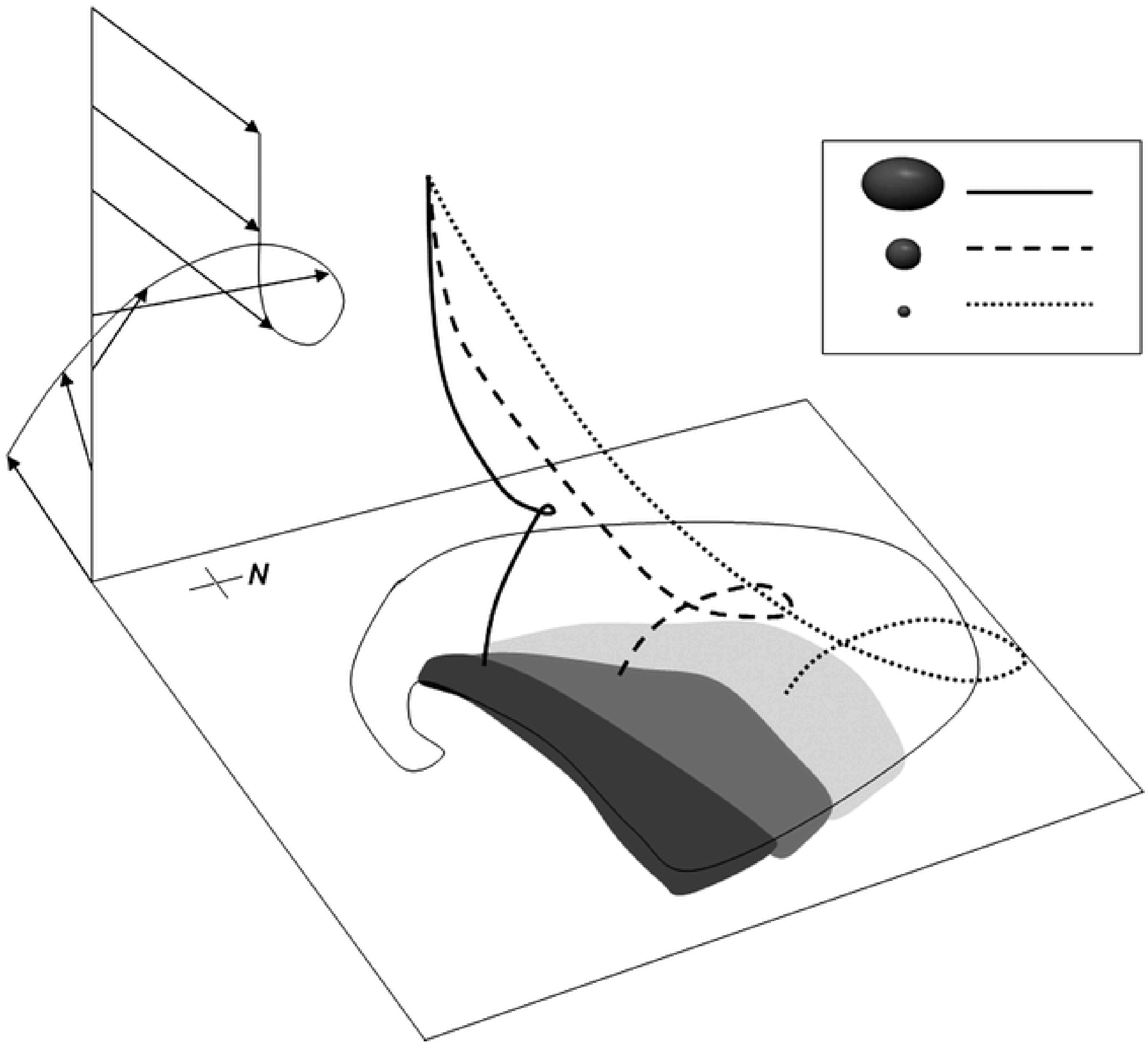

Figure 6. Schematic depiction of how low-level veering winds in a supercell storm-relative frame lead to an enhancement of Z_{DR} along the right (inflow) edge of the forward-flank downdraft precipitation echo (outlined on the surface). The wind vectors indicate the veering flow. If projected onto a horizontal plane, the line connecting the wind vectors would represent the hodograph, the area of which is proportional to the low-level storm relative helicity (SRH). Cyclonic trajectories are shown for large drops (black solid line), medium sized drops (dashed line), and small drops (dotted line) falling from a point source. The shading represents the Z_{DR} enhancement, which is maximized at the edge of the forward-flank downdraft (Figure 2 from Kumjian and Ryzhkov 2009).

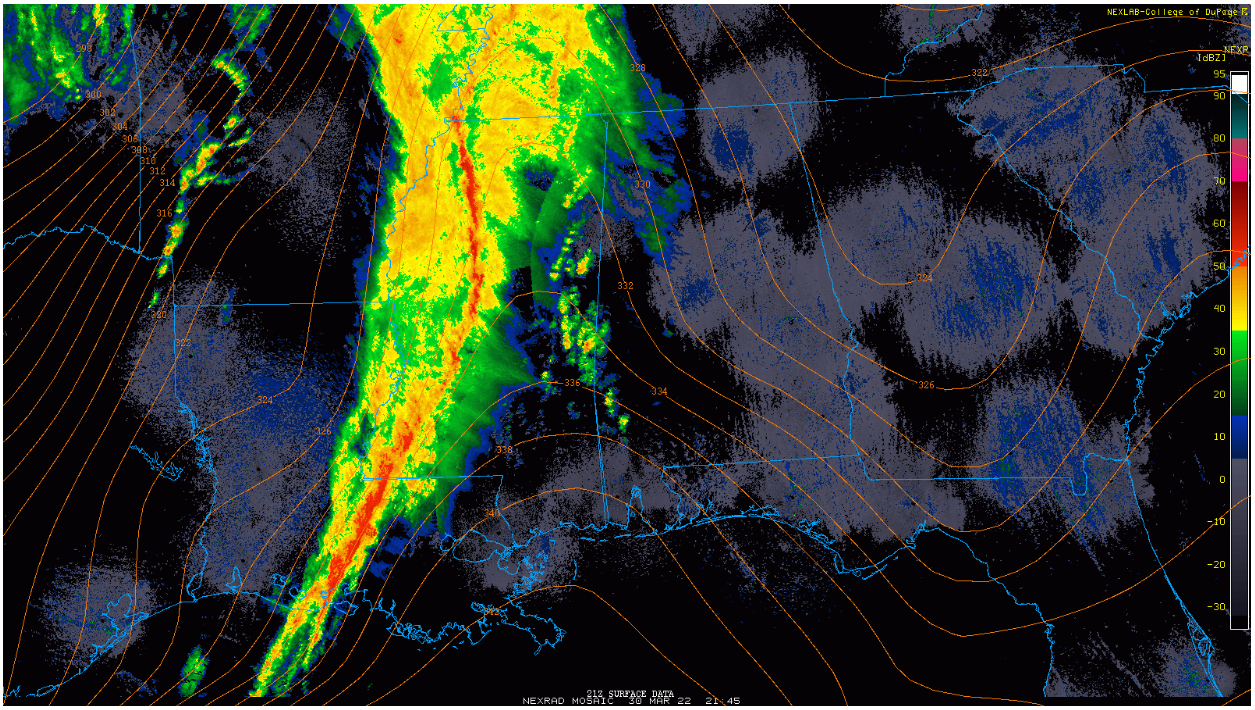

Figure 7. An example of environmental heterogeneity encountered by a tornadic QLCS near the Gulf of Mexico. The brown contours represent θ_e superimposed on a composite radar image of reflectivity. This particular image was generated on 30 March 2022 at 21z. Image retrieved from the College of DuPage NeXt Generation Weather Lab.

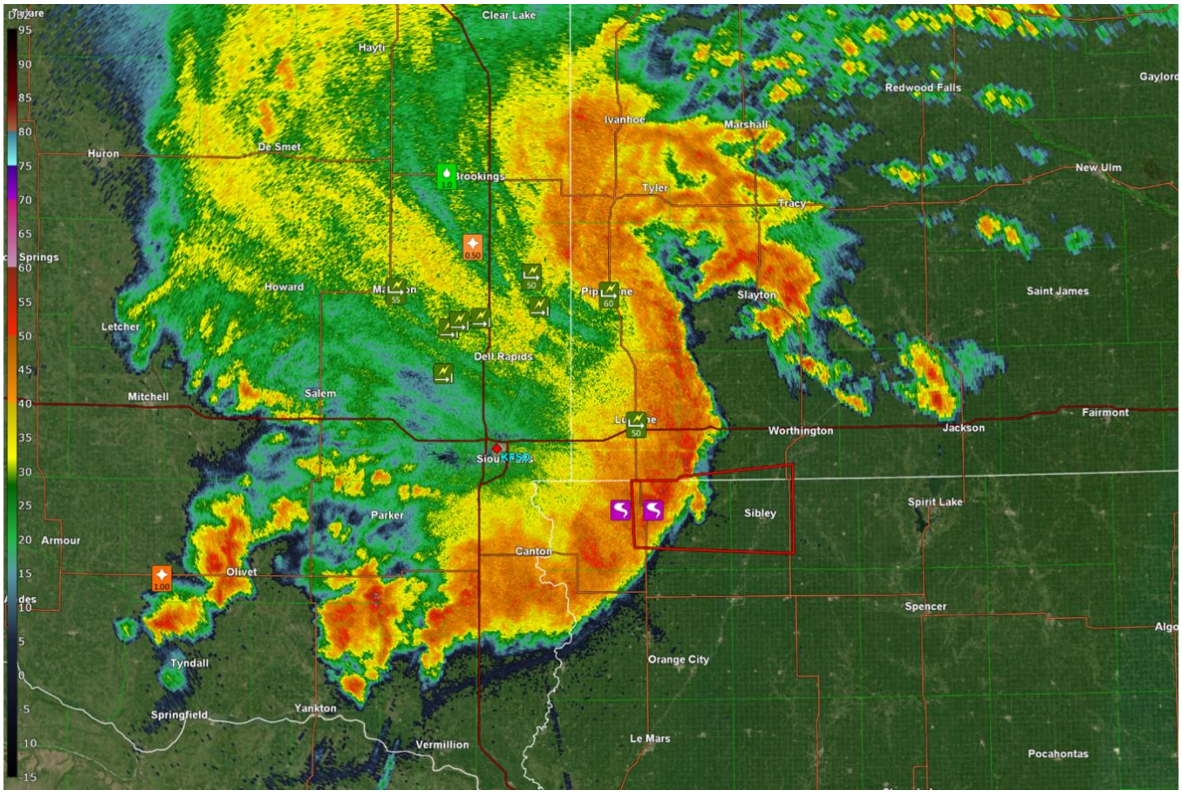

Figure 8. An example of how the Gibson Ridge radar software (GR2Analyst) was used to analyze each QLCS for the reflectivity criteria to satisfy the "Three Ingredients Method" as well as determine how many CB/N were present prior to each reported tornado and warning. This particular image was taken from the 17 August 2019 QLCS at 3:41z. The red polygon represents a tornado warning, and the purple icons show the location of a reported tornado.

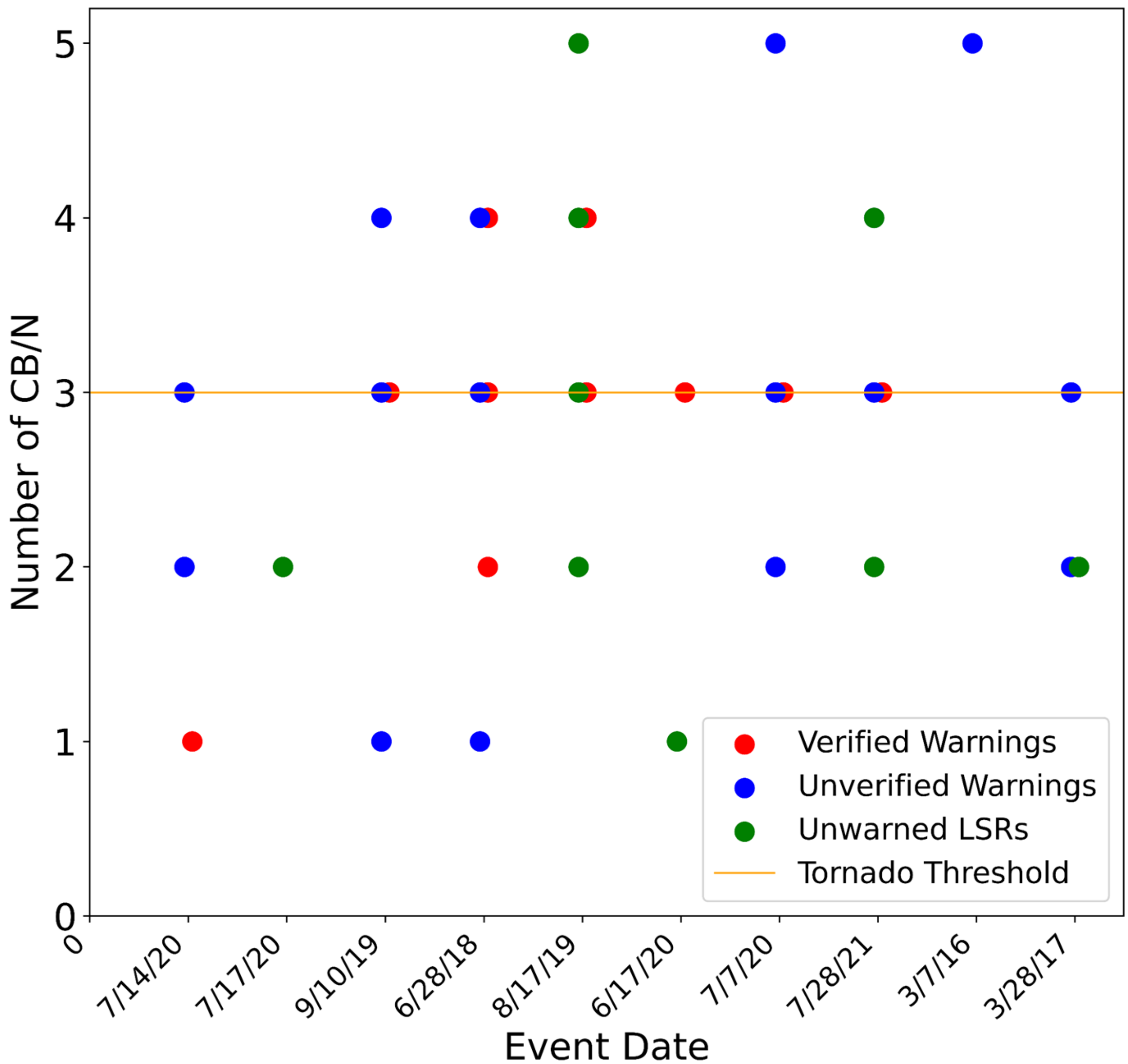

Figure 9. A scatter plot showing the number of CB/N (y axis) present prior to each warning verified with a tornado report (red dot), unverified warning (blue dot), and unwarned tornadic local storm report (LSR) (green dot) for each QLCS event (x axis). The yellow line represents the tornado threshold based on the scale in Figure 10 which shows the number of CB/N which are supposed to be strongly indicative of a tornado forming.

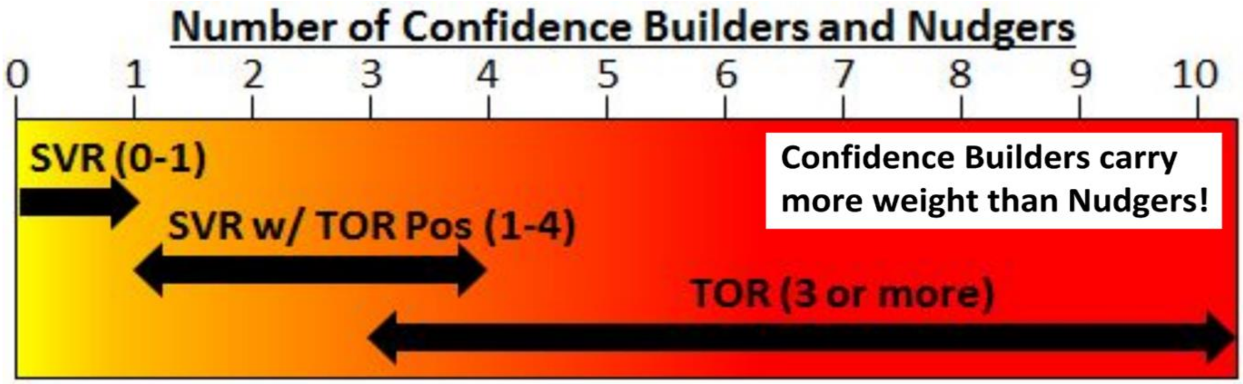

Figure 10. A scale from 1-10 showing the proposed CB/N threshold for which tornadoes are possible. A threshold of 3 was used in Figure 5. Adapted from the Mesovortex Warning System Reference Sheet developed by the NWS Central Region Tornado Warning Improvement Project.

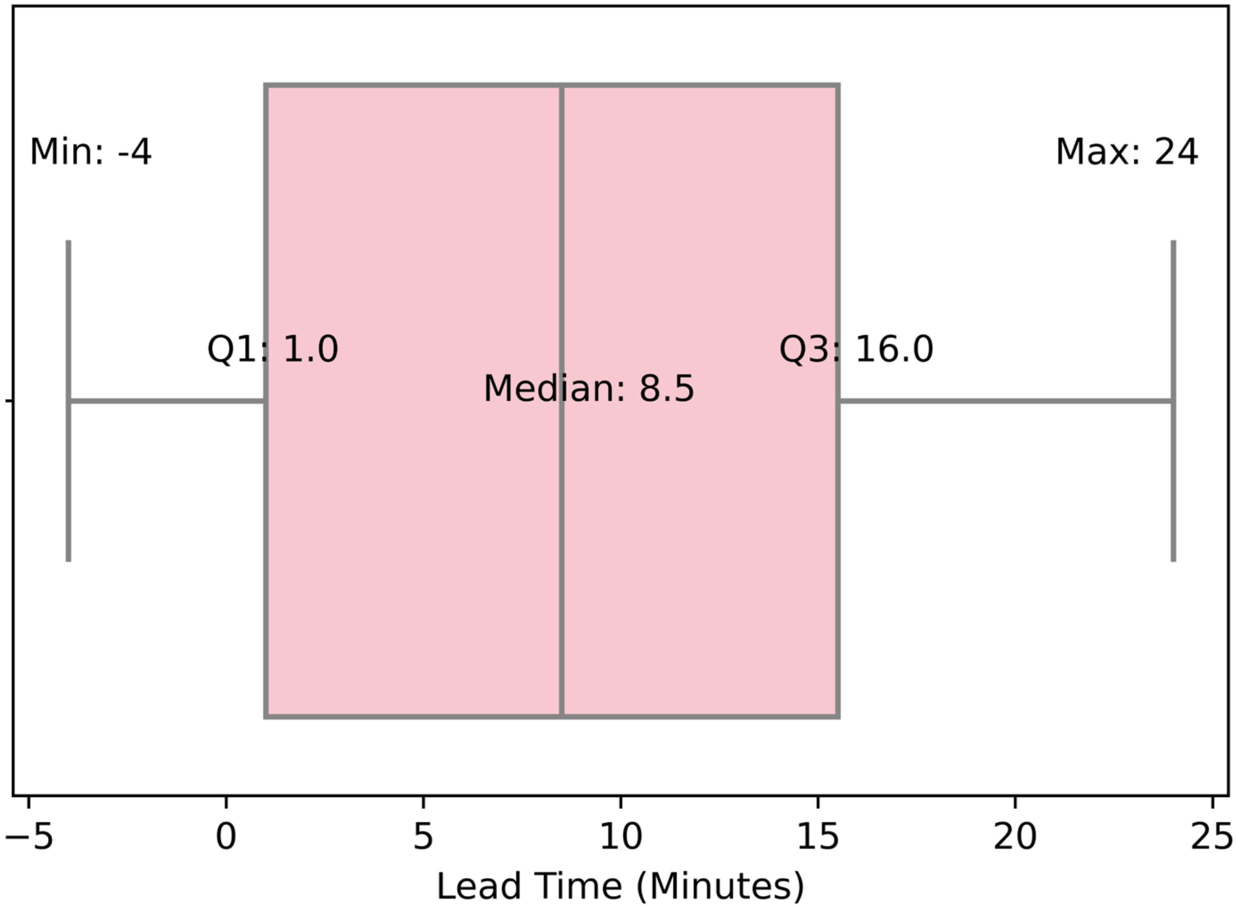

Figure 11. A boxplot of QLCS tornado lead time (minutes) from the 10 tornadic QLCSs in chapter one of this study with a range from -4 to 24, a median of 8.5, a first quartile of 1.0, and a third quartile of 16.0 minutes. The minimum value of -4 represents a warning that was issued after a tornado had touched down which occurred on 7 March 2016.

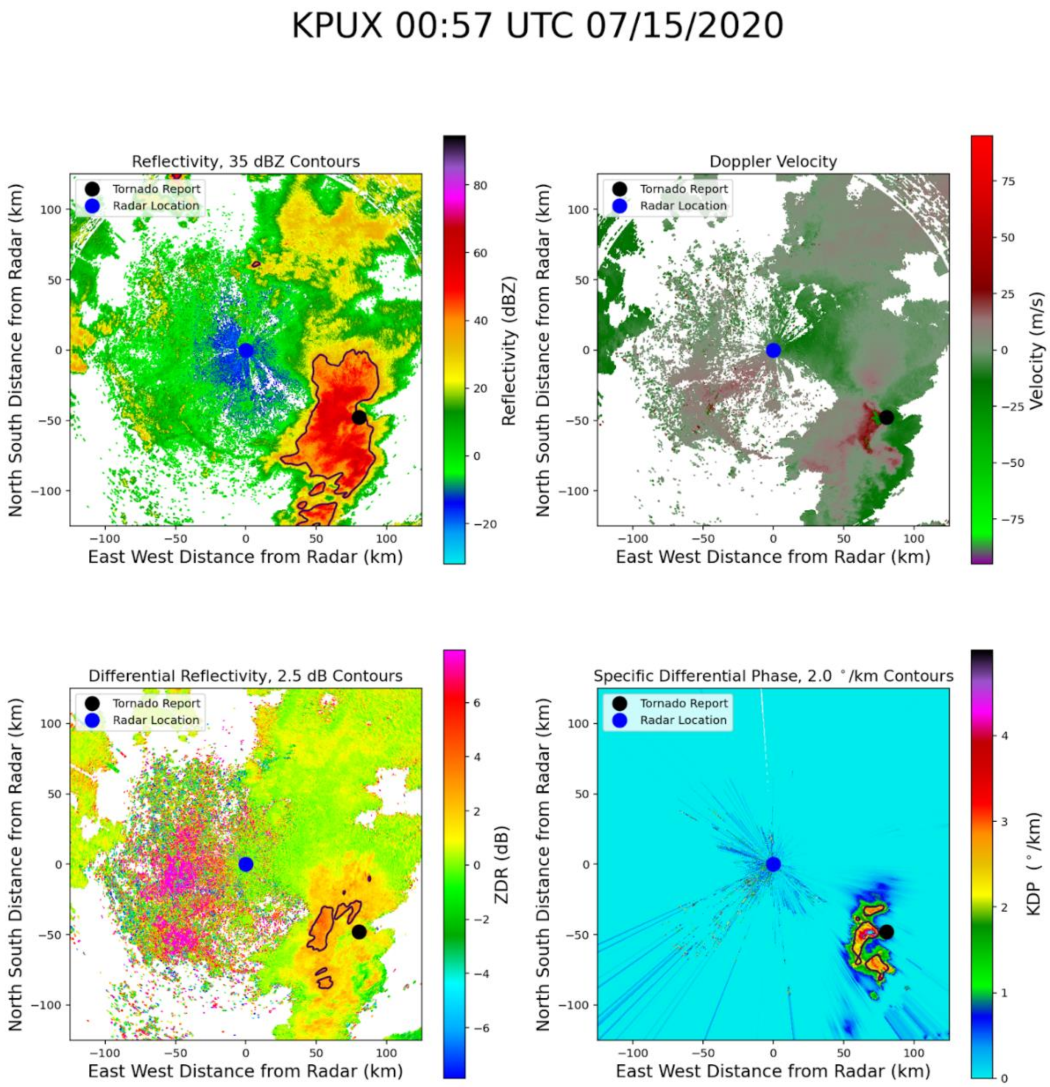

Figure 12. Plots of reflectivity contoured at 35 dBZ, doppler velocity, differential reflectivity (Z_{DR}) contoured at 2.5 dB, and specific differential phase (K_{DP}) contoured at 2.0 deg/km. These radar images were produced by the KPUX radar at 0:57z on 7/15/2020. The black dot indicates the location of the tornado report, and the blue dot represents the location of the radar which is always at (0,0).

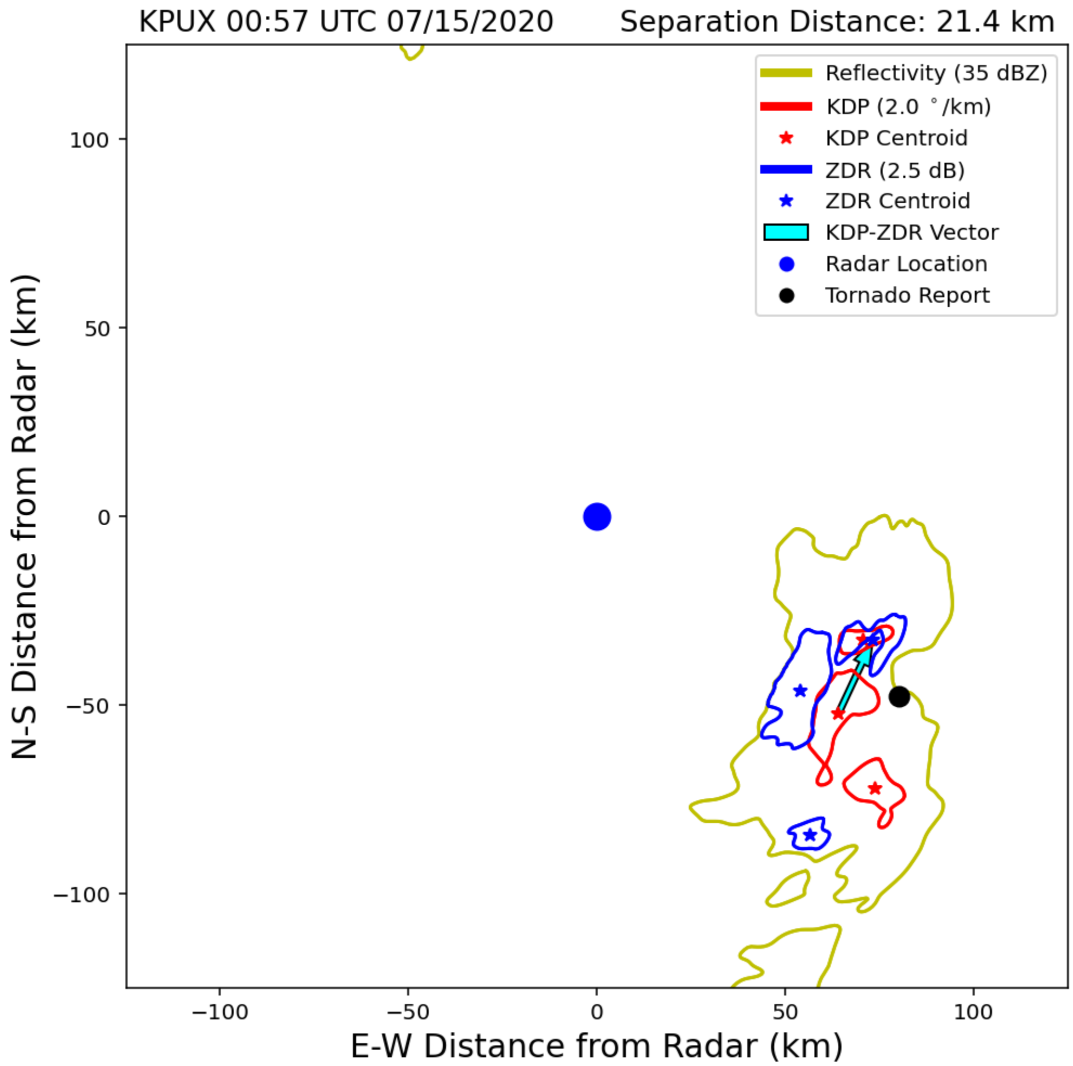

Figure 13. Contours of reflectivity at 35 dBZ (yellow lines), K_{DP} at 2.0 deg/km (red lines), and Z_{DR} at 2.5 dB (blue lines). This image was produced with data from the KPUX radar at 0:57z on 7/15/2020. The red and blue stars represent the K_{DP} and Z_{DR} centroids respectively. The light blue arrow is the K_{DP}/Z_{DR} separation vector with a magnitude of 21.4 km. The black dot indicates the location of the tornado report, and the blue dot represents the location of the radar which is always at (0,0).

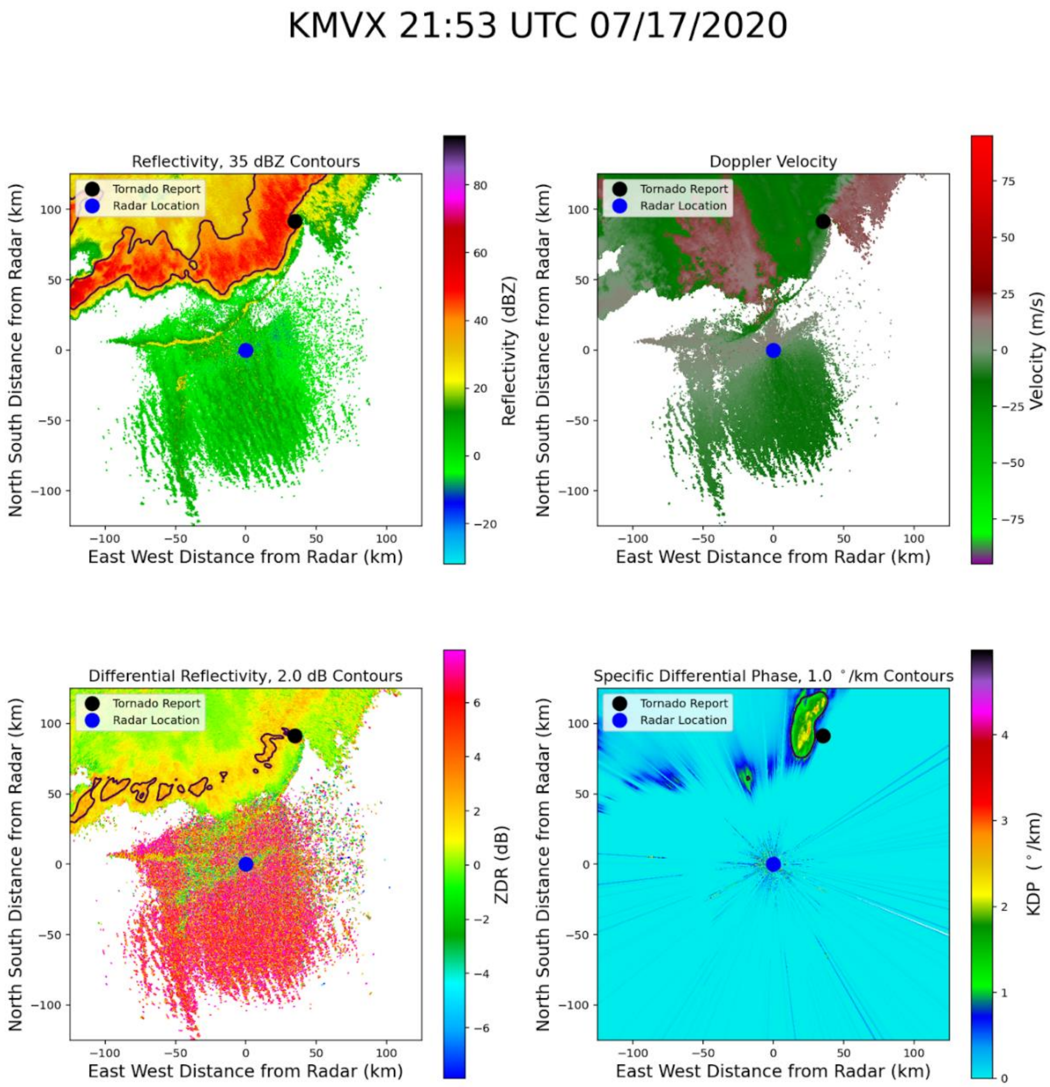

Figure 14. As in Figure 12, but for the KMVX radar at 21:53z on 7/17/2020 and for Z_{DR} and K_{DP} contours of 2.0 dB and 1.0 deg/km respectively.

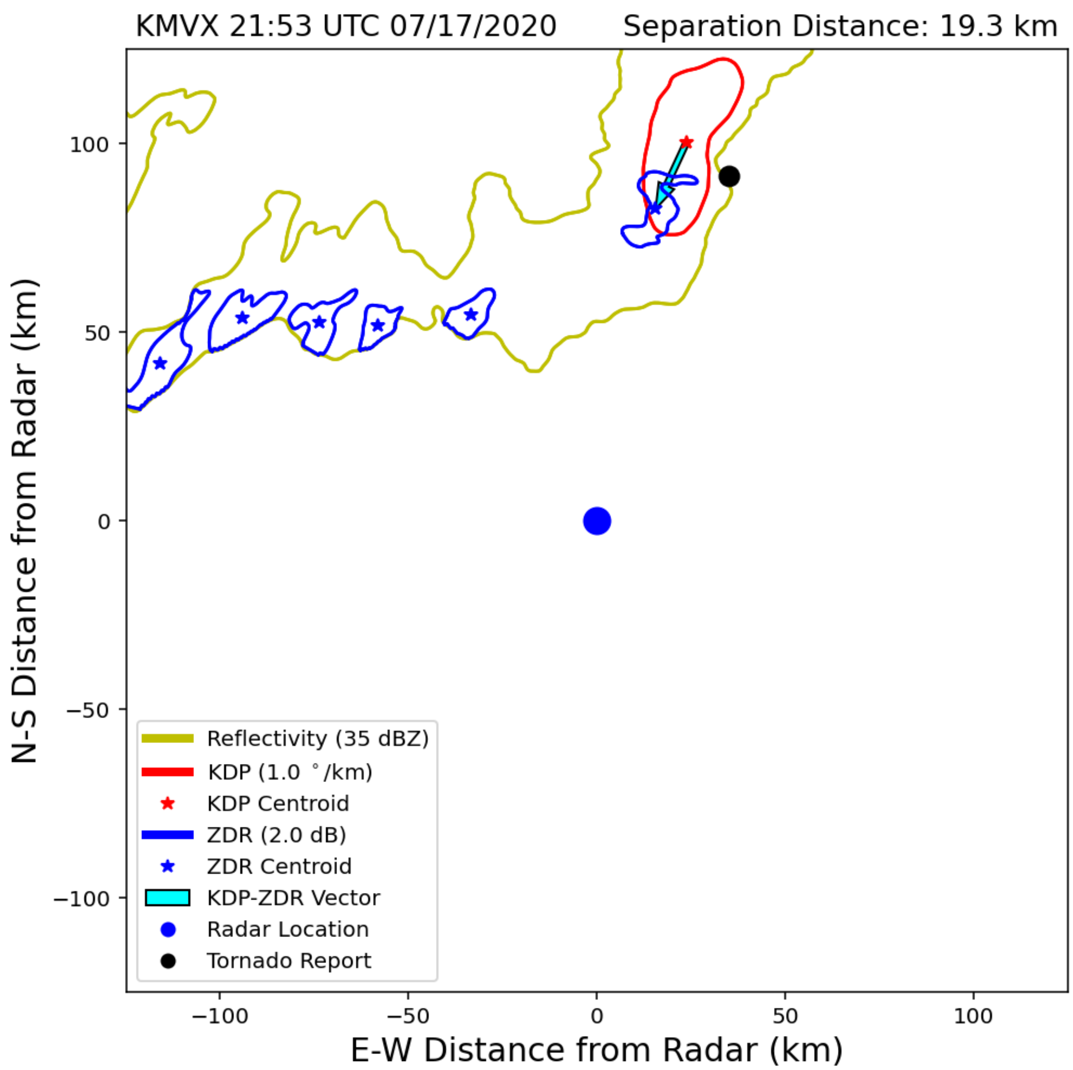

Figure 15. As in Figure 13 but for the KMVX radar at 21:53z on 7/17/2020, for Z_{DR} and K_{DP} contours of 2.0 dB and 1.0 deg/km respectively, and a K_{DP}/Z_{DR} separation vector magnitude of 19.3 km

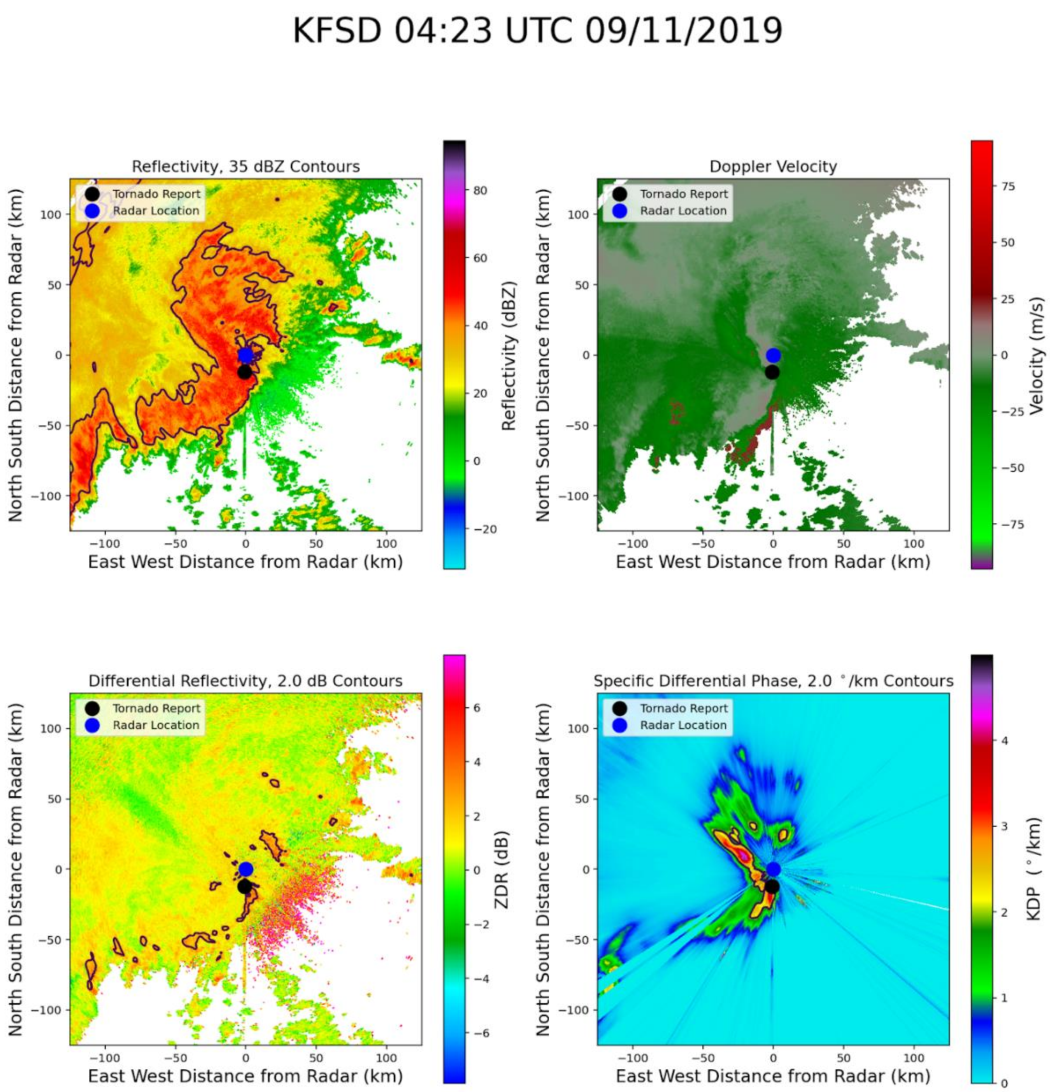

Figure 16. As in Figure 12, but for the KFSD radar at 4:23z on 9/11/2019 and for Z_{DR} and K_{DP} contours of 2.0 dB and 2.0 deg/km respectively.

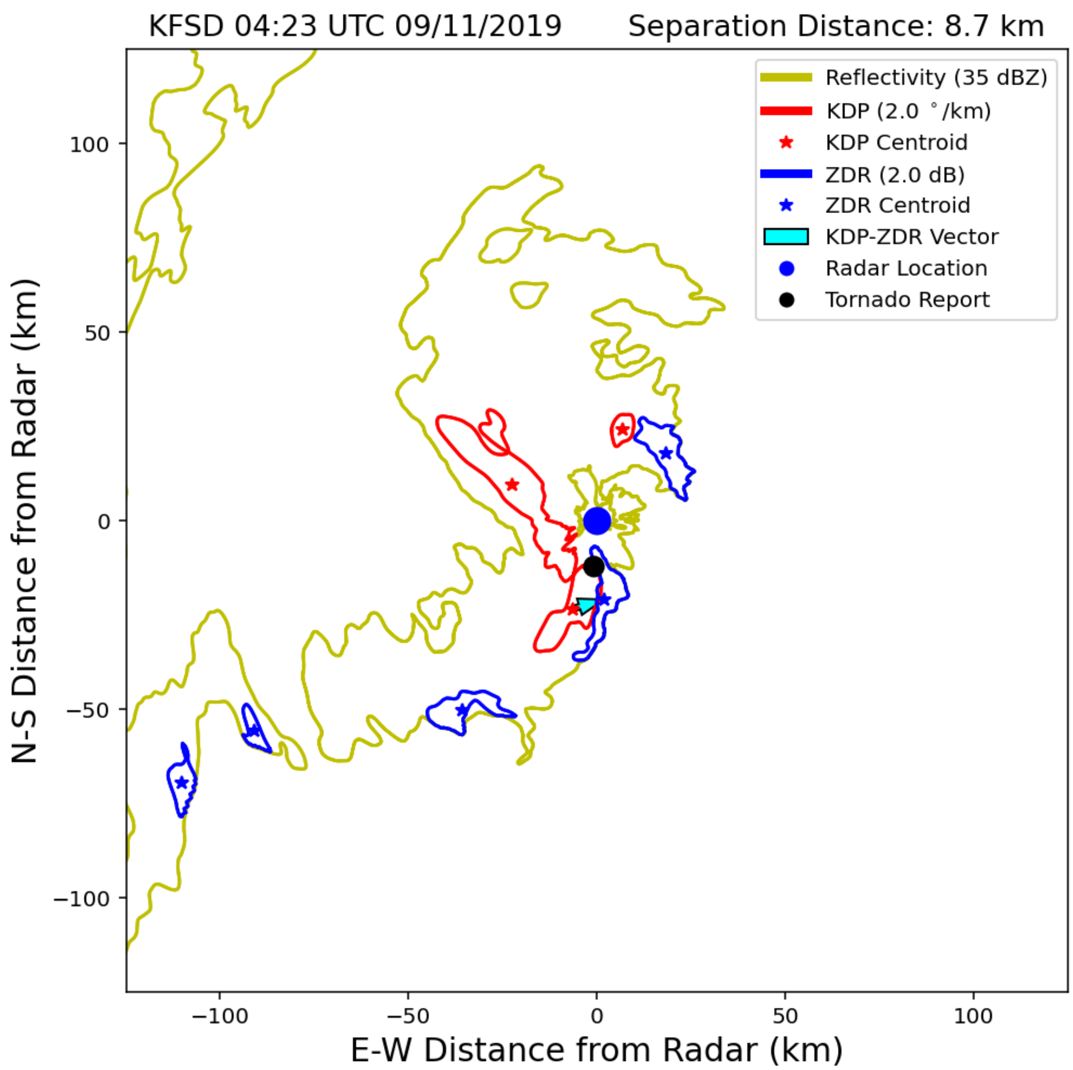

Figure 17. As in Figure 13 but for the KFSD radar at 4:23z on 9/11/2019, for Z_{DR} and K_{DP} contours of 2.0 dB and 2.0 deg/km respectively, and a K_{DP}/Z_{DR} separation vector magnitude of 8.7 km

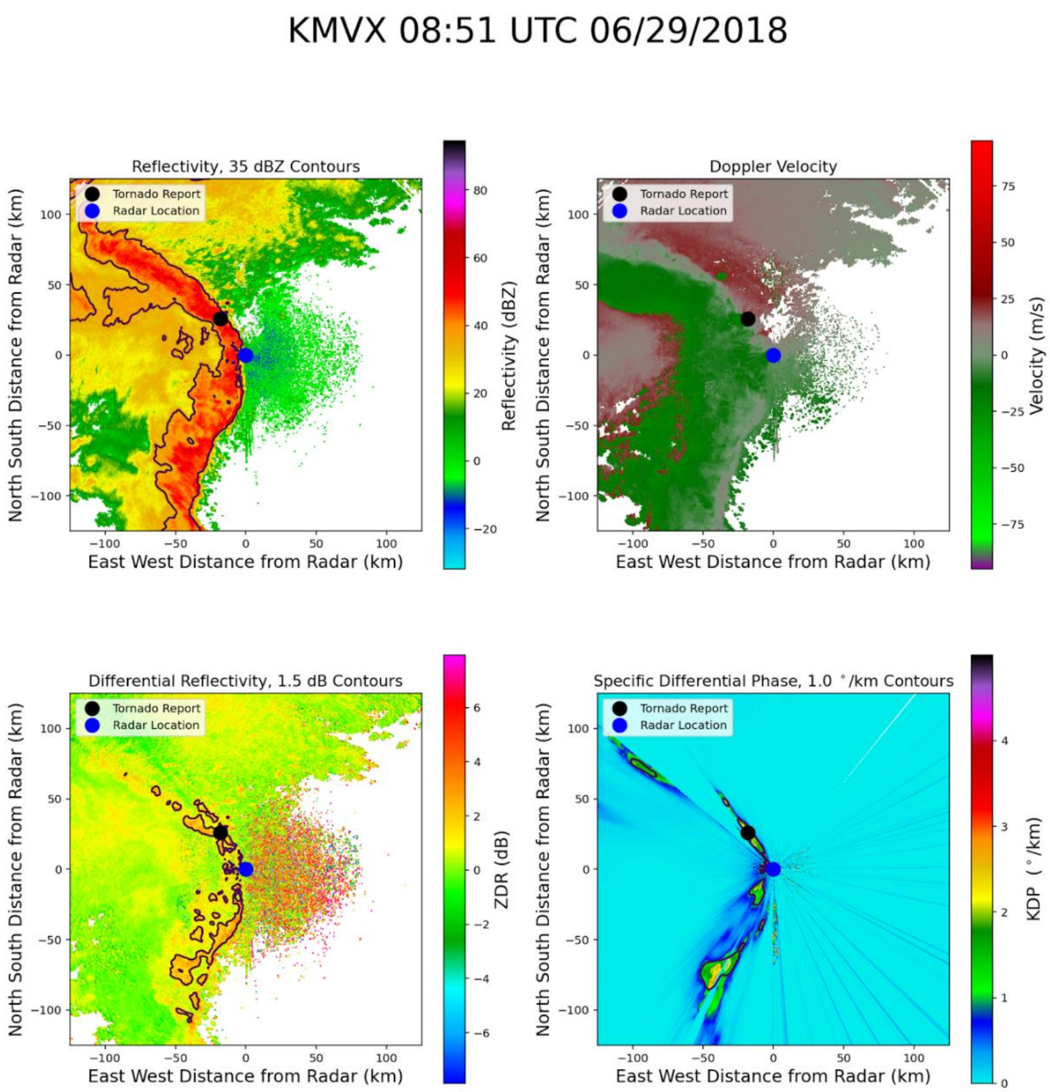

Figure 18. As in Figure 12, but for the KMVX radar at 8:51z on 06/29/2018 and for Z_{DR} and K_{DP} contours of 1.5 dB and 1.0 deg/km respectively.

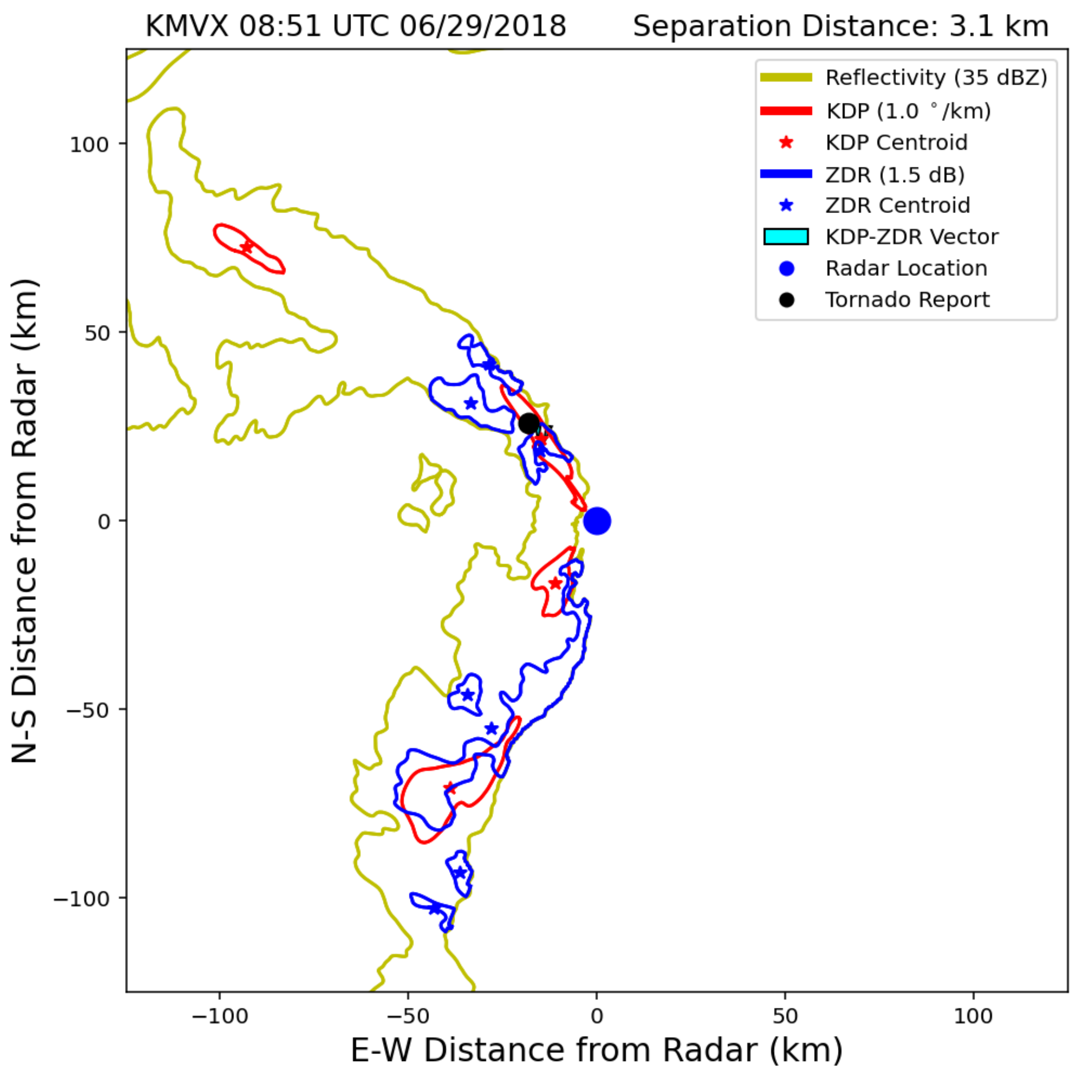

Figure 19. As in Figure 13 but for the KMVX radar at 8:51z on 6/29/2018, for Z_{DR} and K_{DP} contours of 1.5 dB and 1.0 deg/km respectively, and a K_{DP}/Z_{DR} separation vector magnitude of 3.1 km

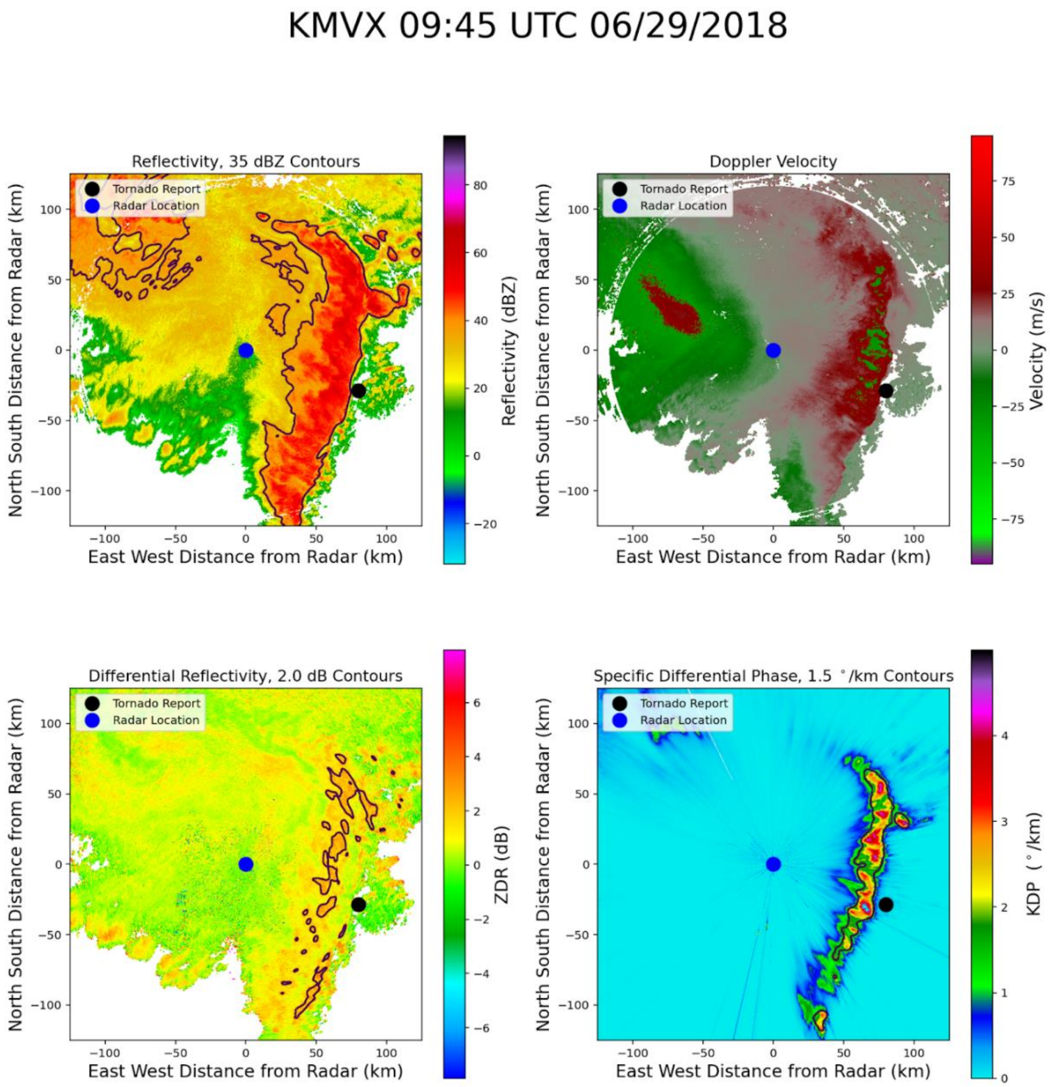

Figure 20. As in Figure 12, but for the KMVX radar at 9:45z on 06/29/2018 and for Z_{DR} and K_{DP} contours of 2.0 dB and 1.5 deg/km respectively.

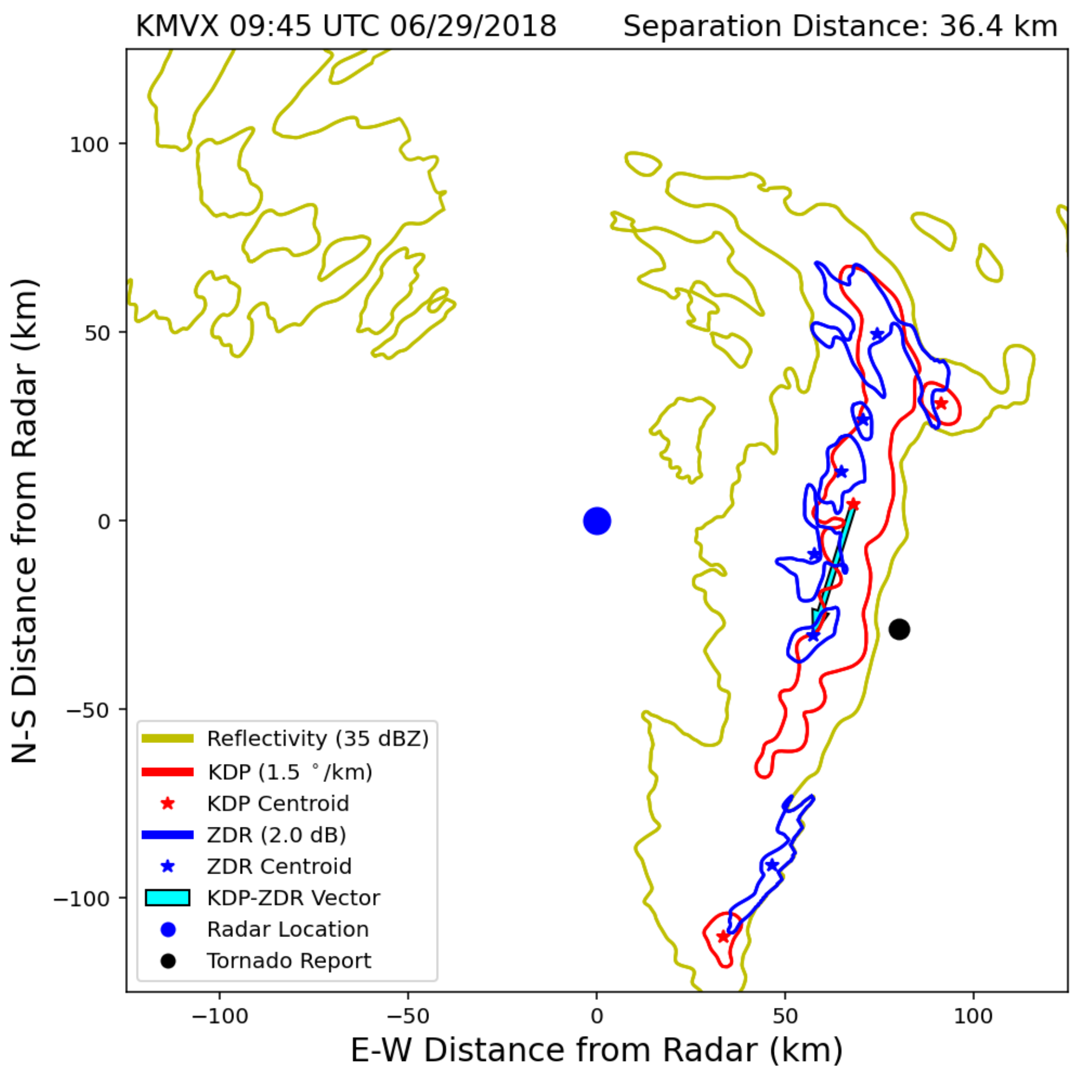

Figure 21. As in Figure 13 but for the KMVX radar at 9:45z on 6/29/2018, for Z_{DR} and K_{DP} contours of 2.0 dB and 1.5 deg/km respectively, and a K_{DP}/Z_{DR} separation vector magnitude of 36.4 km

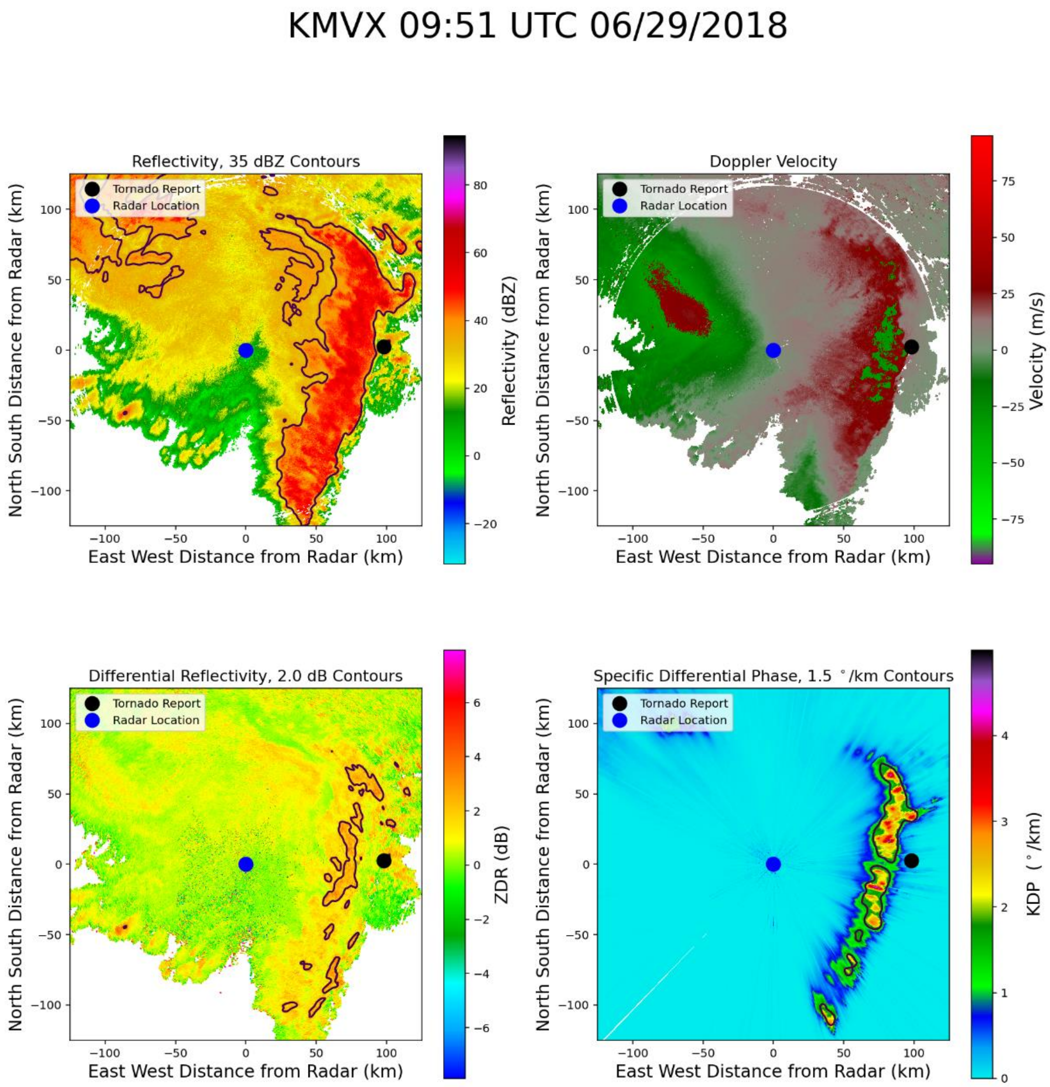

Figure 22. As in Figure 12, but for the KMVX radar at 9:51z on 06/29/2018 and for Z_{DR} and K_{DP} contours of 2.0 dB and 1.5 deg/km respectively.

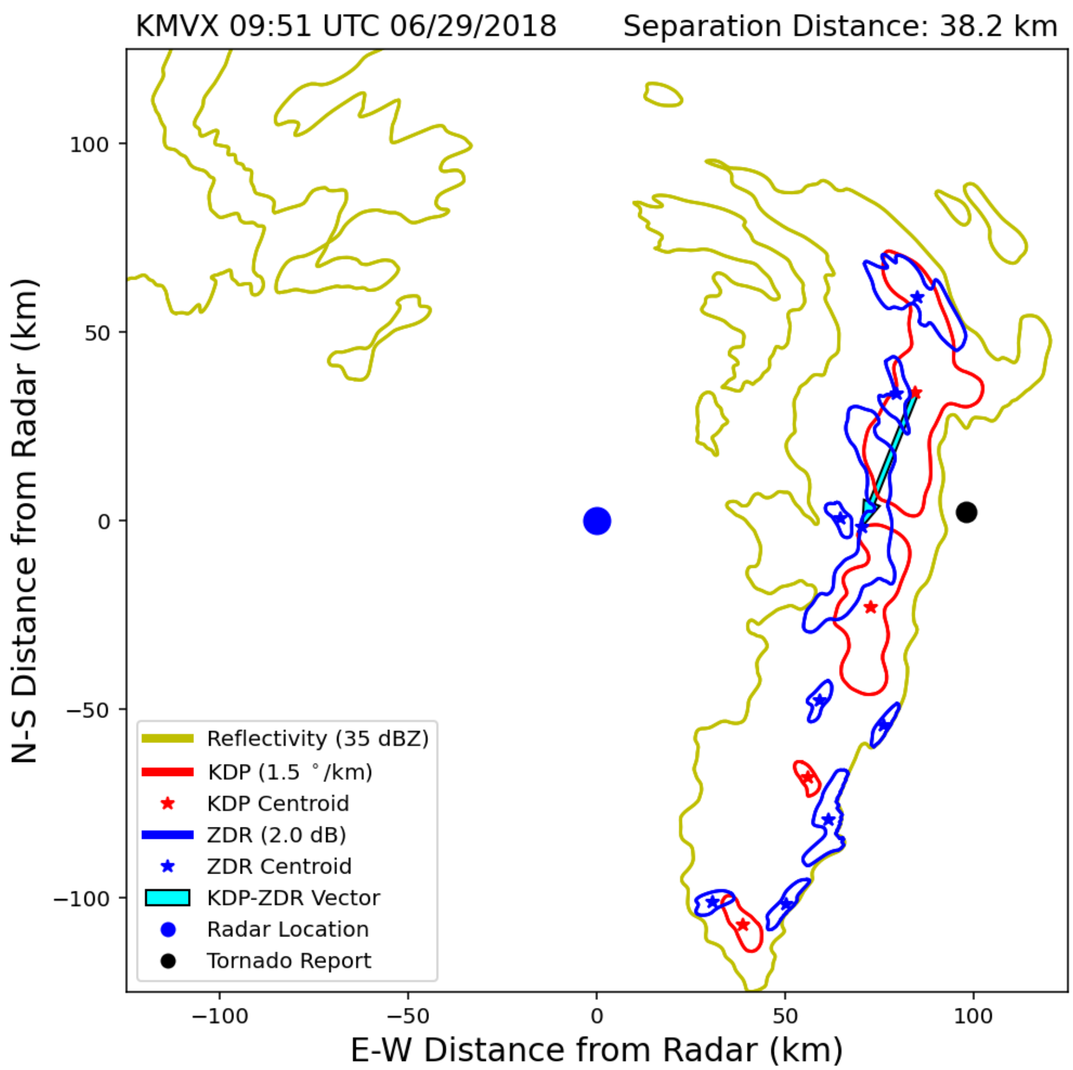

Figure 23. As in Figure 13 but for the KMVX radar at 9:51z on 6/29/2018, for Z_{DR} and K_{DP} contours of 2.0 dB and 1.5 deg/km respectively, and a K_{DP}/Z_{DR} separation vector magnitude of 38.2 km

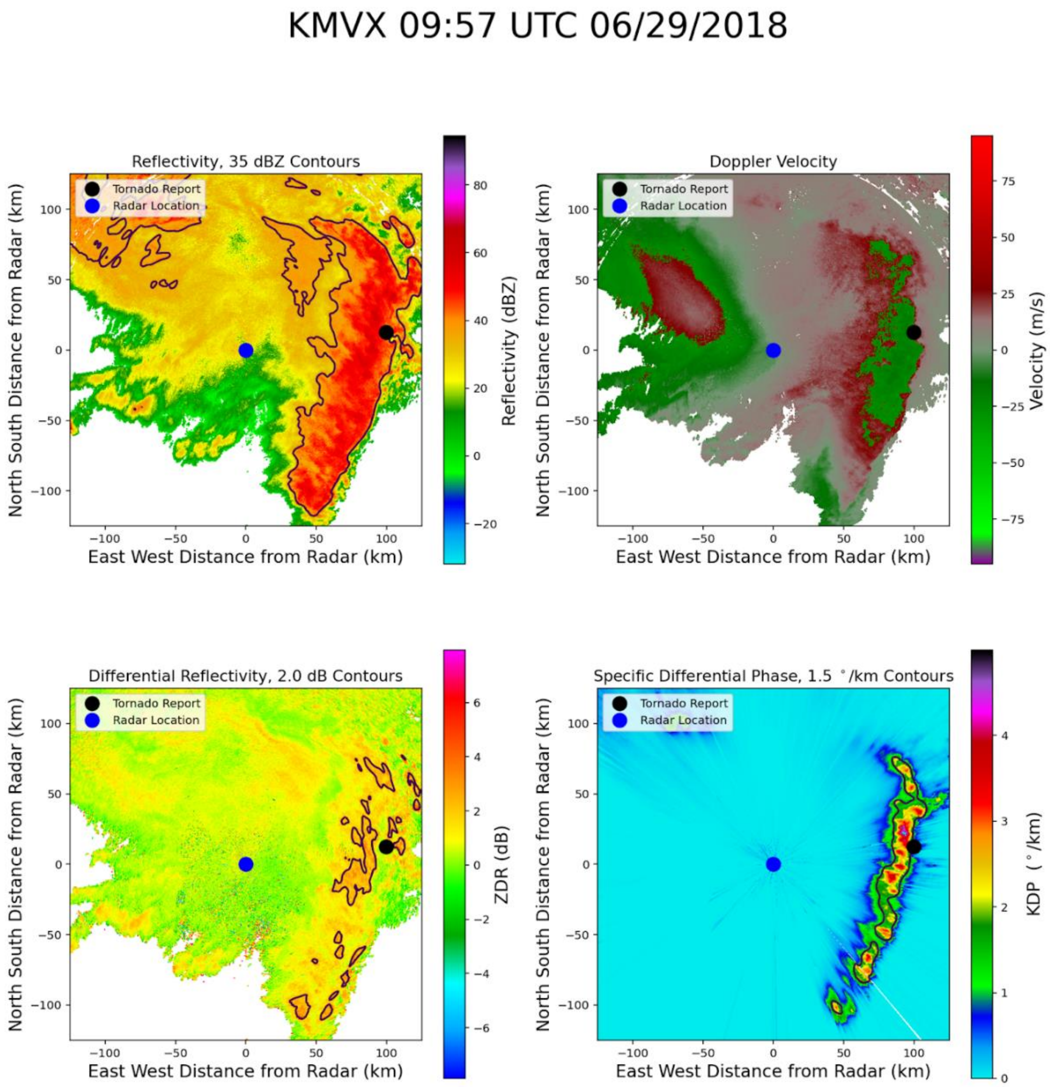

Figure 24. As in Figure 12, but for the KMVX radar at 9:57z on 06/29/2018 and for Z_{DR} and K_{DP} contours of 2.0 dB and 1.5 deg/km respectively.

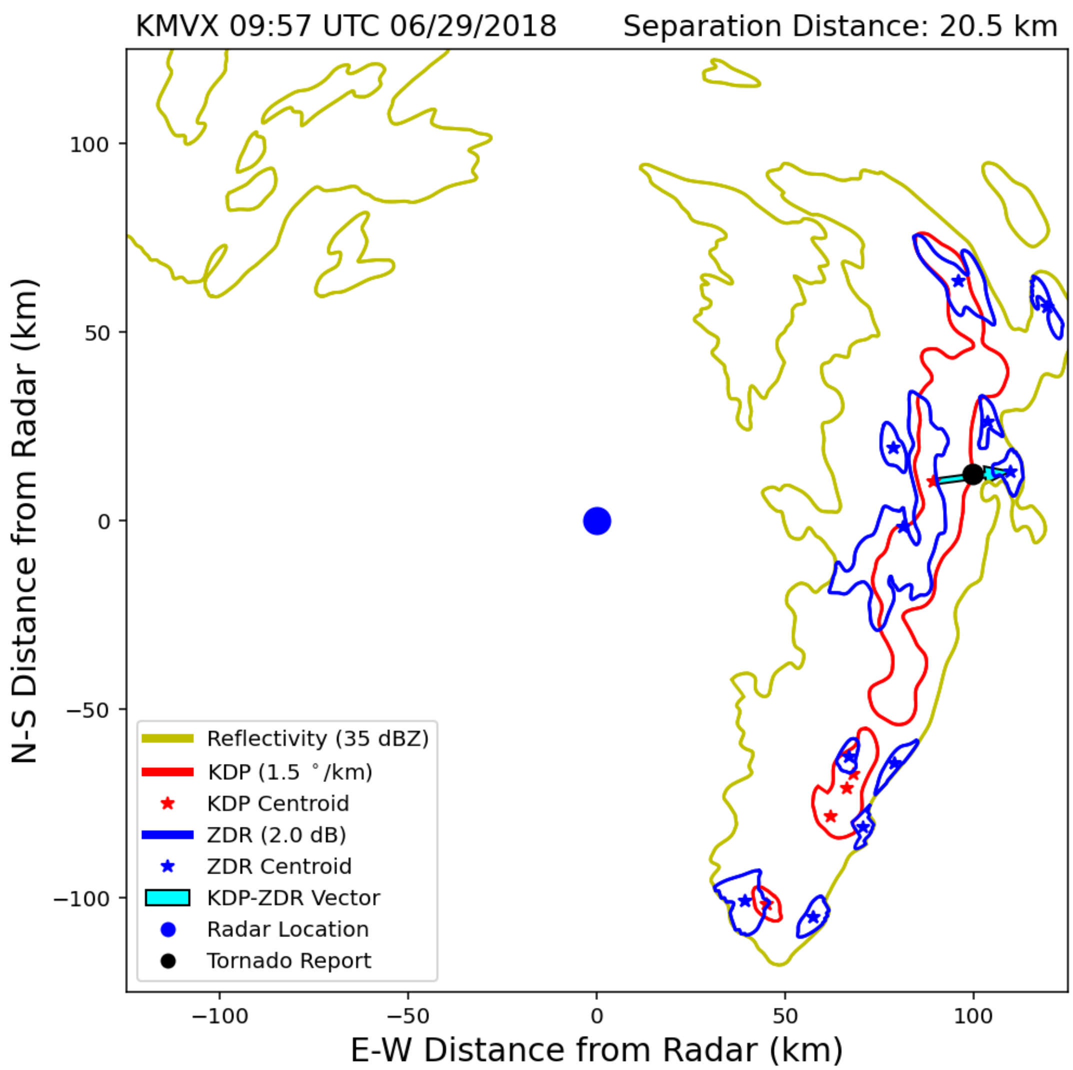

Figure 25. As in Figure 13 but for the KMVX radar at 9:57z on 6/29/2018, for Z_{DR} and K_{DP} contours of 2.0 dB and 1.5 deg/km respectively, and a K_{DP}/Z_{DR} separation vector magnitude of 20.5 km

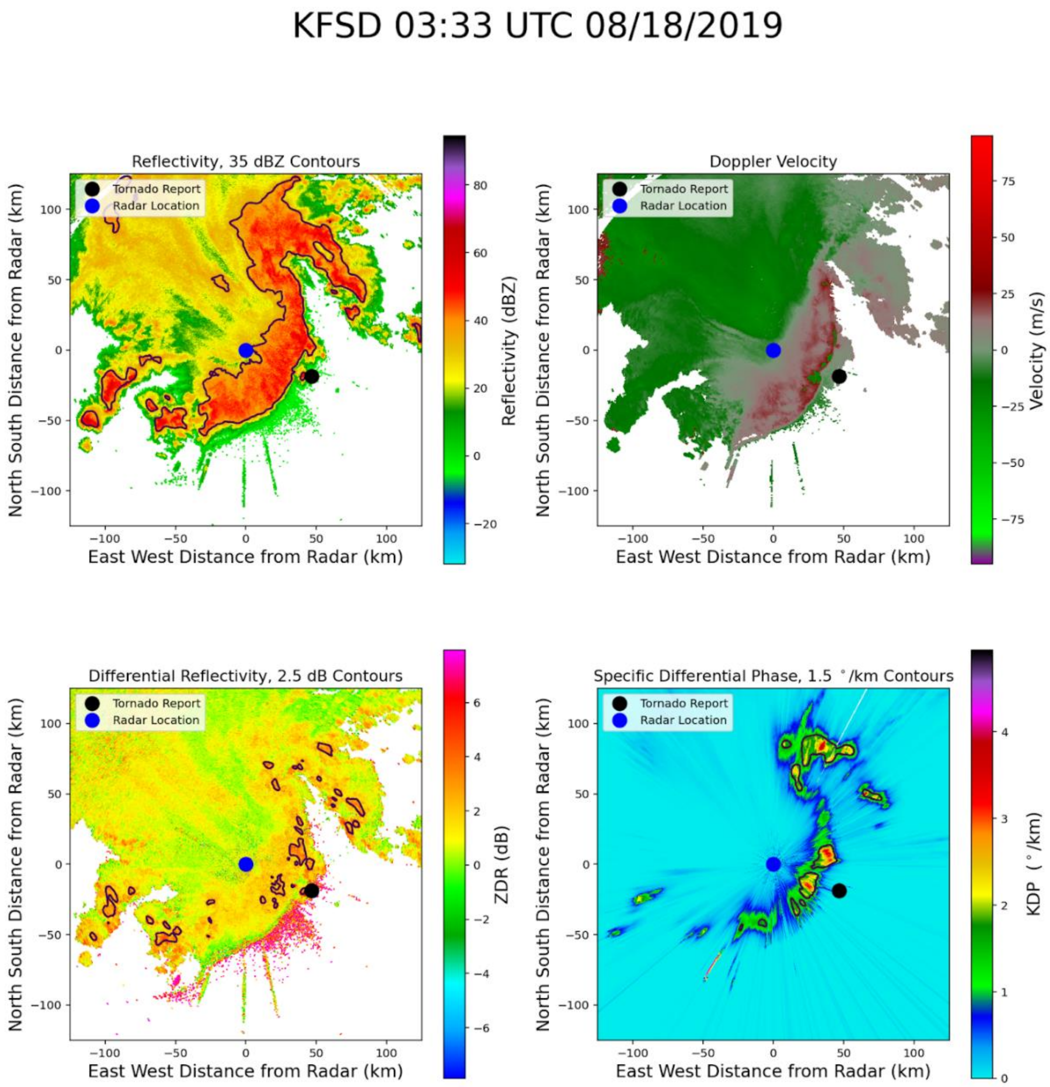

Figure 26. As in Figure 12, but for the KFSD radar at 3:33z on 08/18/2019 and for Z_{DR} and K_{DP} contours of 2.5 dB and 1.5 deg/km respectively.

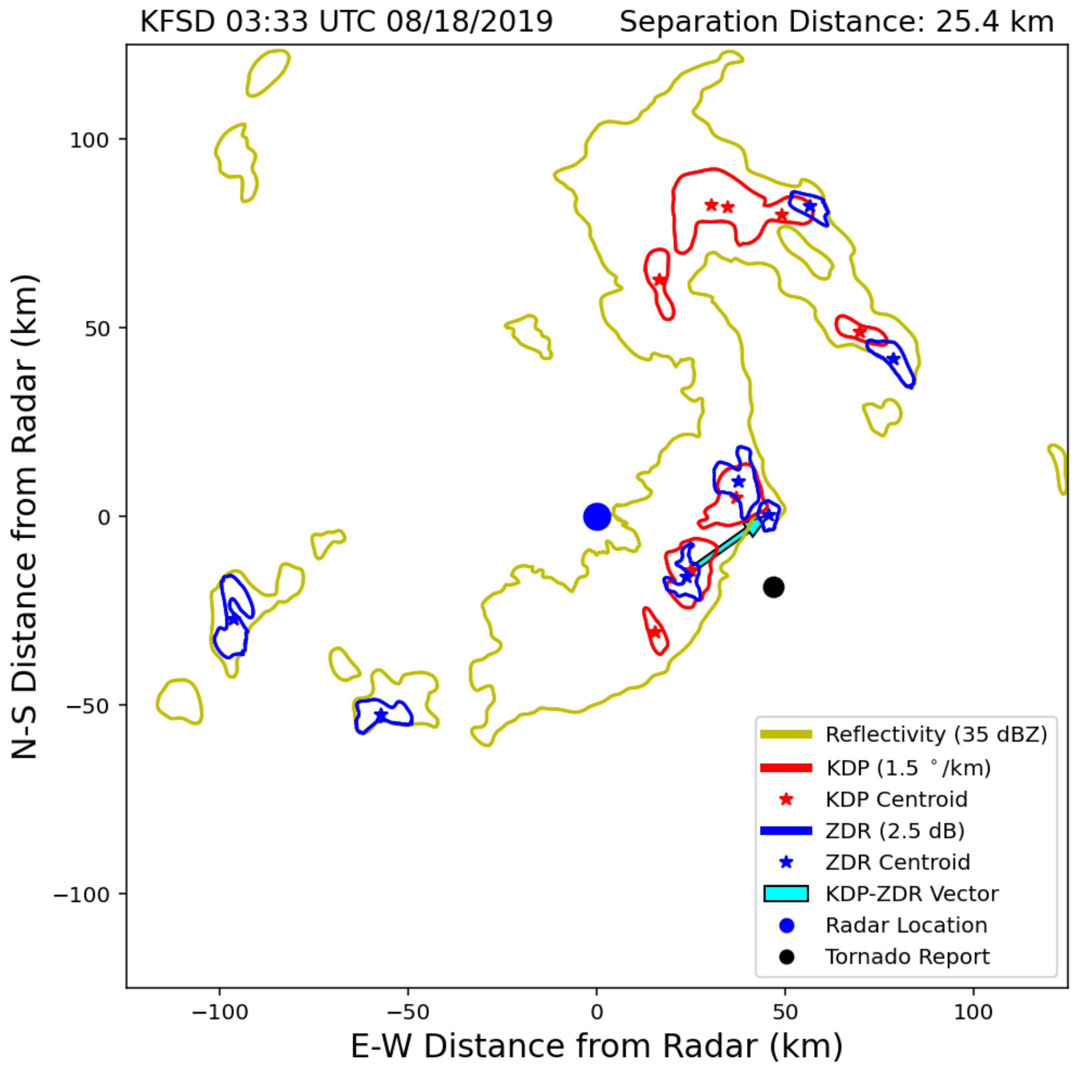

Figure 27. As in Figure 13 but for the KFSD radar at 3:33z on 8/18/2019, for Z_{DR} and K_{DP} contours of 2.5 dB and 1.5 deg/km respectively, and a K_{DP}/Z_{DR} separation vector magnitude of 25.4 km

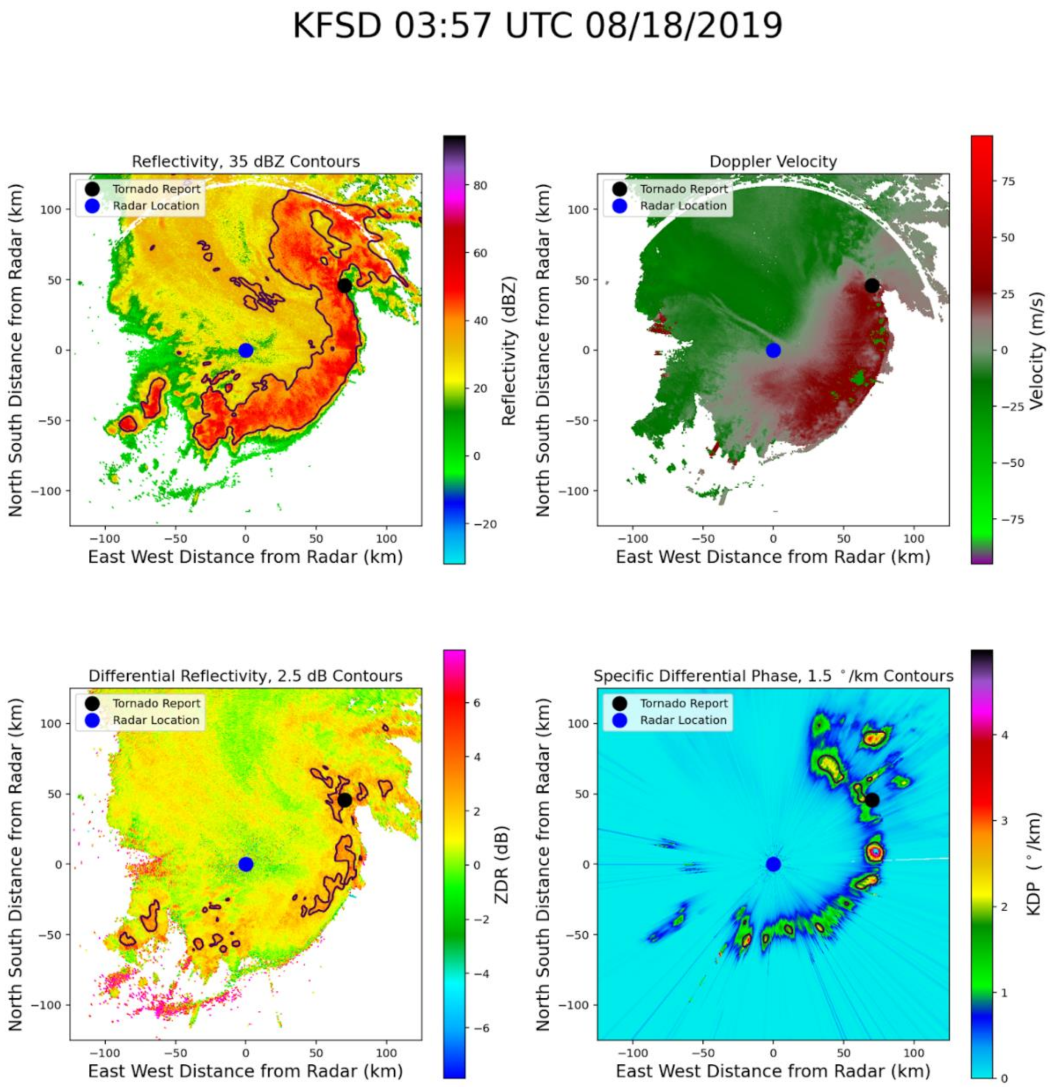

Figure 28. As in Figure 12, but for the KFSD radar at 3:57z on 08/18/2019 and for Z_{DR} and K_{DP} contours of 2.5 dB and 1.5 deg/km respectively.

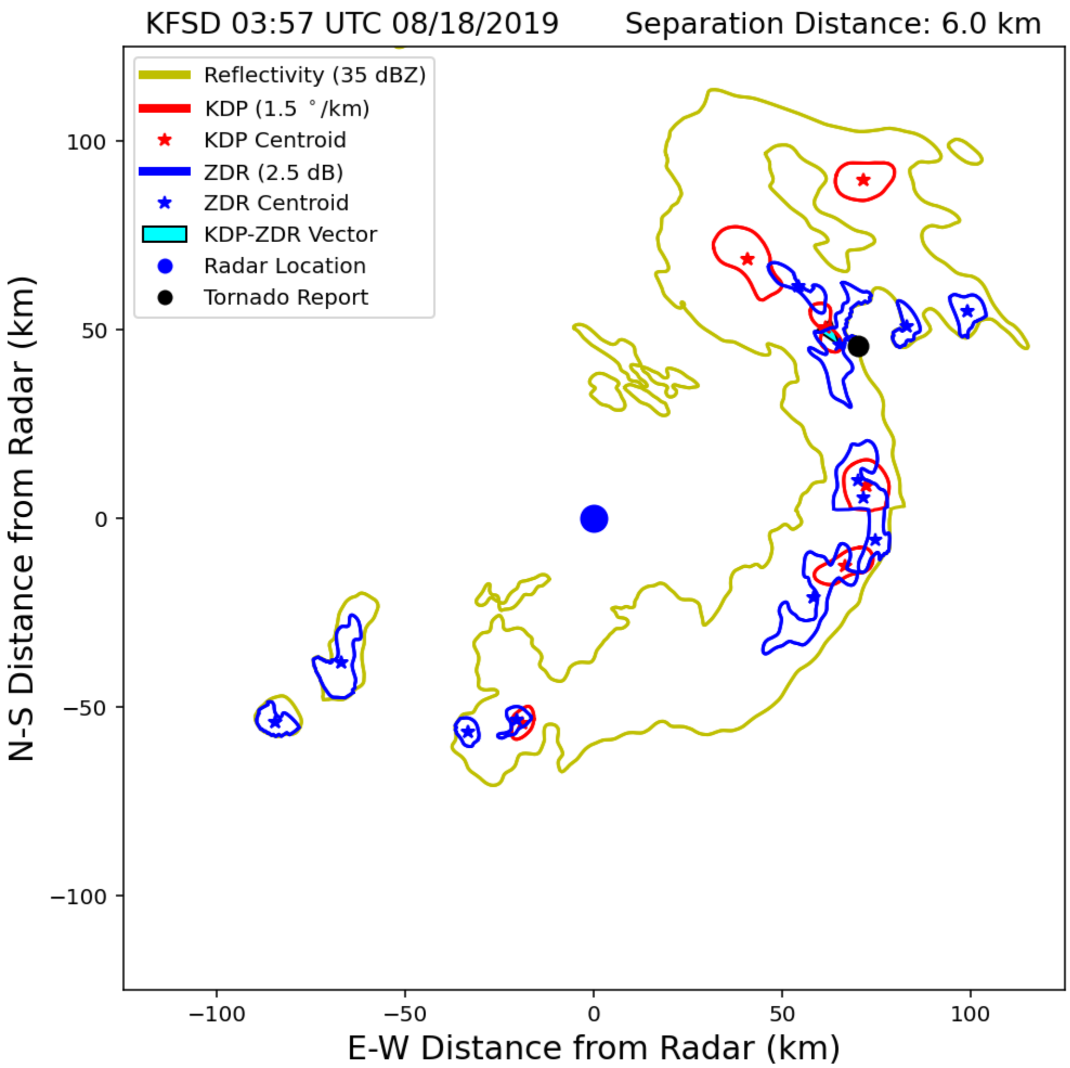

Figure 29. As in Figure 13 but for the KFSD radar at 3:57z on 8/18/2019, for Z_{DR} and K_{DP} contours of 2.5 dB and 1.5 deg/km respectively, and a K_{DP}/Z_{DR} separation vector magnitude of 6.0 km.

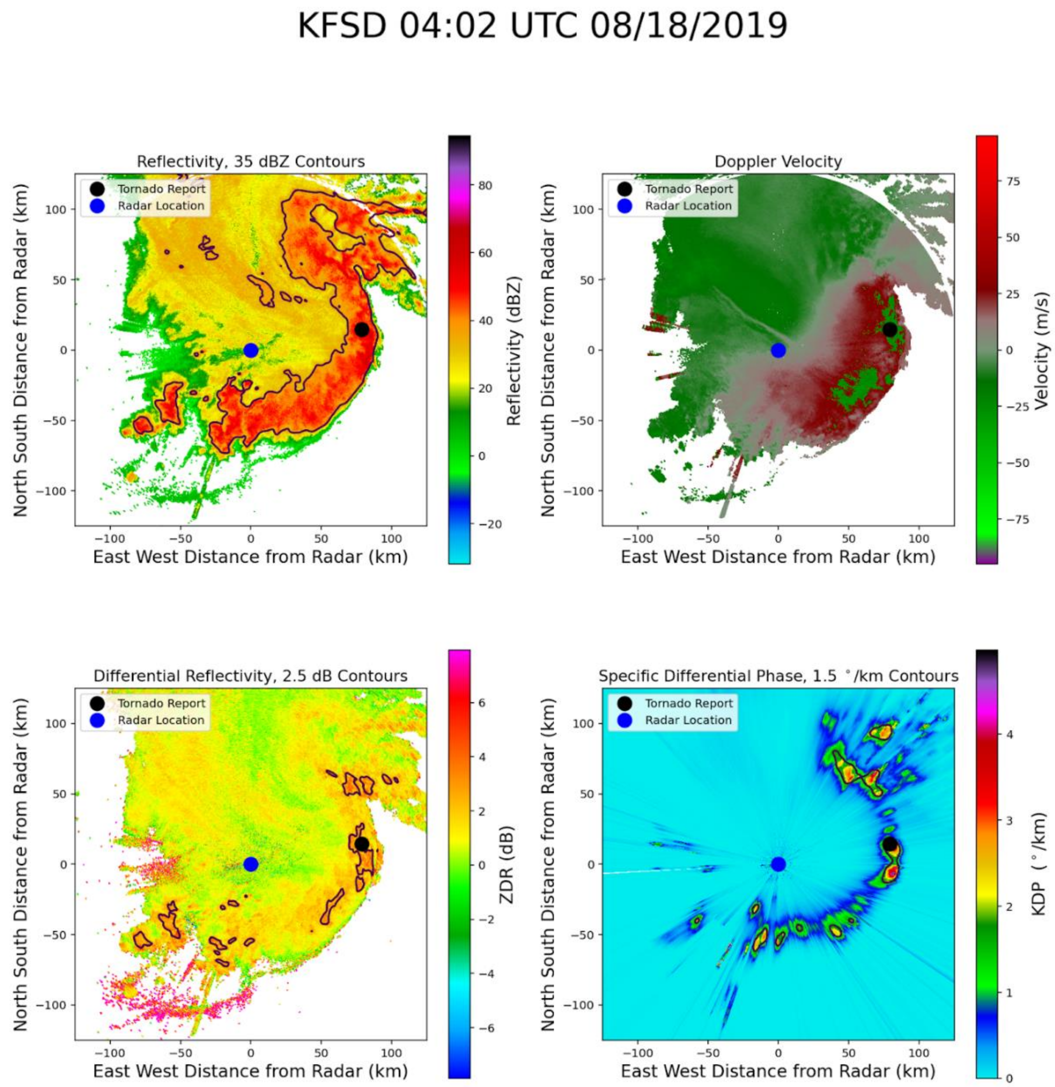

Figure 30. As in Figure 12, but for the KFSD radar at 4:02z on 08/18/2019 and for Z_{DR} and K_{DP} contours of 2.5 dB and 1.5 deg/km respectively.

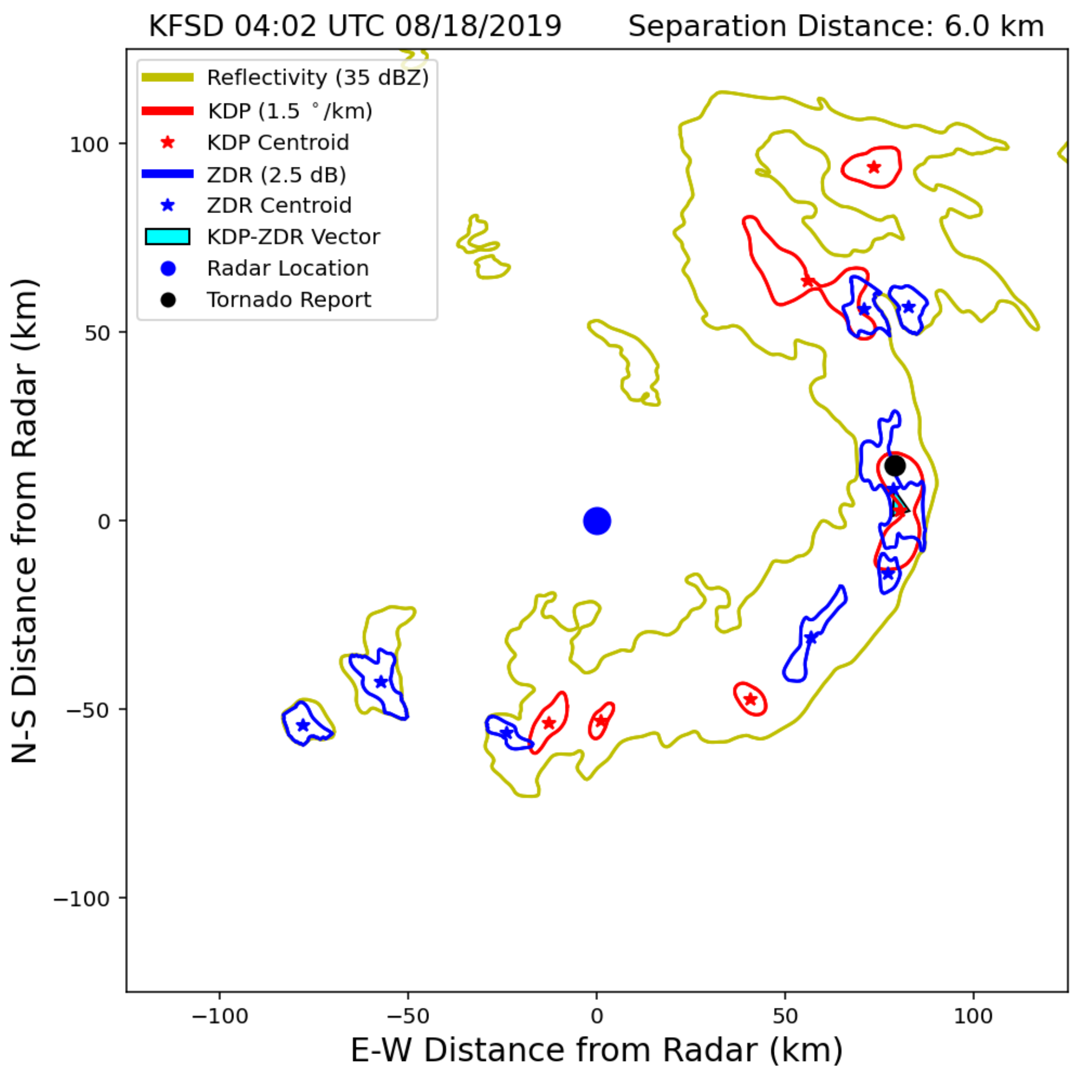

Figure 31. As in Figure 13 but for the KFSD radar at 4:02z on 8/18/2019, for Z_{DR} and K_{DP} contours of 2.5 dB and 1.5 deg/km respectively, and a K_{DP}/Z_{DR} separation vector magnitude of 6.0 km

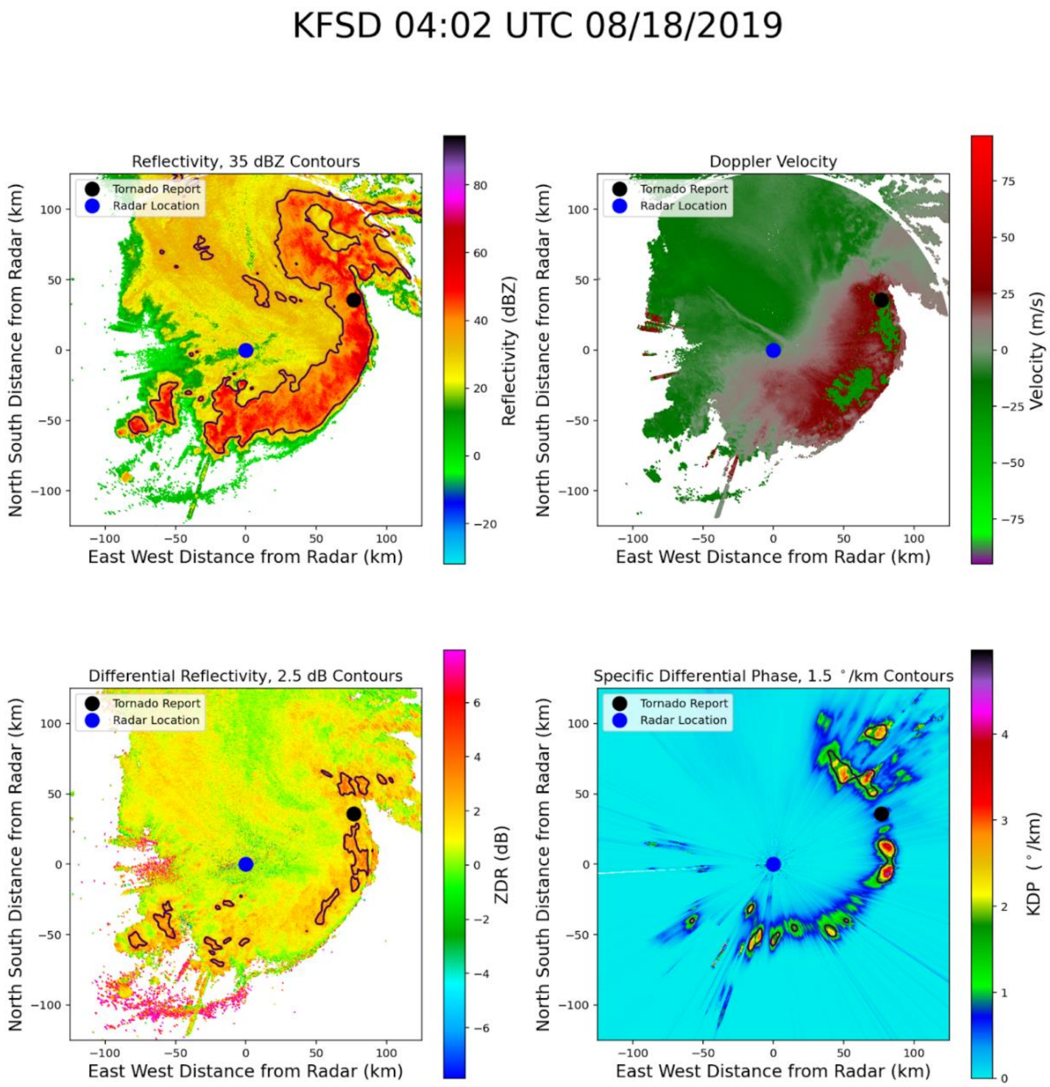

Figure 32. As in Figure 30, but for a different tornado reported at the same time

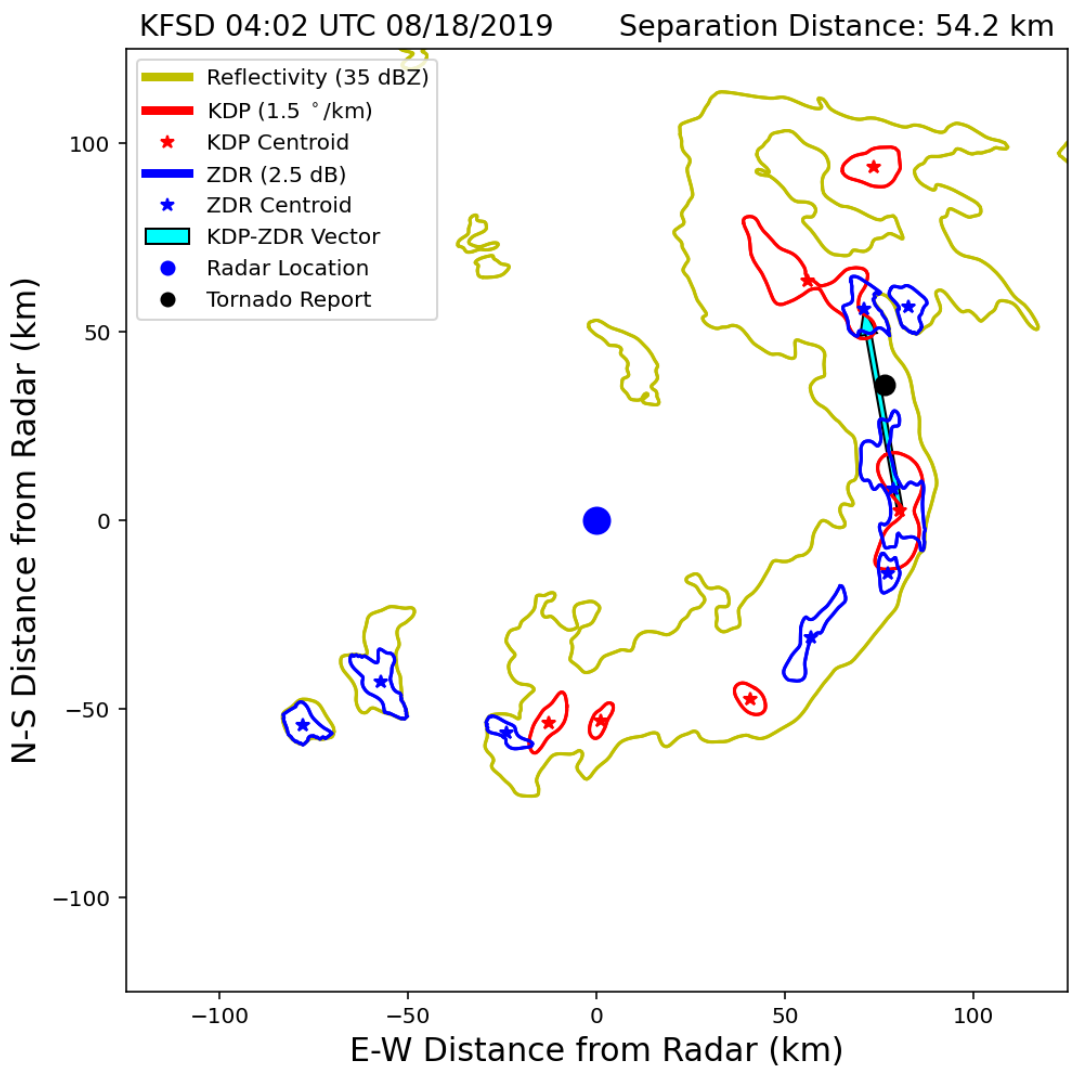

Figure 33. As in Figure 31, but for a different tornado reported at the same time and a K_{DP}/Z_{DR} separation distance of 54.2 km.

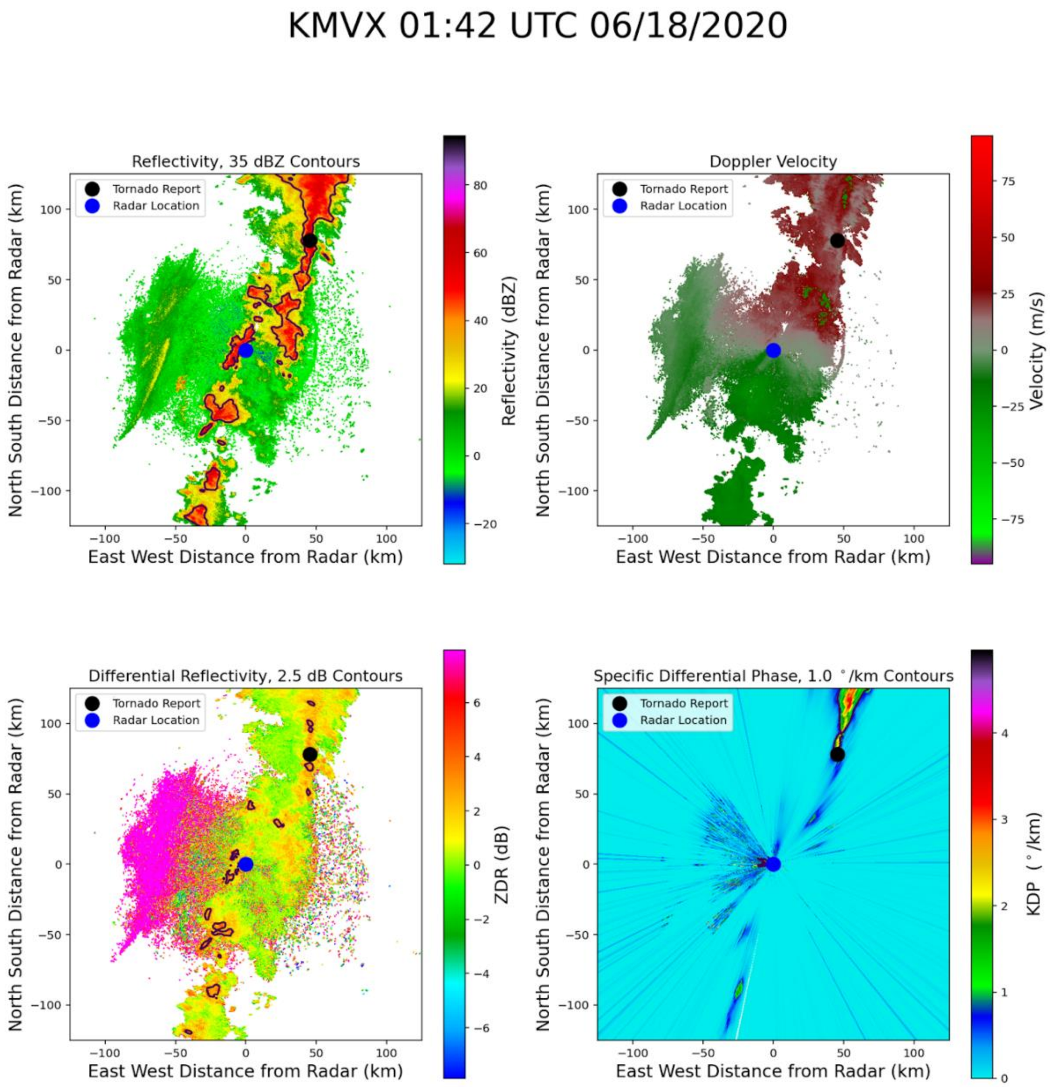

Figure 34. As in Figure 12, but for the KMVX radar at 1:42z on 06/18/2020 and for Z_{DR} and K_{DP} contours of 2.5 dB and 1.0 deg/km respectively.

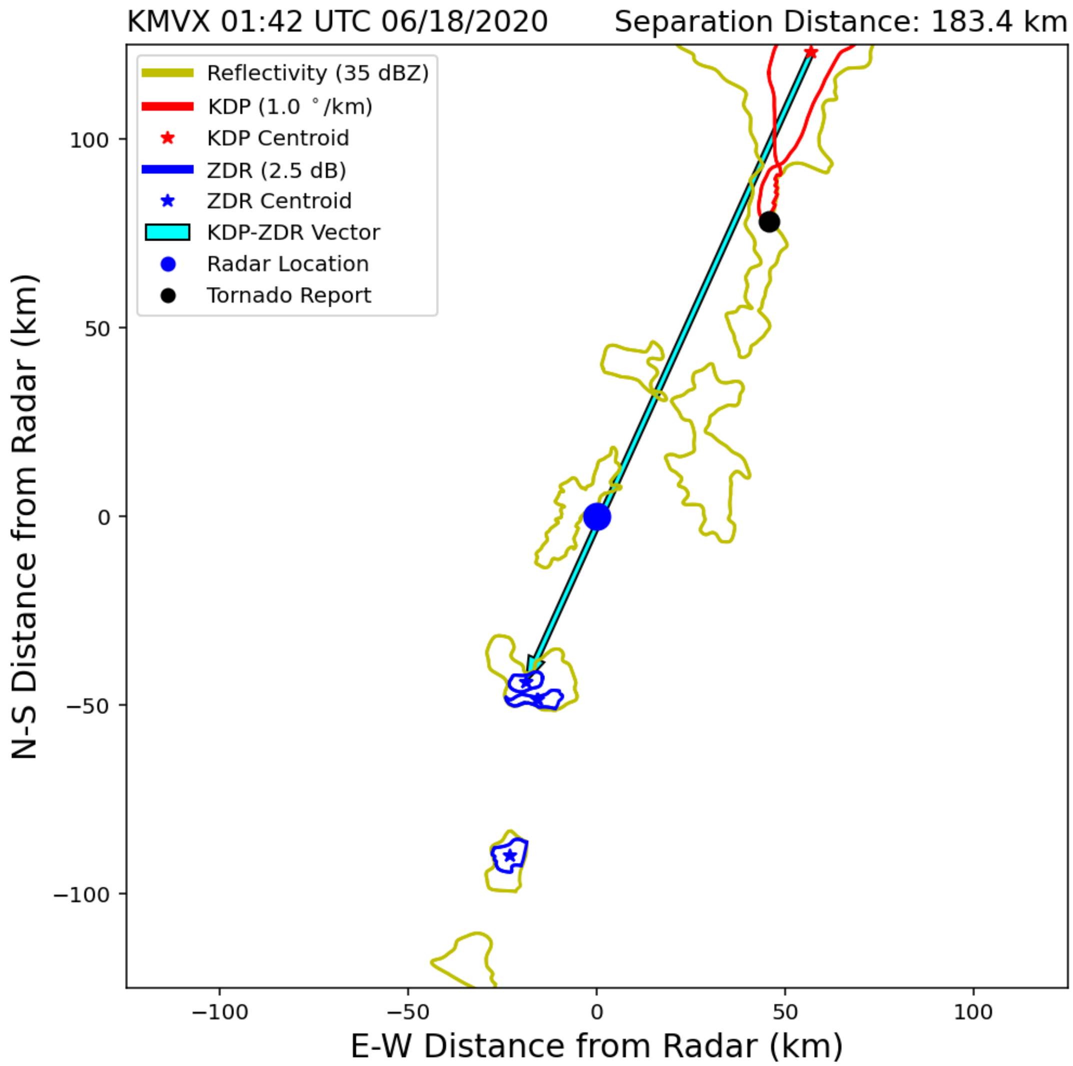

Figure 35. As in Figure 13 but for the KMVX radar at 1:42z on 6/18/2020, for Z_{DR} and K_{DP} contours of 2.5 dB and 1.0 deg/km respectively, and a K_{DP}/Z_{DR} separation vector magnitude of 183.4 km. This particular case was assigned a separation vector magnitude of 0 in the sample as the Z_{DR} centroid was more than 30 km from the tornado report.

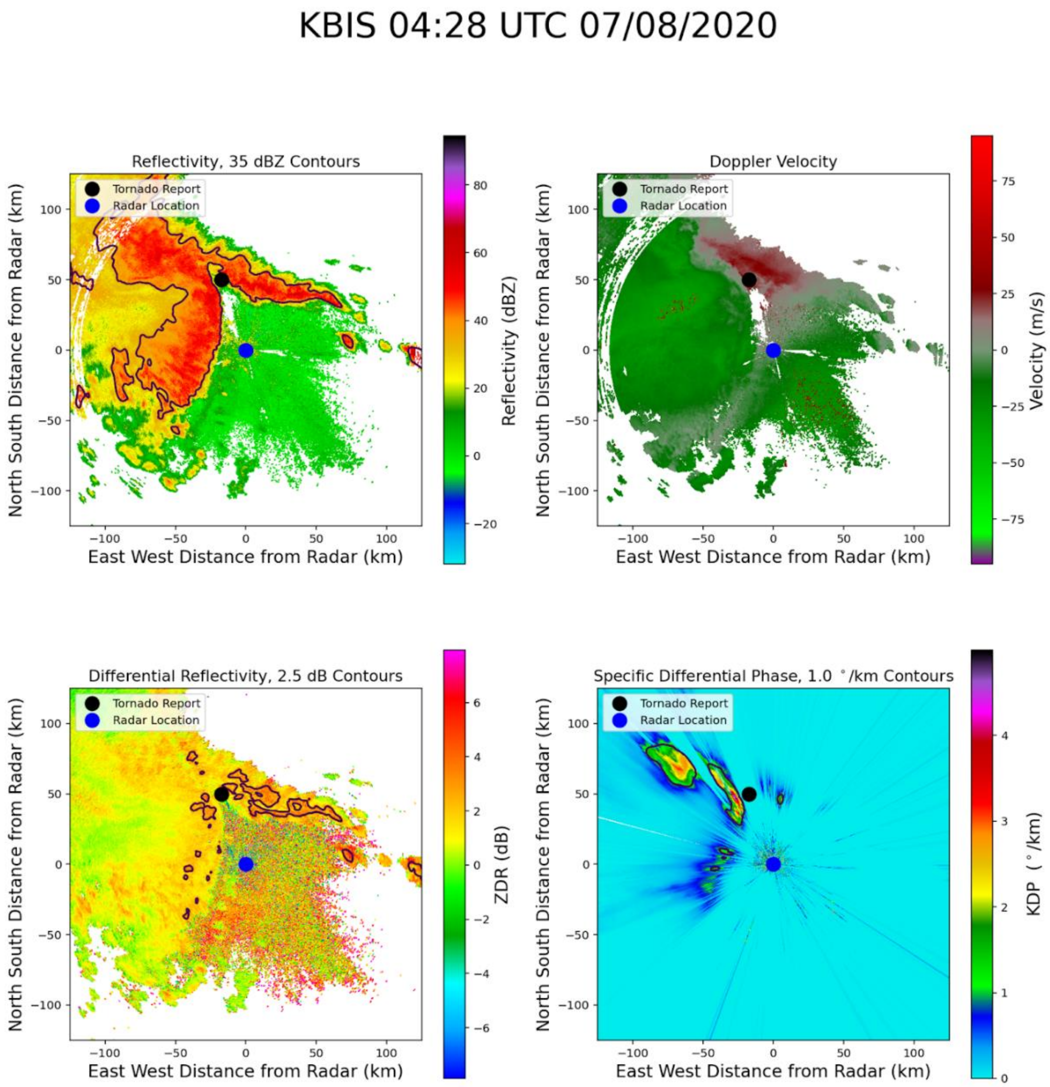

Figure 36. As in Figure 12, but for the KBIS radar at 4:28z on 7/8/2020 and for Z_{DR} and K_{DP} contours of 2.5 dB and 1.0 deg/km respectively.

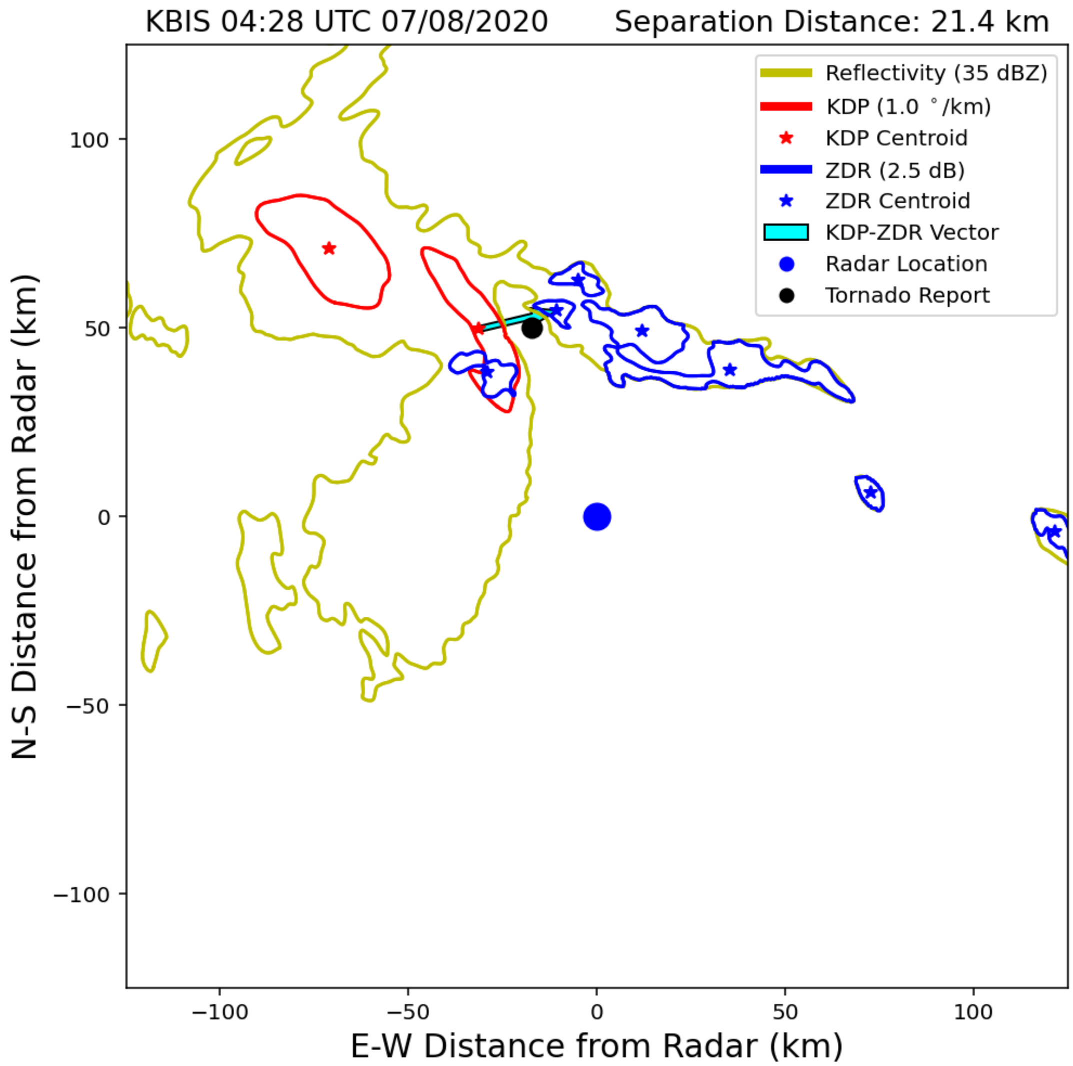

Figure 37. As in Figure 13 but for the KBIS radar at 4:28z on 7/8/2020, for Z_{DR} and K_{DP} contours of 2.5 dB and 1.0 deg/km respectively, and a K_{DP}/Z_{DR} separation vector magnitude of 21.4 km.

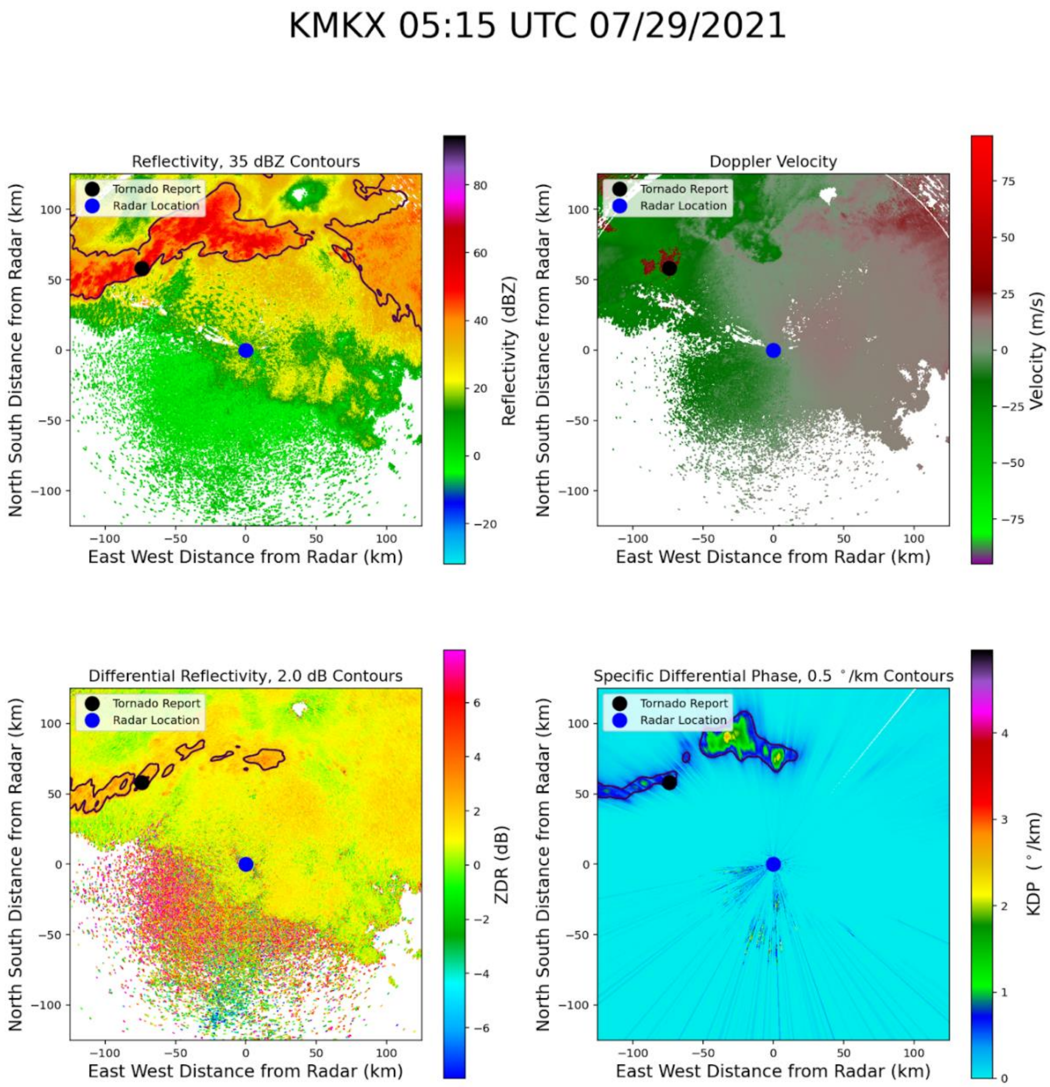

Figure 38. As in Figure 12, but for the KMKX radar at 5:15z on 7/29/2021 and for Z_{DR} and K_{DP} contours of 2.0 dB and 0.5 deg/km respectively.

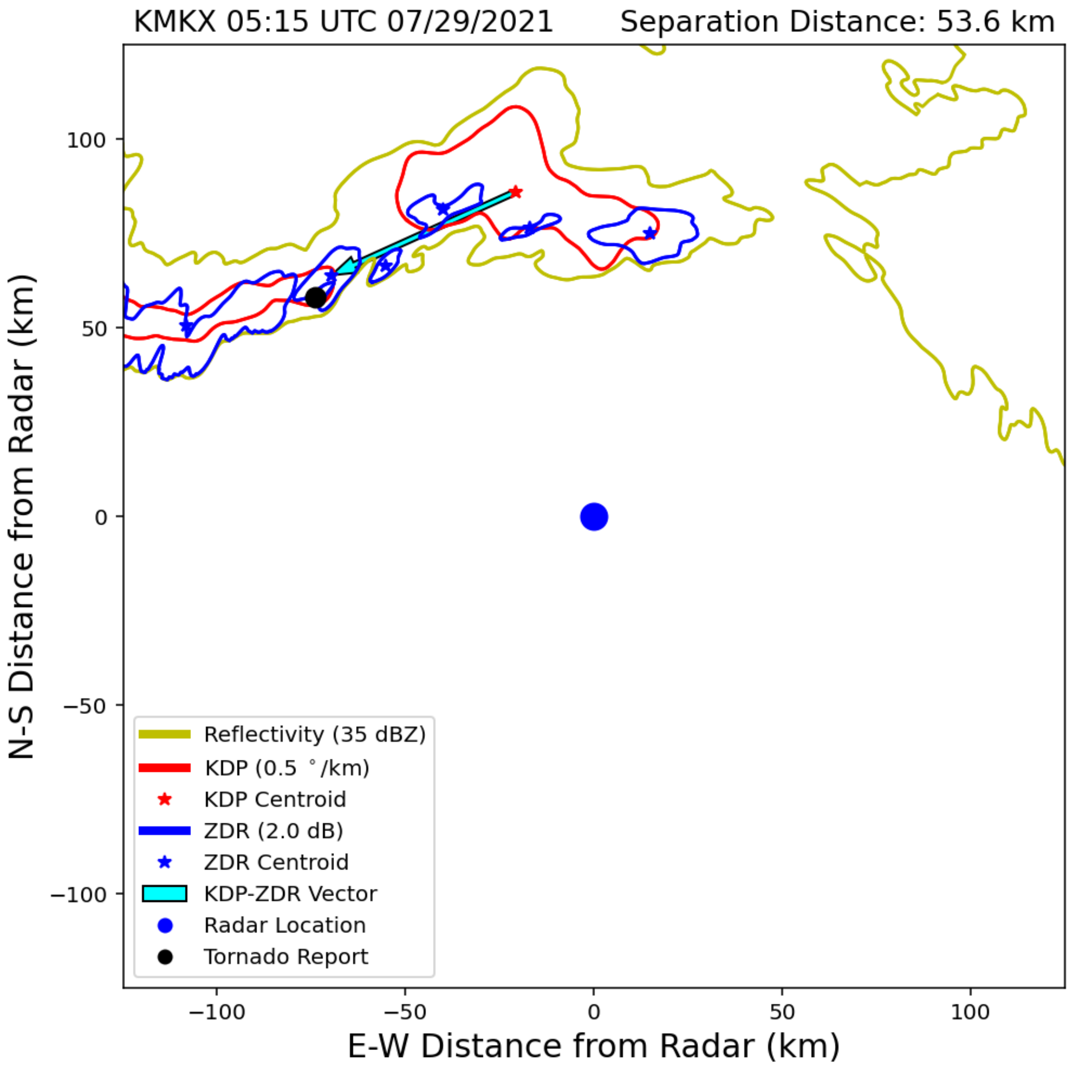

Figure 39. As in Figure 13 but for the KMKX radar at 5:15z on 7/29/2021, for Z_{DR} and K_{DP} contours of 2.0 dB and 0.5 deg/km respectively, and a K_{DP}/Z_{DR} separation vector magnitude of 53.6 km.

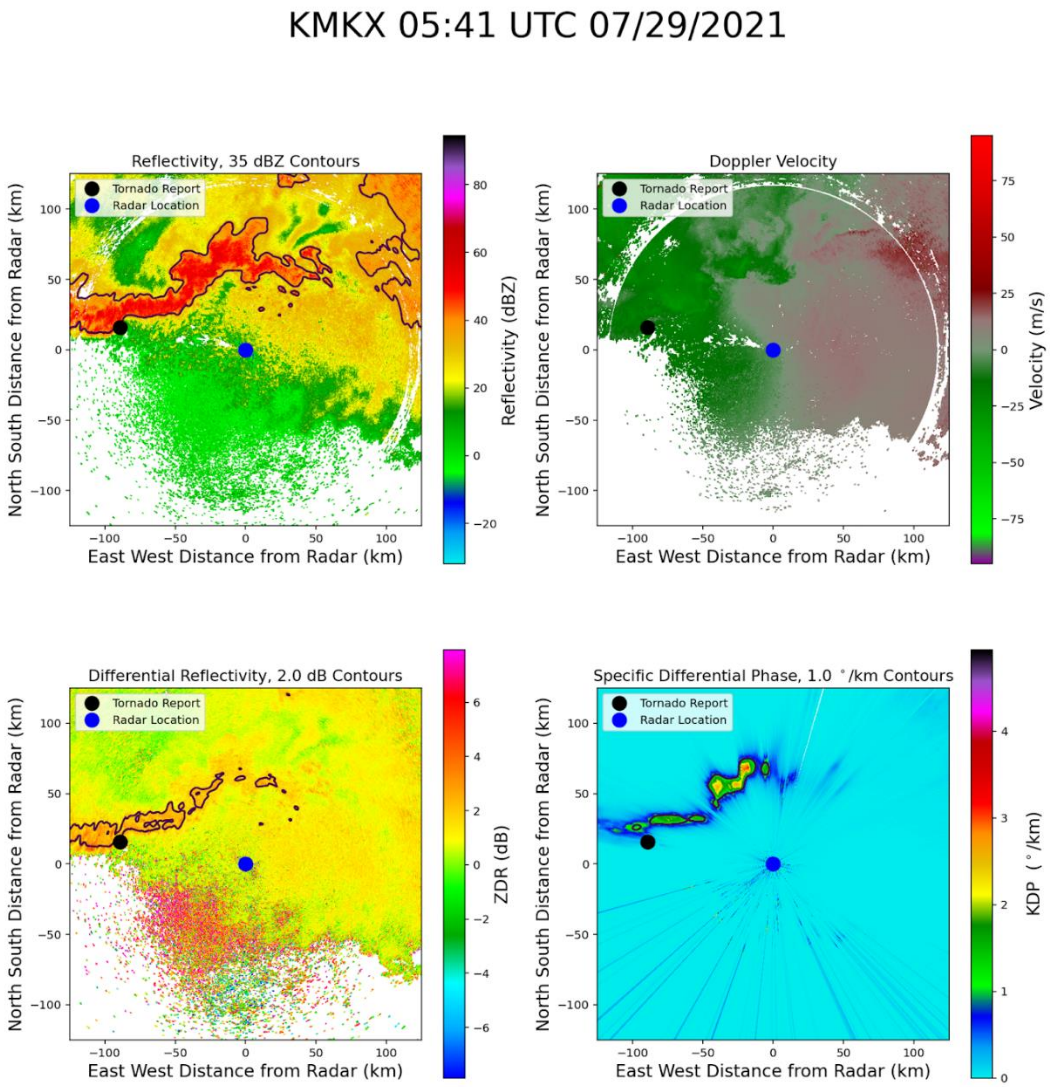

Figure 40. As in Figure 12, but for the KMKX radar at 5:41z on 7/29/2021 and for Z_{DR} and K_{DP} contours of 2.0 dB and 1.0 deg/km respectively.

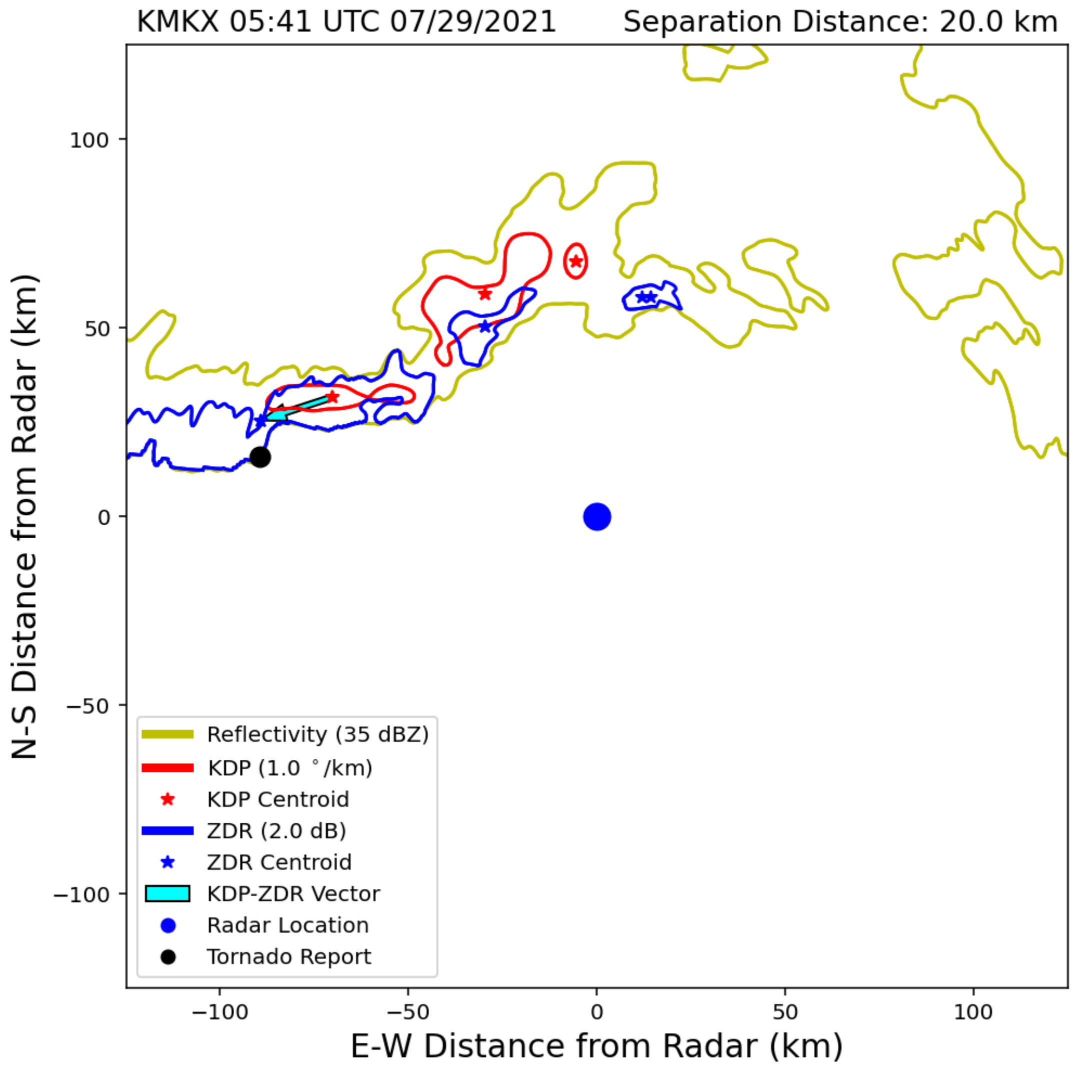

Figure 41. As in Figure 13 but for the KMKX radar at 5:41z on 7/29/2021, for Z_{DR} and K_{DP} contours of 2.0 dB and 1.0 deg/km respectively, and a K_{DP}/Z_{DR} separation vector magnitude of 20.0 km.

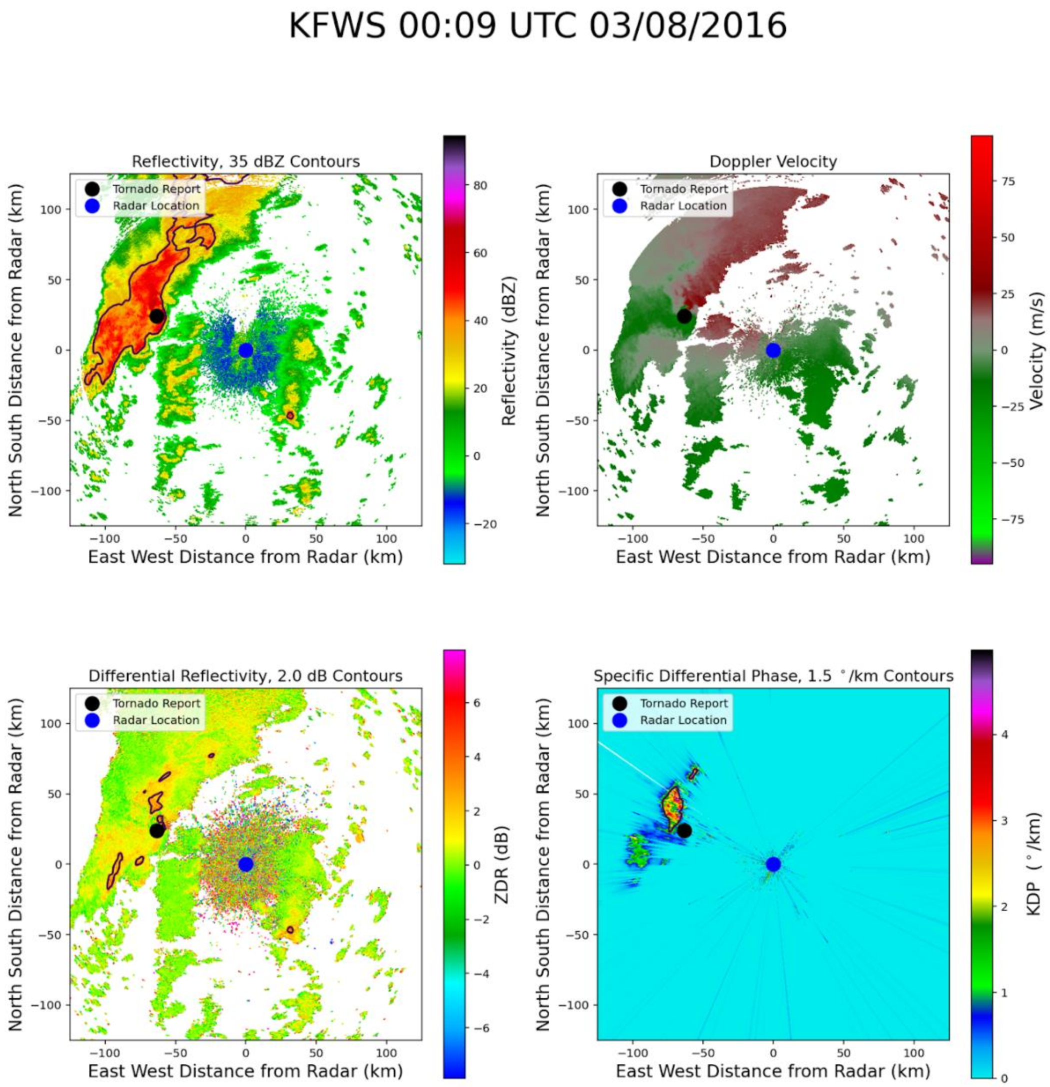

Figure 42. As in Figure 12, but for the KFWS radar at 0:09z on 3/8/2016 and for Z_{DR} and K_{DP} contours of 2.0 dB and 1.5 deg/km respectively.

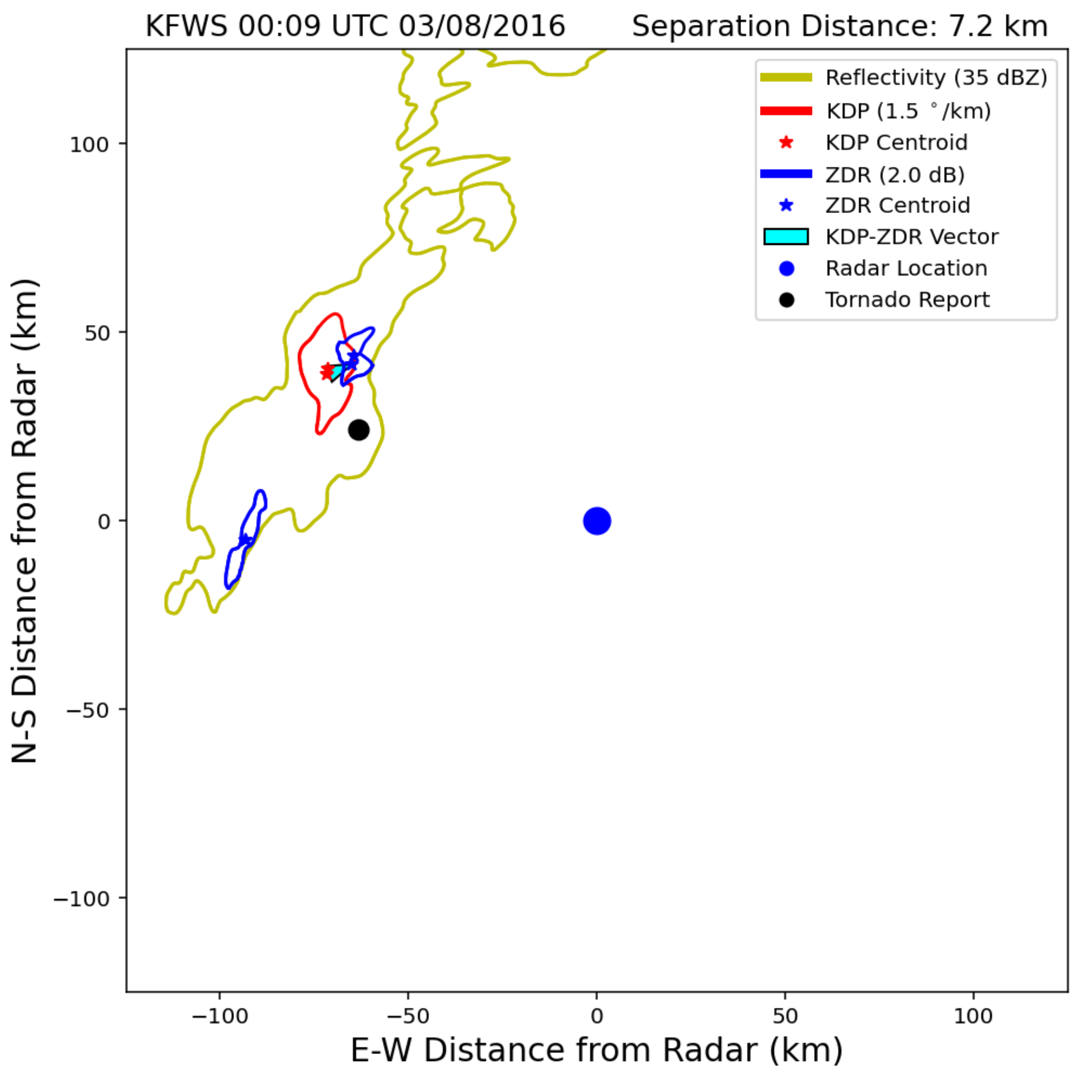

Figure 43. As in Figure 13 but for the KFWS radar at 0:09z on 3/8/2016, for Z_{DR} and K_{DP} contours of 2.0 dB and 1.5 deg/km respectively, and a K_{DP}/Z_{DR} separation vector magnitude of 7.2 km.

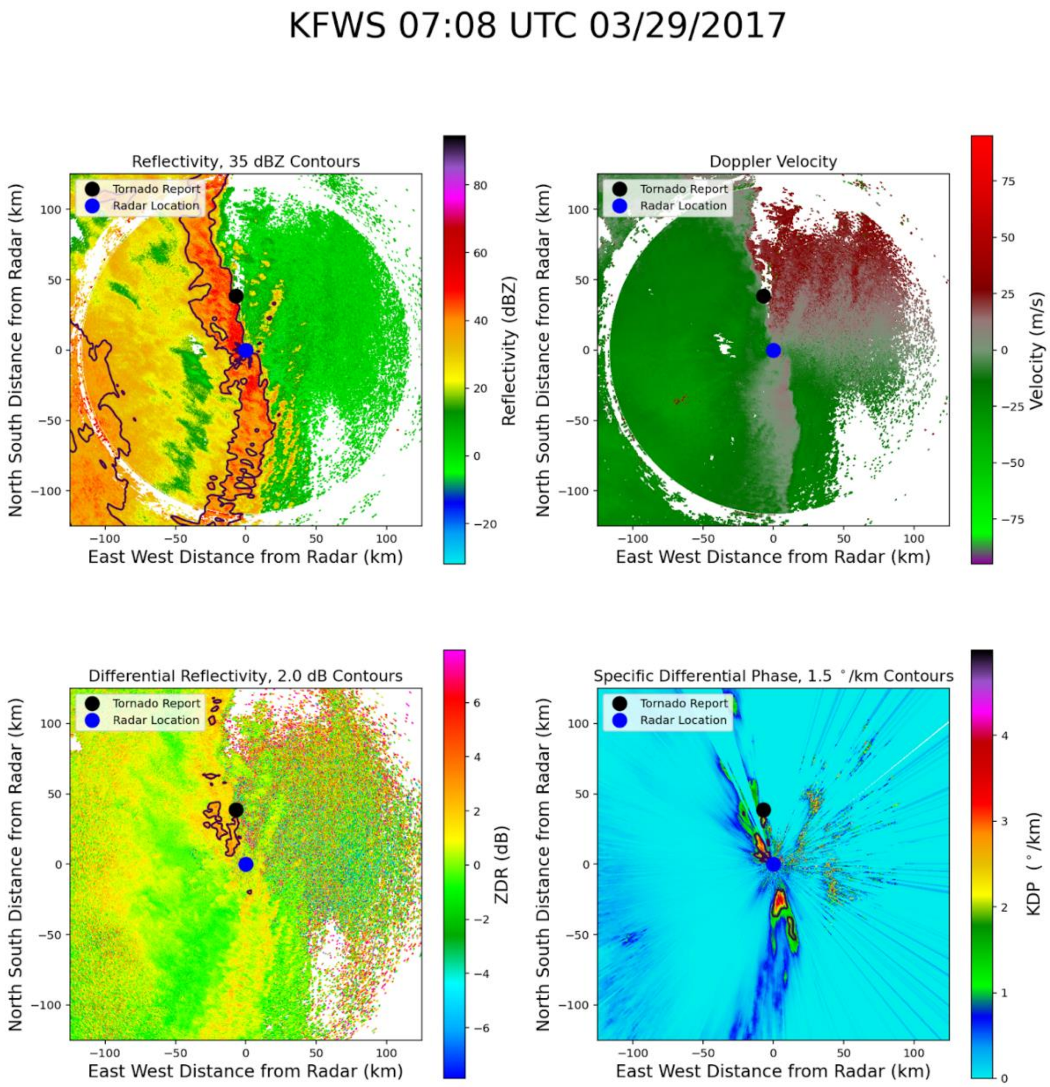

Figure 44. As in Figure 12, but for the KFWS radar at 7:08z on 3/29/2017 and for Z_{DR} and K_{DP} contours of 2.0 dB and 1.5 deg/km respectively.

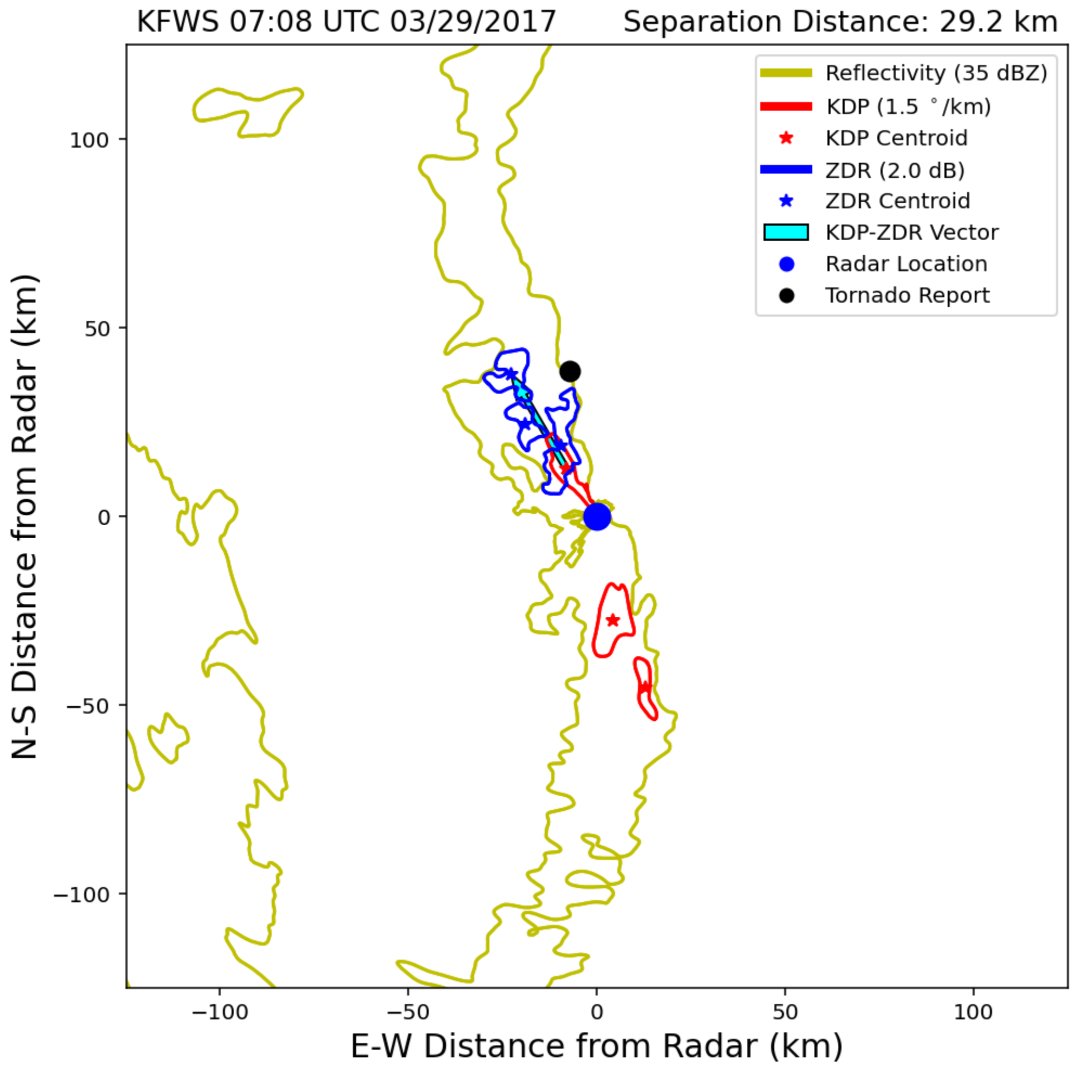

Figure 45. As in Figure 13 but for the KFWS radar at 7:08z on 3/29/2017, for Z_{DR} and K_{DP} contours of 2.0 dB and 1.5 deg/km respectively, and a K_{DP}/Z_{DR} separation vector magnitude of 29.2 km.

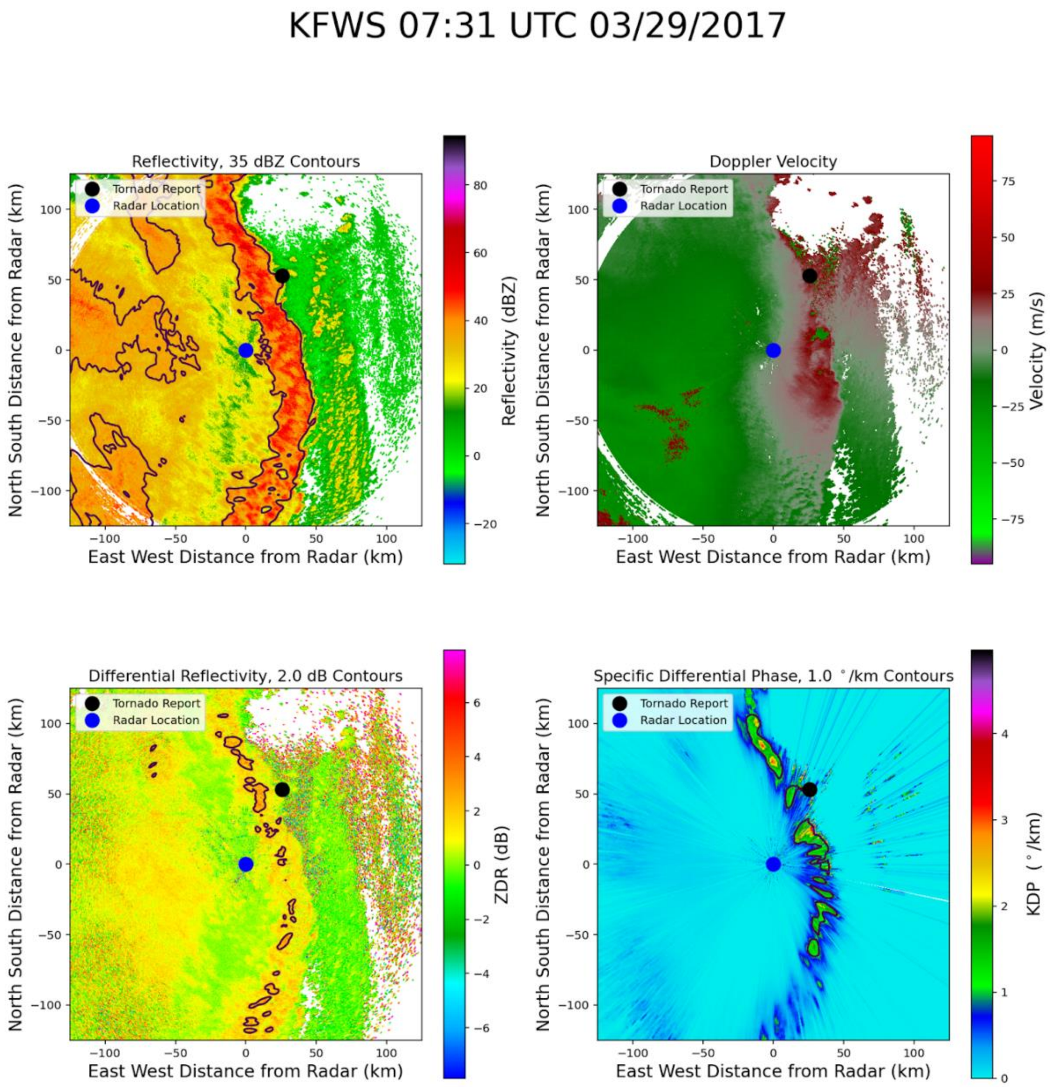

Figure 46. As in Figure 12, but for the KFWS radar at 7:31z on 3/29/2017 and for Z_{DR} and K_{DP} contours of 2.0 dB and 1.0 deg/km respectively.

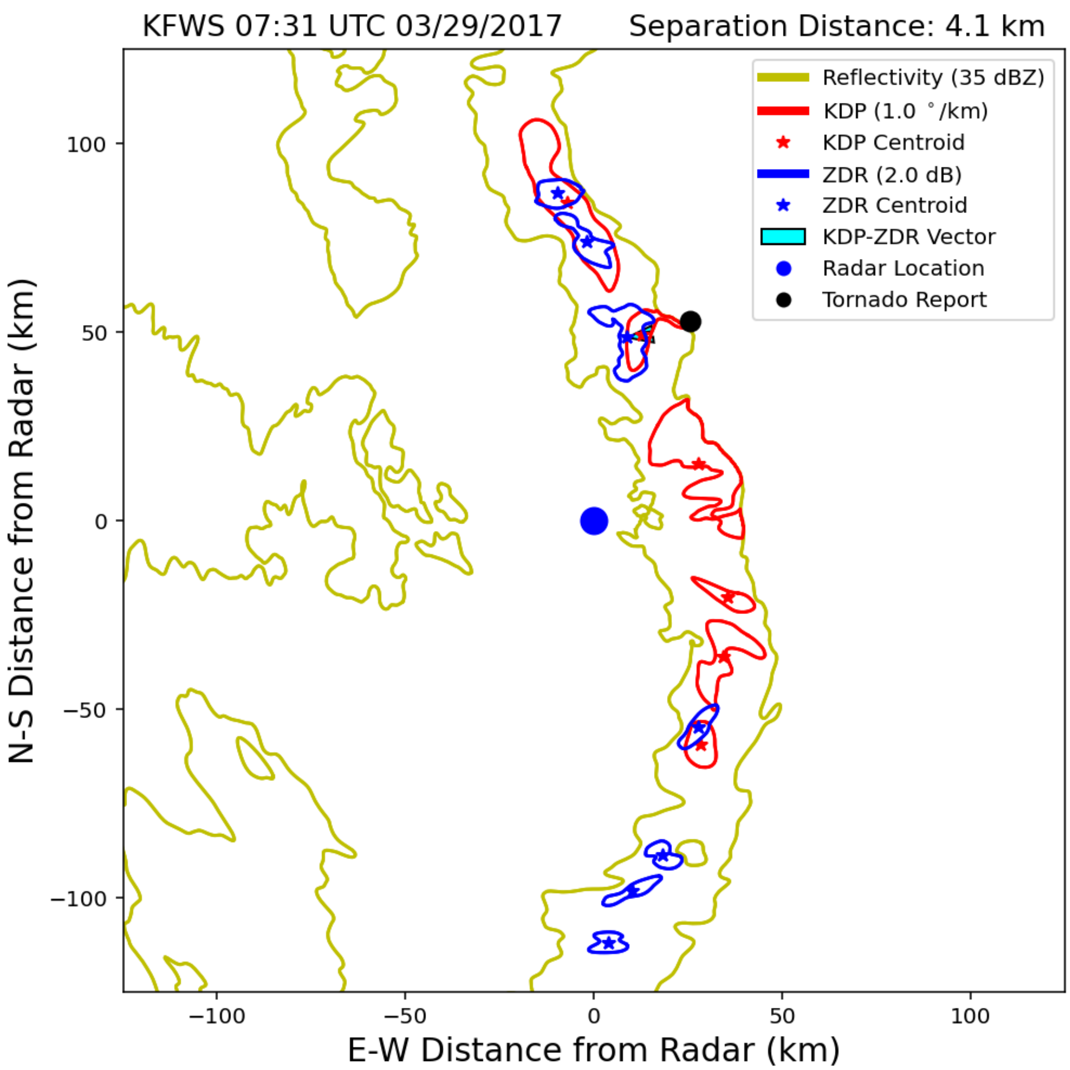

Figure 47. As in Figure 13 but for the KFWS radar at 7:31z on 3/29/2017, for Z_{DR} and K_{DP} contours of 2.0 dB and 1.0 deg/km respectively, and a K_{DP}/Z_{DR} separation vector magnitude of 4.1 km.

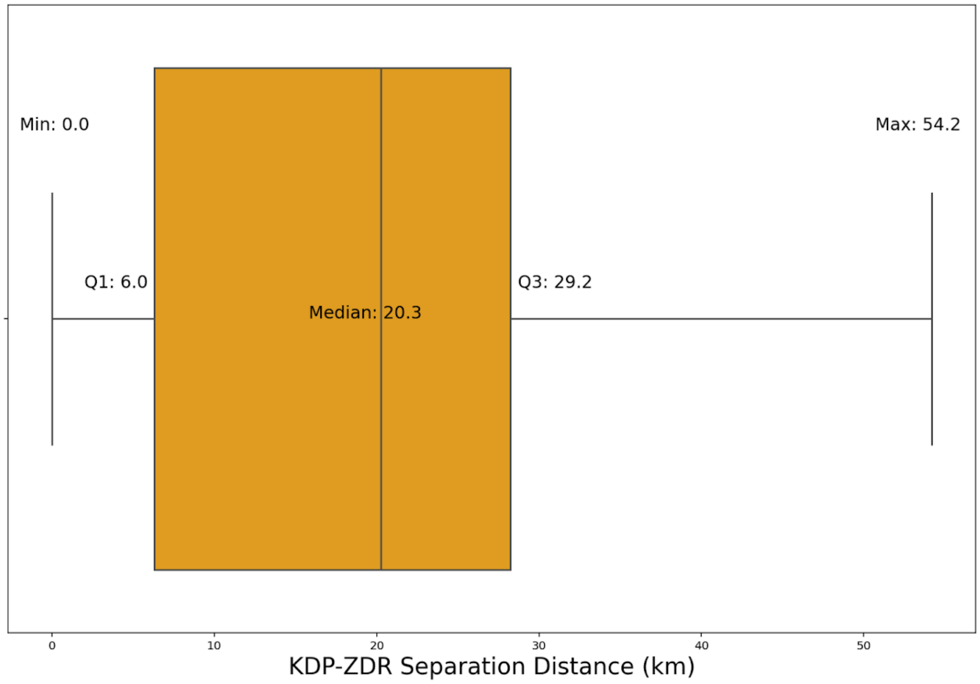

Figure 48. A boxplot of K_{DP}/Z_{DR} separation distance for the 18 case sample. The minimum separation was 0.0 km, and the maximum separation was 54.2 km with a median value of 20.3 km. 50% of the data is contained between the first and third quartiles of 6.0 and 29.2 km respectively.

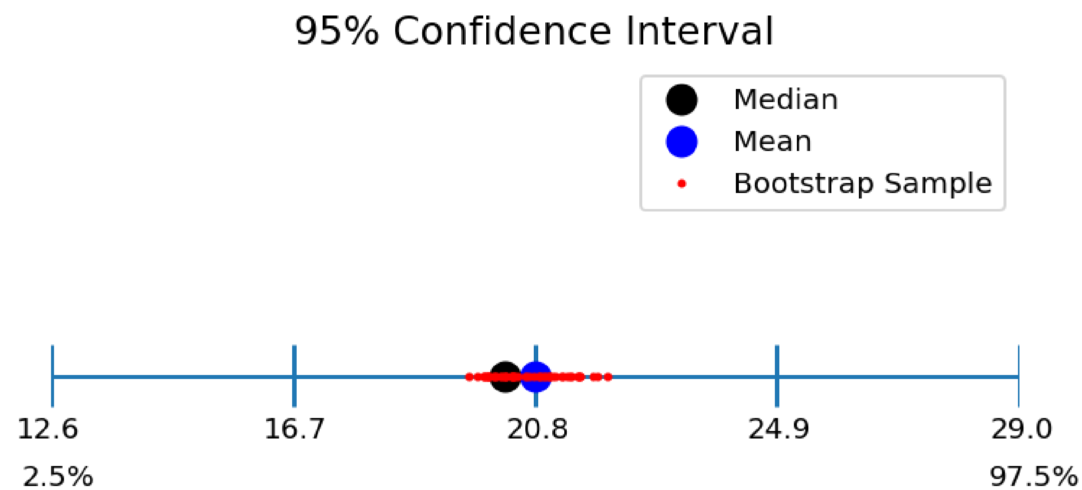

Figure 49. A number line showing the 95% confidence interval derived from the 18 case sample of K_{DP}/Z_{DR} separation distance ranging from 12.6 km to 29.0 km as well as the relative placement of the mean (blue dot) and median (black dot). The relative placement of all 50 bootstrap samples are placed using the smaller red dots.

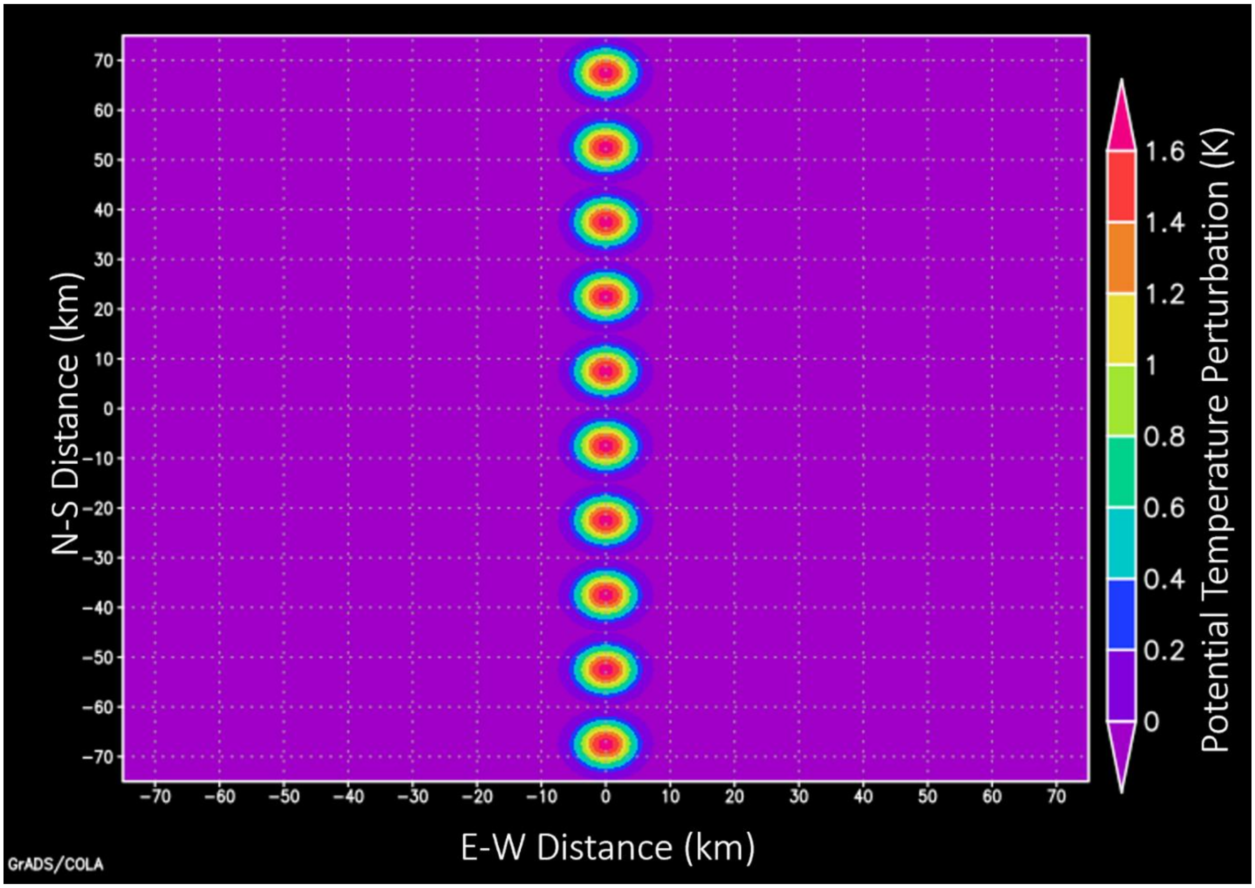

Figure 50. A plot at 1 km above ground level (AGL) of the warm bubbles used to initialize the QLCS in each simulation. The color bar shows the potential temperature perturbation values.

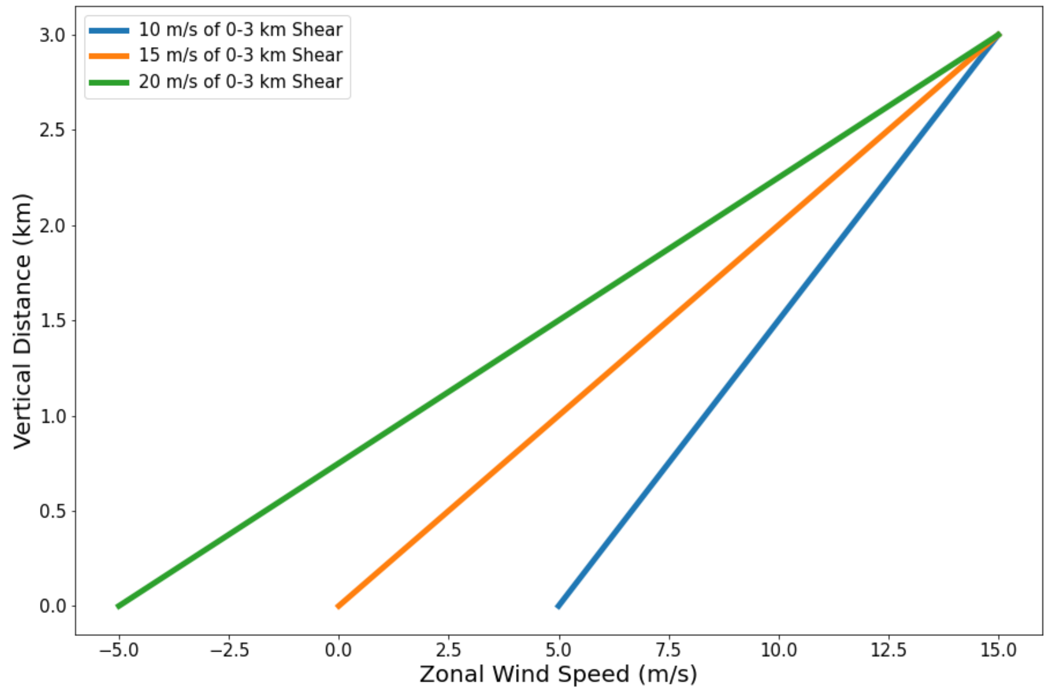

Figure 51. A plot of the three shear profiles used in the numerical simulations. The zonal wind speed (m/s) on the x axis is the ground-relative wind. The blue, orange, and green lines are 0-3 km wind profiles for the weak (10 m/s), moderate (15 m/s), and strong (20 m/s) homogenous simulations. The 10, 15, and 20 m/s shear profiles also represent the initial conditions of the heterogeneous simulation at the shear minimum (y = 37.5 km), average (y = 0, 75, -75), and maximum (y = -37.5) values.

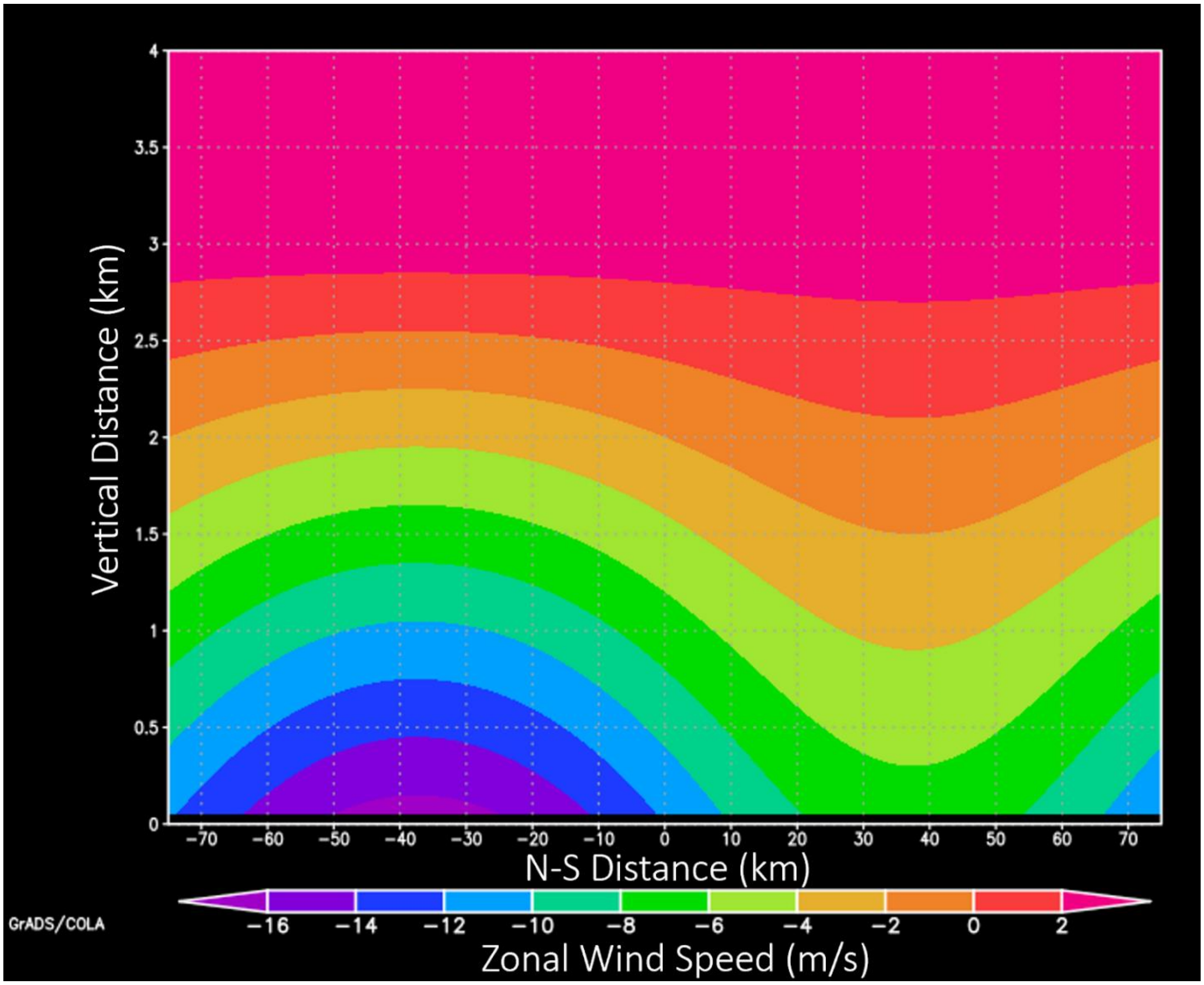

Figure 52. A N-S cross section, showing the vertical storm relative zonal wind profile used in the heterogeneous shear simulation. The storm motion was 12 m/s. Wind speed varies sinusoidally in the N-S direction below 3 km and is set to a constant value above 3 km. The sinusoidal variability decays linearly with height.

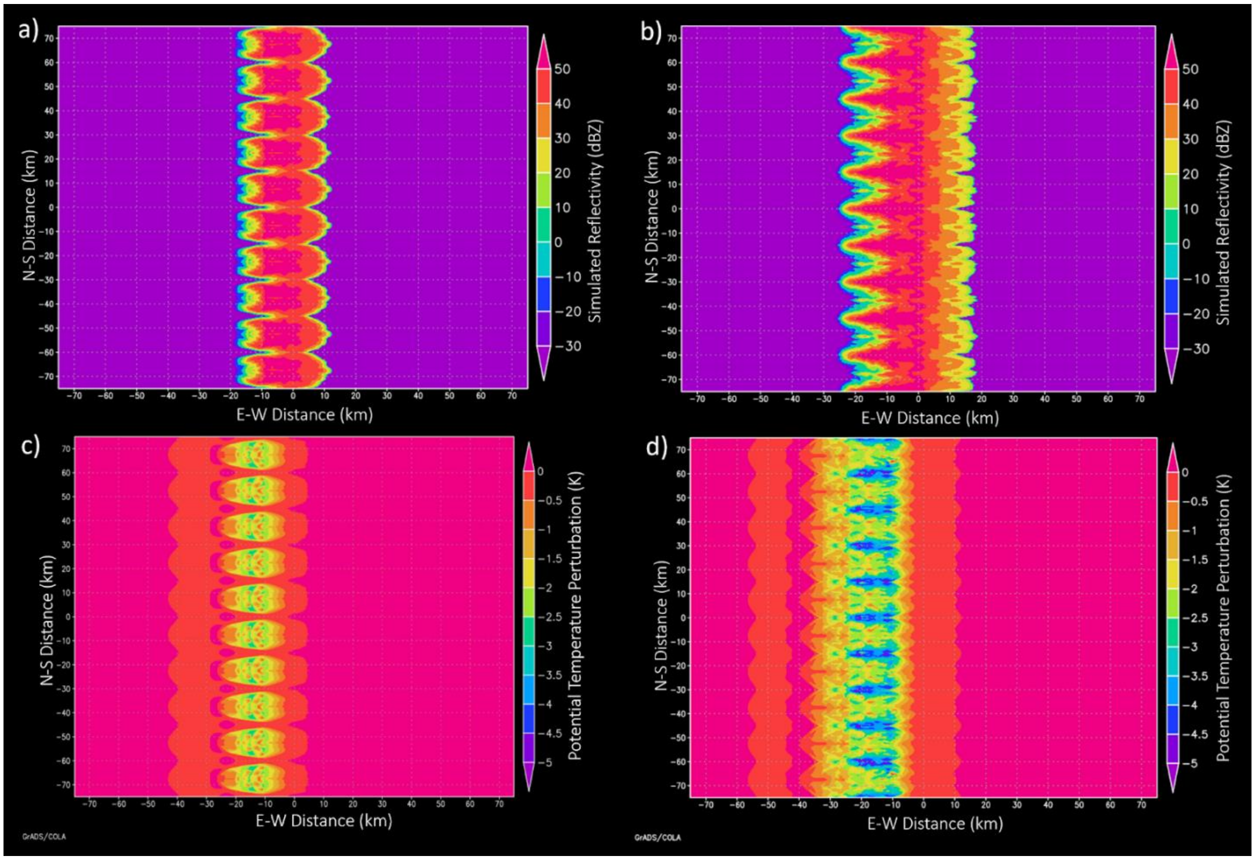

Figure 53. A 4 panel plot of the early evolution of the high-shear, homogeneous simulation. The left and right 2 images correspond to 52 and 65 minutes after the start of the simulation, respectively. The bottom 2 images represent potential temperature perturbation (K) while the top 2 images are the simulated reflectivity (dBZ) at 50 m AGL. At 65 minutes, cold pools from the individual 10 cells have merged, indicating a QLCS has formed.

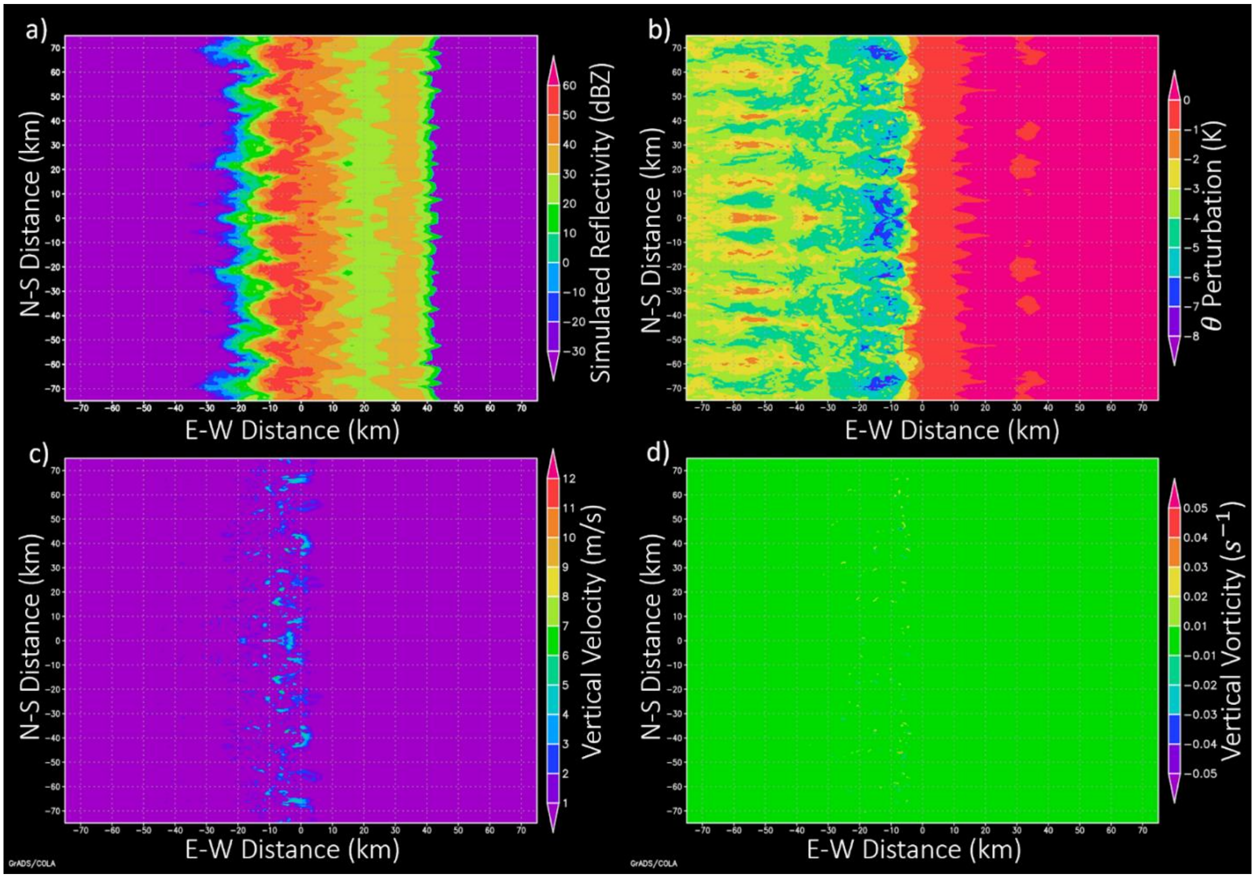

Figure 54. A 4 panel plot of simulated reflectivity at 50 m AGL, potential temperature perturbation (K) at 50 m AGL, vertical velocity (m/s) at 1.05 km, and vertical vorticity at 50 m AGL 2 hours into the simulation for the high shear (20 m/s) homogeneous case.

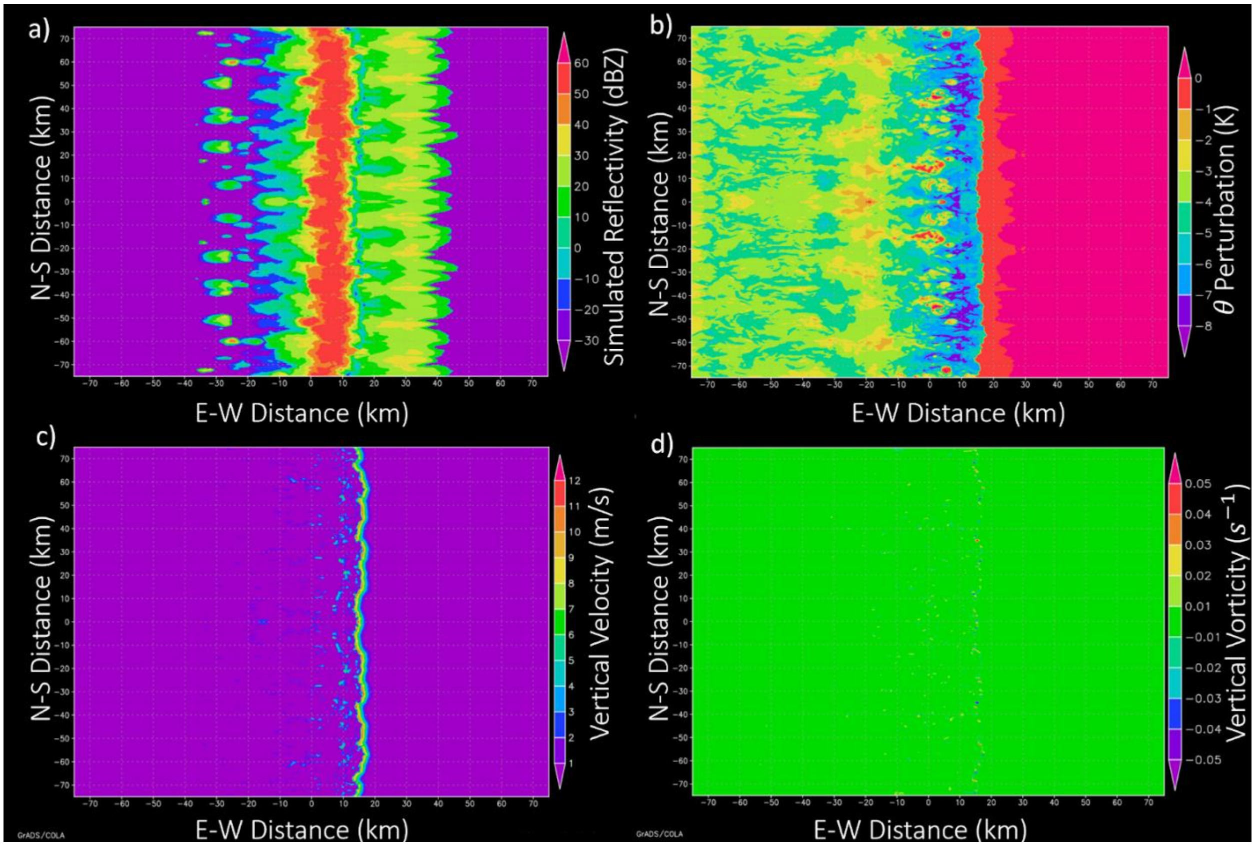

Figure 55. As in Figure 54 but for the moderate shear (15 m/s) case.

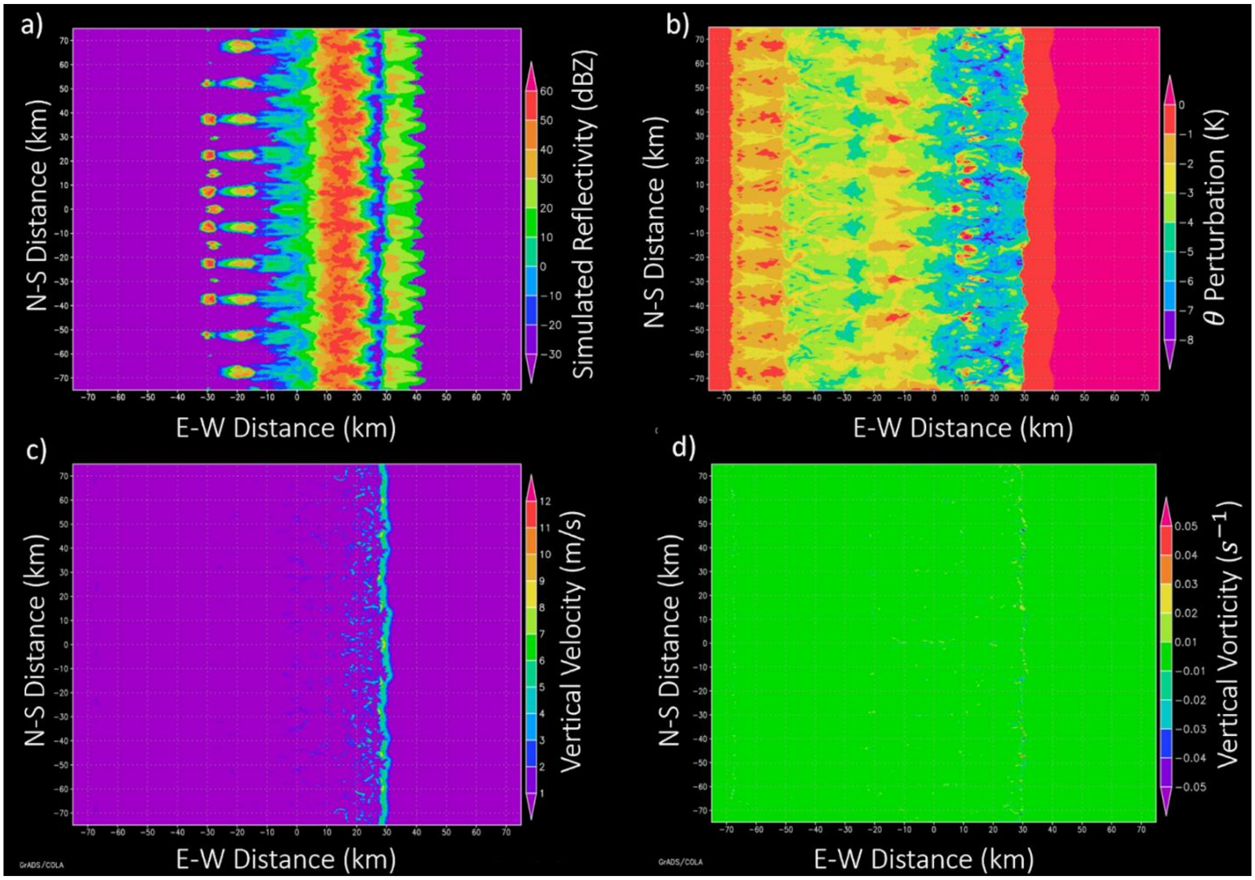

Figure 56. As in Figure 54 but for the low shear (10 m/s) case.

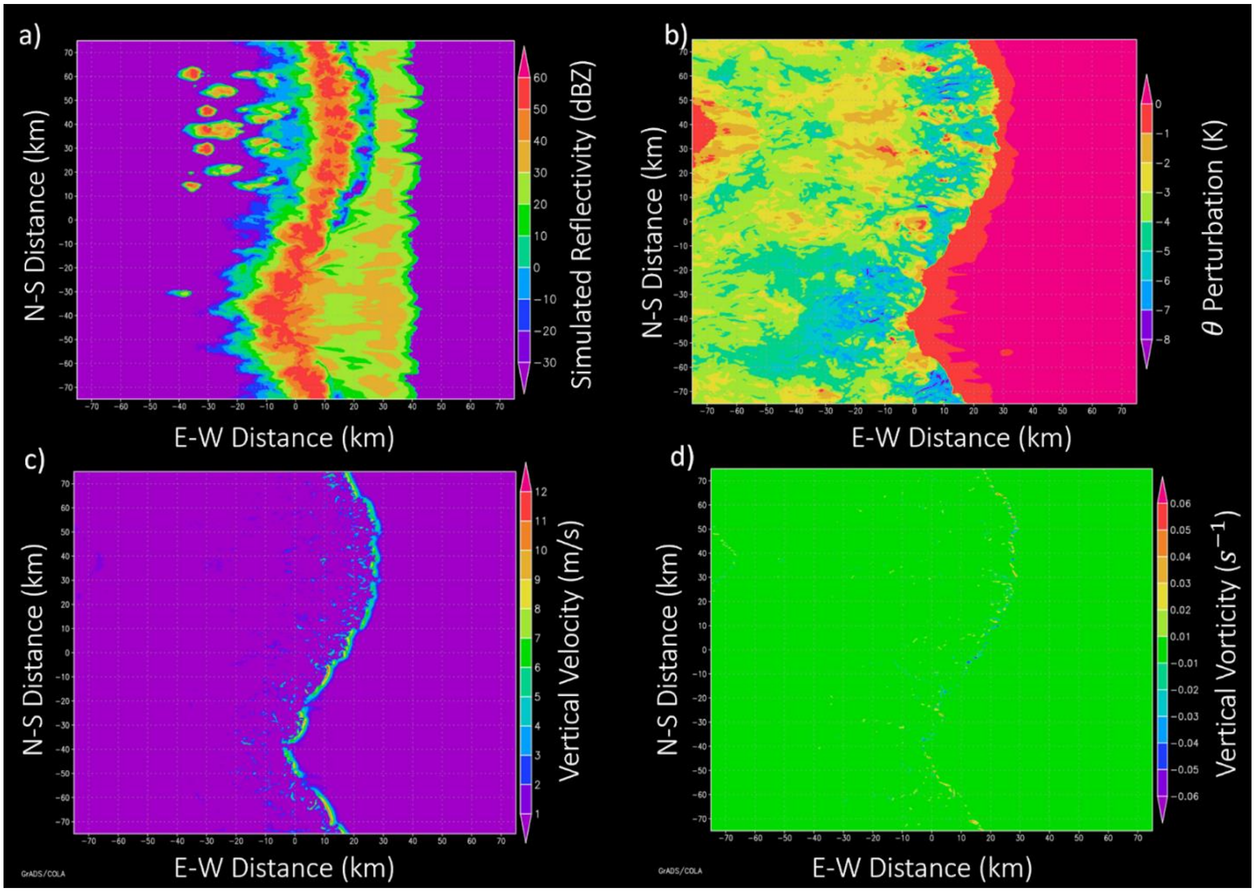

Figure 57. As in Figure 54 but for the heterogeneous shear case

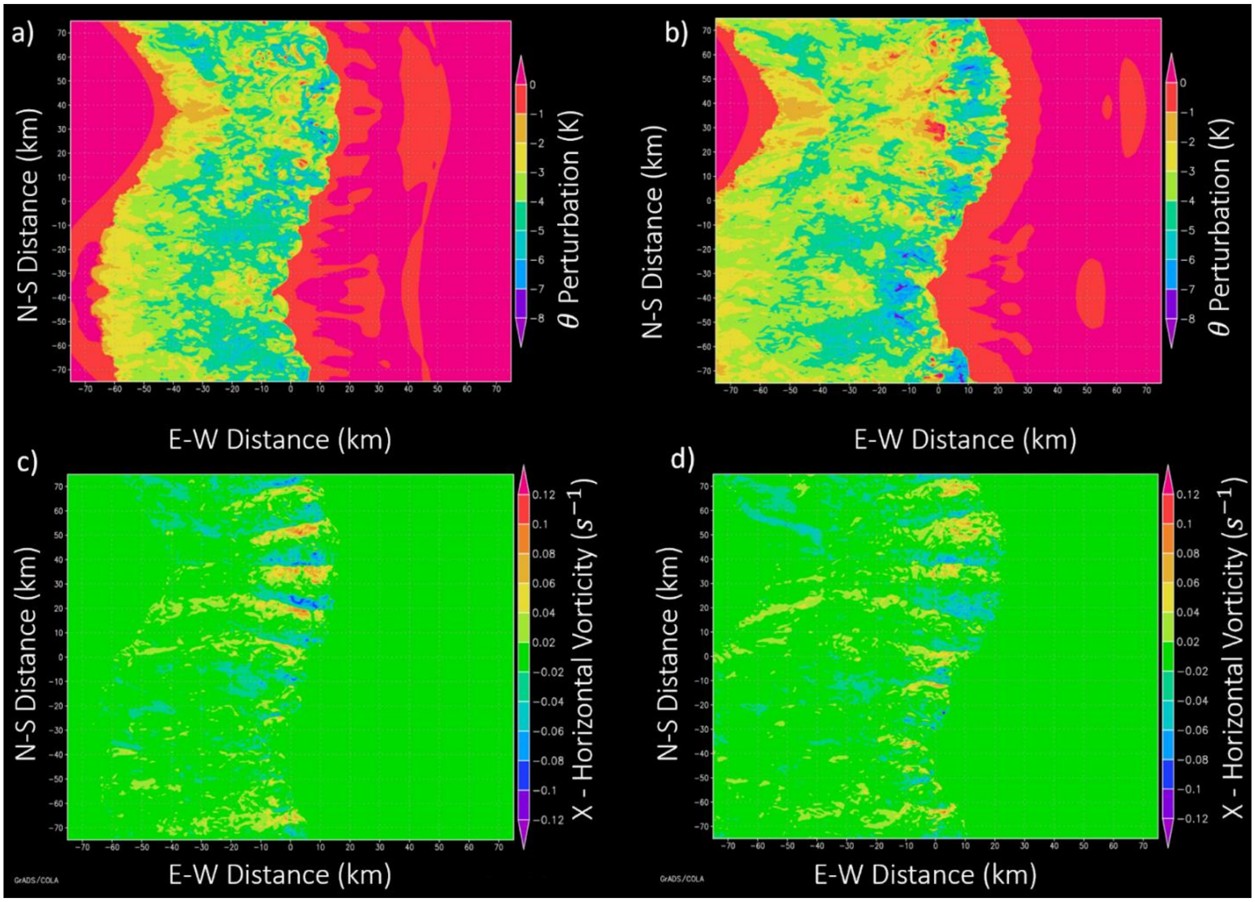

Figure 58. A 4 panel plot showing horizontal vorticity (panels c, d), presumably a result of baroclinic origin, in the cold pool of the QLCS in heterogeneous shear at 94 and 107 minutes and 50 m AGL. Panels a and b show the potential temperature perturbation (K) of the cold pool while panels c and d show the horizontal vorticity generated in the x direction.

ACADEMIC VITA

Work Experience

National Weather Service (Pathways) Internship **Summer 2021**

Amarillo, TX (Fully remote)

- Researched environmental conditions and radar features present prior to tornadogenesis in QLCSs
- Exposure to daily operations and forecasting
- Presented my research via poster at the 2022 American Meteorological Society (AMS) conference

Pine Tree Weather **Summer 2021**

Maine (Fully Remote)

- Produced graphical and written multi-day forecasts on Facebook, Twitter, and the Pine Tree Weather website
- Interacted with community following, answering questions about forecasts
- Gained experience in summer and winter forecasting

Research Assistant **June 2019-May 2021**

Penn State University

- Researched supercell evolution in heterogeneous moisture environments with Dr. Yvette Richardson
- Grew storms in a model simulation
- Gained experience in Linux and GrADS

National Weather Service (NWS) William M. Lapenta Internship **Summer 2020**

Meteorological Development Laboratory, Silver Spring, MD (Fully remote)

- Worked on the Localized Aviation Model Output Statistics Program (LAMP), assisted with Research to Operations, examined case studies, and performed prediction verification
- Coded a decision tree algorithm in Fortran to improve ceiling height and visibility forecasts
- Verified experimental High Resolution Rapid Refresh (HRRR) model ceiling height forecasts
- Gained experience in Linux shell scripting, submitting jobs on a supercomputer, Fortran, and Python
- Successfully worked as part of a fully remote team
- Presented my research orally and via paper at the 2021 AMS conference

Education

The Pennsylvania State University **August 2018-May 2022**

Schreyer Honors College

Meteorology & Atmospheric Science (BS)

- Noteworthy Courses: Radar Meteorology (Honors), Mesoscale (Honors), Micrometeorology, Forecasting Practicum

Computer Skills

- Proficient in Python
- Experience in MATLAB, Linux, ArcGIS, Excel, and Adobe Premier Pro
- Exposure to Fortran
- Experience submitting jobs on a supercomputer

Leadership

NCAR Undergraduate Leadership Workshop **Summer 2021**

- Learned to recognize and polish my leadership skills while engaging in discussions with peers and NCAR scientists

Irvin Hall Living Learning Community Vice-President **Fall 2019-Fall 2021**

- Organized major house social events, such as networking opportunities, for students in the community

Student Mentor - Penn State Branch of the American Meteorological Society **Fall 2020-Present**

- Sharing experiences about internships, classes, clubs, and professional opportunities with a meteorology freshman

Storm Chase Team at Penn State Secretary **Fall 2020-Spring 2021**

- Responsible for all communication to club members and smooth operation of club activities and functions

Irvin Hall Living Learning Community Academic Committee Chairperson **Spring 2019-Fall 2019**

- Led and managed house members in hosting required events as well as coordinated my own
- Organized and led Phone-A-Thon which involved calling and answering prospective students' questions

TEEMS (Total Engagement with Earth and Mineral Sciences) **Fall 2019**

- Mentor to incoming freshmen helping them adjust to college through a 4-day offsite orientation program

Student Organization Involvement

Campus Weather Service (PSU) **Spring 2021-Present**

- Forecast for PA regions while learning to analyze model data and communicate weather hazards to the public

Storm Chase Team at Penn State Club Member **Fall 2018-Present**

- Selected for the 2019 and 2020 Chase Team, traveling the country observing and learning about severe weather
- Collected, measured, and reported hail size for an IBHS (Insurance Institute for Business and Home Safety) study

Penn State Branch of the American Meteorological Society Member **Fall 2018-Present**

- Focus on career preparation through workshops and guest speakers. Promotes the AMS/NWA conferences

Chi Epsilon Pi Meteorology Honor Society **Spring 2021-Present**

- Accepted students have demonstrated high scholastic ability and promise of achievement in meteorology

Awards and Special Recognition

- Earth and Mineral Science Academy for Global Experience (EMSAGE) Laureate
- Ellen Steidle Achievement Award (2021 College of EMS PSU)
- AMS Senior Named Scholarship – Om & Saraswati Bahethi Scholarship (2021)
- Tim Samaras Memorial Scholarship (2021 NWA Iowa Chapter)